© Copyright by Yi Zhang 2014

All Rights Reserved

Subsurface Source Generation and Transport from Spills of Alcohol Blended Fuels

A Dissertation

Presented to

the Faculty of the

Environmental Engineering Graduate Program

University of Houston

In Partial Fulfillment

of the Requirements for the Degree

Doctor of Philosophy

in Environmental Engineering

by

Yi Zhang

May 2014

Subsurface Source Generation and Transport from Spills of Alcohol Blended Fuels

Yi Zhang

Approved:

Chair of the Committee
William G. Rixey, Associate Professor,
Civil and Environmental Engineering

Committee Members:

Shankar Chellam, Professor,
Civil and Environmental Engineering

Kishore Mohanty, Professor,
University of Texas at Austin
Petroleum and Geosystems Engineering

Cumaraswamy Vipulanandan, Professor,
Civil and Environmental Engineering

Keh-Han Wang, Professor
Civil and Environmental Engineering

Suresh K. Khator, Associate Dean,
Cullen College of Engineering

Hanadi S. Rifai, Professor and Director,
Environmental Engineering Graduate Program

ACKNOWLEDGEMENTS

First I would like to express my heartfelt gratitude to Professor William Rixey who is the committee chair, my graduate school advisor, and my greatest mentor. He is inspirational, supportive and truly thinking for his students. I also would like to express my deepest thanks to other committee members for their encouragement, support and insightful suggestions to my research work. They are: Professor Shankar Chellam, Professor Kishore Mohanty, Professor Cumaraswamy Vipulanandan, and Professor Keh-Han Wang.

I could not have finished my research without the help of my dear colleagues and friends: Ali, Irina, Lynn, Ranga, Rishi, and Yongzhi. I thank you for bringing cultural diversity around the world to the group which made everyday study and work more enjoyable and fun. I also thank the members of our partner group in Rice University for their contributions to the joint project, especially Professor Pedro Alvarez and his student, Jie Ma. I'm grateful to them for sharing their perspectives and expertise to the research work. I'm also grateful to the industry professionals who have been constantly involved with the project: Bruce Bauman, Tim Buscheck, Ravi Kolhatkar, Brent Stafford, and other experts from BP, Chevron, and Shell. I thank American Petroleum Institute (API) for providing financial support for the research.

I also would like to express my gratitude to my friends who are always there when I need them: Jie Fu, Yuanfeng Gu, Kai He, Siyun Xu, Chuanyu Zhao, and many other warmhearted people from Christian Churches. My deepest gratitude to my family: my father Zhiqiang Zhang and my mother Miaozhen Jin, for their encouragement, never-flagging support, and their confidence in me; my cousin and her family who happened to

live in the same city with me in this foreign country who helped me through many dreadful situations.

I also want to express my gratitude to you, my dear readers. Hopefully you will find beneficial content in this dissertation that is helpful to your work.

Subsurface Source Generation and Transport from Spills of Alcohol Blended Fuels

An Abstract

of a

Ph.D. Dissertation

Presented to

the Faculty of the

Environmental Engineering Graduate Program

University of Houston

In Partial Fulfillment

of the Requirements for the Degree

Doctor of Philosophy

in Environmental Engineering

by

Yi Zhang

May 2014

ABSTRACT

The goal of this research is to improve the current understanding of the physical-chemical impacts of alcohol in an alcohol-blended fuel on the distribution and transport characteristics of alcohol and non-aqueous phase liquid (NAPL) contaminants from fuel releases, which may result in new or enhanced groundwater quality issues. The principal aim is to build a framework for developing a predictive tool for guidance in field spill events associated with these blended fuels.

The phase partitioning and plume transport characteristics of alcohol and hydrocarbons in the fuel mixtures were studied via 2-D visualization experiments and quantitative pore water analyses. NAPL source generation and distribution characteristics were observed and compared for spills of various alcohol blended fuels to a model aquifer. As alcohol content in the fuel mixture increased, a higher fraction of the NAPL in the fuel was mobilized due to both cosolvency and phase mobilization. Variations in the size, shape, and saturation of the residual NAPL source generated from different alcohol fuel blends impacted the dissolution rates of the hydrocarbon contaminants and the longevity of the NAPL source. Ethanol was the alcohol studied in this research.

A multi-component, multi-phase flow simulator, UTCHEM, was used to quantitatively evaluate the impact of key physical-chemical properties that influence the transport behavior of alcohol as well as the distribution of the hydrocarbon contaminants in porous media. Numerical simulations compared well with physical model experiments for ethanol blended fuels to the aquifer in water-saturated conditions.

TABLE OF CONTENTS

ACKNOWLEDGEMENTS v

ABSTRACT viii

TABLE OF CONTENTS ix

LIST OF FIGURES xiii

LIST OF TABLES xvii

NOMENCLATURE xviii

CHAPTER 1 INTRODUCTION 1

1.1 Background on the Use of Alcohol Fuel Blends 1

1.2 Physical and Chemical Properties of Alcohols Used in Fuel Blends 2

1.3 Environmental Impacts from Spills of Alcohol Fuel Blends 4

1.4 Problem Statement 7

CHAPTER 2 LITERATURE REVIEW 9

2.1 Introduction 9

2.2 Phase Behavior and Modeling 10

2.3 Laboratory Scale Studies of Ethanol Blended Fuel Spills in the Subsurface 13

2.4 Field Scale Study 16

2.5 Numerical Models 19

CHAPTER 3 2-D PHYSICAL MODEL EXPERIMENTS — SOURCE GENERATION 22

3.1 Introduction 22

3.2 Materials and Methods 22

3.2.1 Configuration 22

3.2.2 Fluids and Dyes *24*

3.2.3 Media and the Packing Method *26*

3.2.4 Fixed-volume Releases of Ethanol Fuel Blends *28*

3.2.5 Visualization and Analytical Methods *28*

3.3 Results and Discussion 30

3.3.1 NAPL Source Behavior *30*

3.3.2 Ethanol Partitioning and Transport Behavior *38*

3.3.3 Quantitative Pore Water Measurements *40*

CHAPTER 4 2-D PHYSICAL MODEL EXPERIMENTS — DISSOLUTION 48

4.1 Introduction 48

4.2 Methods 49

4.2.1 Post-tracer Visualization *49*

4.2.2 Quantitative Analyses of Dissolved Hydrocarbons *50*

4.3 Results and Discussion 51

4.3.1 Post-tracer Visualization *51*

4.3.2 Hydrocarbon Concentrations in Pore Water *57*

4.3.3 Analysis with a NAPL Dissolution Model *62*

CHAPTER 5 NUMERICAL SIMULATION 71

5.1 Introduction 71

5.2 Model Formulations 72

5.2.1 Conservation Equation *72*

5.2.2 Phase Equilbria *74*

5.2.3 Viscosity *77*

5.2.4 Interfacial Tension *79*

5.2.5 Relative Permeability & Capillary Pressure *82*

5.2.6 Residual Saturation and Capillary Desaturation *87*

5.3 2-D Numerical Model 89

5.4 Simulation Results and Discussion 91

5.4.1 History Matching Approaches *91*

5.4.2 Ethanol Transport Behavior *93*

5.4.3 NAPL Formation and Migration *99*

5.4.4 Post-tracer analysis *102*

CHAPTER 6 SENSITIVITY ANALYSIS 108

6.1 Introduction 108

6.2 Parameter Selection 108

6.2.1 Porosity and Permeability *108*

6.2.2 Viscosity *110*

6.2.3 Interfacial Tension *111*

6.2.4 Relative Permeability Curves *112*

6.3 Results and Discussion 114

6.3.1 Impact of Permeability and Porosity *114*

6.3.2 Impact of Composition Dependent Viscosities *118*

6.3.3 Impact of interfacial tension *119*

6.3.4 Effect of Relative Permeability Curves *122*

CHAPTER 7 CONCLUSIONS 124

7.1 Physical model experiments 124

7.1.1 Source Generation and Transport Behavior *124*

7.1.2 Dissolution of Hydrocarbons from a Residual NAPL Source *126*

7.2 Numerical Simulations 127

REFERENCES 130

APPENDIX A CAPILLARY PRESSURE-WATER SATURATION MEASUREMENTS 137

APPENDIX B IMAGE PROCESSING RESULTS FOR RESIUDAL NAPL SATURATION CALCULATIONS 138

APPENDIX C PORE WATER SHORT-TERM CONCENTRATION MEASUREMENT FOR INDIVIDUAL HYDROCARBON COMPOUND 145

APPENDIX D SIMULATION RESULTS WITH VARIOUS PERMEABILITY AND POROSITY CASES 149

LIST OF FIGURES

Figure 1.1 Ternary phase diagram for ethanol-benzene-water at 30°C. 3

Figure 3.1 (a) Photograph of 2-D glass model aquifer; (b) 2-D physical model aquifer setup and dimensions. 24

Figure 3.2 Ethanol plume transport and NAPL saturation profiles for a release of E15 into a saturated aquifer. 34

Figure 3.3 Ethanol plume transport and NAPL saturation profiles for a release of E25 into a saturated aquifer. 35

Figure 3.4 Ethanol plume transport and NAPL saturation profiles for a release of E50 into a saturated aquifer 36

Figure 3.5 Ethanol plume transport and NAPL saturation profiles for a release of E85 into a saturated aquifer. 37

Figure 3.6 NAPL saturation profiles for releases of E0, E5, and E10. 38

Figure 3.7 Ethanol transport for a release of pure ethanol (E100) into a saturated aquifer. 40

Figure 3.8 E15 Pore water concentrations. 44

Figure 3.9 E25 Pore water concentrations. 45

Figure 3.10 E50 Pore water concentrations. 46

Figure 3.11 E85 Pore water concentrations. 47

Figure 4.1 Post-tracer study of groundwater passing through the residual NAPL source formed from an E15 spill. 53

Figure 4.2 Post-tracer study of groundwater passing through the residual NAPL source formed from an E25 spill. 54

Figure 4.3 Post-tracer study of groundwater passing through the residual NAPL source formed from an E50 spill. 55

Figure 4.4 Post-tracer study of groundwater passing through the residual NAPL source formed from an E85 spill. 56

Figure 4.5 Pore water hydrocarbon concentrations measured at 2, 3, 4 weeks after the spill of an E25 ethanol fuel blend. 59

Figure 4.6 Pore water hydrocarbon concentrations measured at 2, 3, 4 weeks after the spill of an E50 ethanol fuel blend. 60

Figure 4.7 Pore water hydrocarbon concentrations measured at 2, 3, 4 weeks after the spill of an E85 ethanol fuel blend. 61

Figure 4.8 Comparison of experimental pore water measurements with an equilibrium dissolution model (Equation 4-8) for longer-term dissolution from NAPL sources for various fuel blends. 68

Figure 5.1 Binodal curve and tie lines for a typical ethanol-gasoline-water system. 77

Figure 5.2 (a) Comparison between the viscosities of ethanol-hydrocarbon-water aqueous mixtures and hydrocarbon-free ethanol-water mixtures; (b) Comparison of Equation 5-7 and experimental measurements for ethanol-water mixtures..... 79

Figure 5.3 Comparison between IFT values using Equation 5-9 and experimental measurements..... 81

Figure 5.4 NAPL capillary desaturation curve. 89

Figure 5.5 (a) 2-D physical model aquifer used for laboratory experiments. (b) Corresponding grid design for the 2-D numerical simulations..... 91

Figure 5.6 Ethanol plume transport for a release of E15. Comparisons of visualization experiments and numerical simulations 95

Figure 5.7 Ethanol plume transport for a release of E25. Comparisons of visualization experiments and numerical simulations 96

Figure 5.8 Ethanol plume transport for a release of E50. Comparisons of visualization experiments and numerical simulations 97

Figure 5.9 Ethanol plume transport for a release of E85. Comparisons of visualization experiments and numerical simulations. 98

Figure 5.10 NAPL saturation distributions two days after ethanol fuel blend releases. Comparisons of numerical simulations and visualization experiments. 101

Figure 5.11 Post-tracer study of groundwater passing through the NAPL source formed from an E15 spill. Comparison of numerical simulations and experiments 104

Figure 5.12 Post-tracer study of groundwater passing through the NAPL source formed from an E25 spill. Comparison of numerical simulations and experiments 105

Figure 5.13 Post-tracer study of groundwater passing through the NAPL source formed from an E50 spill. Comparison of numerical simulations and experiments 106

Figure 5.14 Post-tracer study of groundwater passing through the NAPL source formed from an E85 spill. Comparison of numerical simulations and experiments. 107

Figure 6.1 Effect of grain size and sorting on permeability and porosity for uncemented sands. 109

Figure 6.2 Ethanol-water mixture viscosities. 111

Figure 6.3 (a) Capillary pressure-saturation curve and (b) relative permeability-saturation curve derived from a typical capillary pressure-saturation experiment. 113

Figure 6.4 E50 ethanol plume behavior in a layered system. Permeability above the spill region was ½ that of the spill layer 115

Figure 6.5 E50 ethanol plume behavior in a layered system. Permeability above the spill region was two times that of the spill layer. 116

Figure 6.6 E50 ethanol plume behavior in a layered system. Permeability above the spill region was 1/10 that of the spill layer. 116

Figure 6.7 E85 ethanol plume behavior in a layered system. Permeability above the spill region was 1/10 that of the spill layer. 117

Figure 6.8 Residual NAPL saturation distributions for E50 and E85 spills in a layered system. 117

Figure 6.9 E50 ethanol plume behavior with linear aqueous mixture viscosities. 118

Figure 6.10 Residual NAPL saturation distributions for E50 spill with linear aqueous mixture viscosities. 119

Figure 6.11 E15 ethanol plume behavior for constant IFT. 120

Figure 6.12 E25 ethanol plume behavior for constant IFT. 120

Figure 6.13 E50 ethanol plume behavior for constant IFT. 121

Figure 6.14 E85 ethanol plume behavior for constant IFT. 121

Figure 6.15 Residual NAPL saturation profiles for (a) E15, (b) E25, (c) E50, and (d) E85 for constant IFT. 122

Figure 6.16 E50 ethanol plume behavior simulated using typical capillary pressure, relative permeability, and residual saturation parameters. 123

Figure 6.17 E50 residual NAPL saturation profile simulated using typical capillary pressure, relative permeability, and residual saturation parameters. 123

LIST OF TABLES

Table 1.1 Physical chemical properties of ethanol and methanol..... 4

Table 3.1 Physical-chemical properties of the hydrocarbons used in the synthetic gasoline. 25

Table 3.2 Ottawa Federal Fine Sieve analysis. 27

Table 3.3 NAPL residual saturation and impacted area formed from release of E15, E25, E50, and E85 fuel blends. 33

Table 3.4 Maximum dissolved ethanol and hydrocarbon concentrations and their corresponding locations from spills of E15, E25, E50, and E85 fuel blends. 41

Table 4.1 Maximum dissolved hydrocarbon concentrations from longer-term dissolution experiments following spills of E25, E50, and E85 fuel blends. 58

Table 4.2 Source length, seepage velocity, NAPL saturation, and initial pore water concentration for hydrocarbon components after depletion of ethanol. 67

Table 5.1 Parameters used for relative permeability curves. 85

Table 5.2 Capillary pressure parameters. 86

Table 6.1 Simulations to assess impact of permeability and porosity. 110

Table 6.2 Typical relative permeability parameters and values used in the simulations. 113

NOMENCLATURE

Units: SI

a	IFT model parameter
A	Phase model parameter
B	Phase model parameter
c	IFT model parameter
$\tilde{C}_{\kappa}$	Overall concentration of component κ in all phases, m^3/m^3 PV
$C_{\kappa l}$	Volume concentration of κ in phase l, m^3/m^3
C_l^e	Concentrations of ethanol in the fluid phase "l", m^3/m^3
C_l^o	Concentrations of NAPL in the fluid phase "l", m^3/m^3
C_l^w	Concentrations of water in the fluid phase "l", m^3/m^3
$C_{e,\max}$	Maximum concentration of ethanol for a two phase system, m^3/m^3
$C_{o,pl}$	Hydrocarbon concentration at the plait point, m^3/m^3
C_i^w	Concentration of the hydrocarbon component "i" in the aqueous phase, kg/m^3
C_i^o	Concentration of the hydrocarbon "i" in the NAPL phase, kg/m^3
C_i^{w*}	Nondimensionalized concentration
C_{i0}^w	Initial dissolved hydrocarbon component "i" concentration at the edge of the NAPL source, kg/m^3
D	Dispersion coefficient, m^2/s
$\vec{\tilde{D}}_{\kappa l}$	Dispersive flux, $kg/(s \cdot m^2)$
E	Plait point concentrations parameter

F_o IFT correction factor

g Gravitational constant, m/s^2

k_{ro} Relative permeability of the NAPL phase, fraction

k_{rw} Relative permeability of the water phase, fraction

k_o Permeability for the NAPL phase, m^2

k_w Permeability for the water phase, m^2

k Absolute permeability, m^2

k_{rw}^0 Endpoint relative permeability of water phase, fraction

k_{ro}^0 Endpoint relative permeability of water phase, fraction

$\overline{\overline{K}}_{\kappa l}$ Dispersivity tensor, m^2/s

K_i^{o-w} Partition coefficient between the NAPL phase and the water phase

L Length of the NAPL source zone, L

MW_{Avg}^w Average molecular weight of the aqueous phase

MW_{Avg}^o Average molecular weight of the NAPL phase

n^w Relative permeability exponent for water phase

n^o Relative permeability exponent for NAPL phase

N_B Bond number

N_C Capillary number

N_T Trapping number

P_b Entry pressure, Pa or kg/(m·s^2)

P_c	Capillary pressure, Pa
Pe	Peclet number
R_κ	Total source/sink for species κ, kg/(m^3·s)
R_{ow}	Solubility ratio, m^3/m^3
R_i	Retardation coefficient for the hydrocarbon component "i"
S_l	Saturation of phase l, m^3/m^3 PV
S^*	Normalized water saturation
S_w	Water phase saturation, m^3/m^3 PV
S_o	Oil phase saturation, m^3/m^3 PV
S_{or}	Residual NAPL phase saturation, m^3/m^3 PV
S_{wr}	Residual water phase saturation, m^3/m^3 PV
S_{or}^*	Normalized residual NAPL saturation, m^3/m^3 PV
S_{or}^{high}	Residual saturation of NAPL phase at high capillary numbers, m^3/m^3 PV
S_{or}^{low}	Residual saturation of NAPL phase at low capillary numbers, m^3/m^3 PV
T_o	Trapping parameter for NAPL phase
t	Time, s
t^*	Nondimensionalized time
$\vec{u}_l$	Phase velocity, m/s
v	Interstitial velocity, m/s
x	Downstream location, m
x^*	Nondimensionalized distance

Greek Symbols

$\alpha 1, \alpha 2, \alpha 3, \alpha 4, \alpha 5$ Ethanol plume viscosity parameters

γ_i^w Activity coefficient of hydrocarbon component "i" in the aqueous phase

γ_i^o Activity coefficient of hydrocarbon component "i" in the NAPL phase

γ_l^w Specific weight of water, kN/m^3

γ_l^o Specific weight of gasoline, kN/m^3

γ_l^e Specific weight of ethanol, kN/m^3

μ Viscosity of the displacing fluid, Pa·s

μ'_w Viscosity of the water ethanol aqueous phase mixture, Pa·s

μ_w Water viscosity, Pa·s

μ_o NAPL viscosity, Pa·s

θ Angle of the local flow vector relative to the horizontal direction, degree

λ^d Drainage capillary pressure exponent

λ^i Imbibition capillary pressure exponent

ρ_κ Density of the pure component κ, kg/m^3

ρ_l Density of phase l, kg/m^3

$\rho_{l'}$ Density of phase l', kg/m^3

σ_{ow}^0 IFT between the oil phase and the aqueous phase without ethanol's presence, N/m

σ_{ow} IFT between the oil phase and the aqueous phase, N/m

$\sigma_{ll'}$ Interfacial tension between phases l and l', N/m

ϕ Porosity, fraction

Subscripts

Avg	Averaged
b	Entry
B	Bond (number)
c	Capillary
C	Capillary (number)
T	Trapping (number)
i	Hydrocarbon component in presents in the fuel mixture
$i0$	Initial concentration of hydrocarbon component “i”
κ	Species number
	1 – Water
	2 – Oil
	3 – Surfactant
	4 – Polymer
	5 – Chloride
	6 – Calcium
	7 – Alcohol
	8 – Air
	9 – Tracer components
l , l'	Phase number
	1 – Aqueous
	2 – Oleic
	3 – Microemulsion

	4 – Air
max	Maximum concentration
pl	NAPL concentration at the plait point
r	Residual

Superscripts

d	Drainage
e	Ethanol
i	Imbibition
o	Oil (NAPL)
w	Water
*	Normalized property
0	Endpoint property

CHAPTER 1 INTRODUCTION

1.1 Background on the Use of Alcohol Fuel Blends

The Clean Air Act Amendments of 1990 (CAAA) required the use of oxygenated gasoline to reduce the emission of uncombusted carbon monoxide and to dilute the hazardous gasoline components such as aromatics and sulfur. Since 1995, the CAAA requires that reformulated gasoline (RFG) be used in cities that exceed acceptable ground-level ozone concentrations. Between 1995 and May 2006, RFGs were required to have a minimum oxygen content of 2 percent oxygen by weight. Many alcohol and ethers can be used as an oxygenate additive, e.g., methanol, ethanol, n-butanol, methyl tert-butyl ether (MTBE), etc. Prior to 2000, most refiners chose MTBE over other oxygenates. Unlike ethanol and other alcohols, MTBE can be shipped through existing pipelines, and its volatility is lower, making it easier to meet emission standards. However, in the mid- to late-1990s contamination of groundwater by MTBE became wide spread. Thus, the use of MTBE became quite controversial.

In the United States, MTBE was banned in many states across the country beginning in 2000, and was replaced by ethanol. Ethanol is now being used extensively as an oxygenate additive. In 2005, Congress passed the Energy Policy Act that removed the oxygenate requirement for RFG. At the same time, Congress also instituted a renewable fuel standard which required 7.5 billion gallons of renewable-fuel to be blended into gasoline by 2012. In response, refiners made a wholesale switch removing MTBE and blending fuel with ethanol. Because ethanol is domestically produced, it helps reduce America's dependence upon foreign imported energy.

Currently, the United States, Brazil and many European countries are primarily using ethanol fuel blends, while China is primarily using methanol fuel blends. Methanol can be produced from large-scale plants using coal or municipal wastes. With a variety of sources, using methanol fuel blends are trending over the years. China produced over 30 million tons of methanol in 2012 and used more than one billion gallons of methanol per year as a transportation fuel in both low level blends (M3 to M15; 3-15% methanol by volume, v/v), used in conventional vehicles, and high level blends (M85 and M100), used in vehicles designed to accommodate the use of high content methanol fuels. Currently M15 fuel blends are widely used in China due to the domestic availability of methanol and its lower cost compared to gasoline.

1.2 Physical and Chemical Properties of Alcohols Used in Fuel Blends

Ethanol has a hydroxyl group and a short carbon chain. Due to the presence of the hydroxyl group, ethanol has a higher density and viscosity, and is less volatile than non-polar organic compounds of similar molecular weight, e.g., propane. With the hydroxyl group ethanol can dissolve ionic compounds. The nonpolar end of the ethanol molecule also enhances the solubilization of nonpolar compounds, such as aromatic and aliphatic hydrocarbons found in gasoline.

When water and hydrocarbon phases are present, ethanol partitions primarily to the aqueous phase. Phase equilibria data are usually presented as a ternary phase diagram like that shown in Figure 1.1. For a given ethanol-hydrocarbon-water mixture, the binodal curve and tie lines provide the phase composition information for both aqueous and hydrocarbon phases when the overall composition of the mixture falls into the two-phase region.

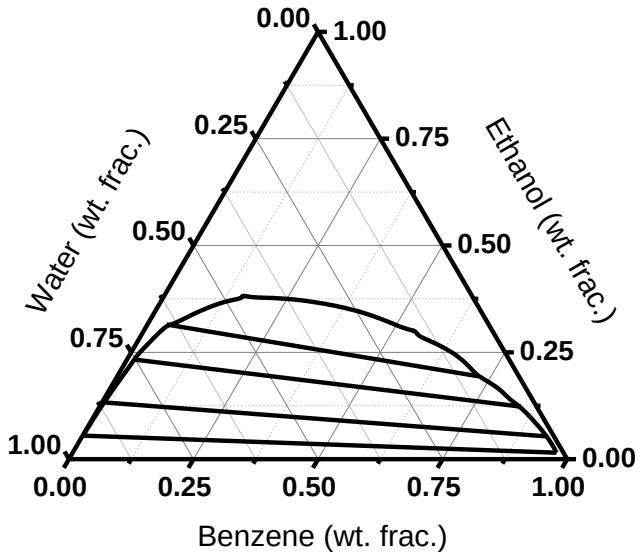

Figure 1.1 Ternary phase diagram for ethanol-benzene-water at 30°C. Adapted from Brandani et al. (1985).

The presence of ethanol may have an impact on fluid properties that influence fluid transport processes in porous media. Those properties are usually temperature and composition dependent. The addition of even a few percent of ethanol to water sharply reduces the surface tension of water as well as the interfacial tension (IFT) between water and a separate hydrocarbon phase. Adding ethanol also increases the viscosity of the aqueous phase. Viscosity reaches a maximum for intermediate ethanol concentrations in water. These effects are explained in detail in Chapter 5.

Other alcohols (methanol, isobutanol) are also being used or considered as possible alternative fuel additives. They have physical and chemical properties that are similar to ethanol due to the same hydroxyl group in their molecular structure. Thus, groundwater impacts similar to that for ethanol fuel blend releases may be expected.

Physical chemical properties of ethanol and methanol that impact transport processes in porous media are listed in Table 1.1.

Table 1.1 Physical chemical properties of ethanol and methanol

	Ethanol	**Methanol**
Molar Mass, g/mol	46.068	32.042
Specific Gravity, kg/m^3	0.7893^{20}	0.7914^{20}
Viscosity, mPa·s	1.203^{20}	0.586^{20}
Surface Tension, dyn/cm	21.97^{25}	22.07^{25}
Diffusivity (Aq.) (infinite dilution), 10^{-5} cm^2/s	1.24^{25}	1.28^{15}

Reference: Haynes (2013). Temperatures (^oC) for the measured values are shown as superscripts.

1.3 Environmental Impacts from Spills of Alcohol Fuel Blends

In the United States, fuel-use ethanol is produced primarily from fermentation of sugar (from sugar cane) or starch (from corn). After the distillation and dehydration processes, 2 to 5% (v/v) of a gasoline-compatible denaturant is added to the ethanol to make denatured ethanol. Denatured ethanol is shipped from the production site typically via rail to terminals where denatured ethanol is blended with gasoline at various proportions to make the desired ethanol fuel blends. Then the fuel blends with different ethanol content are distributed locally to the gas stations by tank truck. Currently the common ethanol fuel blends are E10 and E85.

Gasoline is refined from crude oil and consists of hydrocarbons from C4-C12 (4-12 carbon atoms per molecule). Within this hydrocarbon mixture are toxic chemicals such as BTEX (benzene, toluene, ethylbenzene and xylenes). These are typical groundwater and soil contaminants that could be released to the environment from leaking underground storage tanks (USTs) and from spill events during transport or accidental spills from above-ground storage tanks. There were 611,500 federally-regulated, active USTs at approximately 223,000 sites across the country in 2009. Prior to 2009, 488,000 releases had been reported since the beginning of the EPA's UST program, with thousands of new releases being reported every year.

Conventional gasoline spills are relatively easier to be located and remediated because the contaminant is generally above or close to water table due to its lower density than the water. It is different from dense non-aqueous phase liquids (DNAPL) which can migrate downward into the saturated zone until an impermeable layer is reached. When a cosolvent such as ethanol is added to gasoline, depending on the ethanol content in the gasoline, the distribution of the non-aqueous phase liquid (NAPL) and the migration of the dissolved NAPL components could behave quite differently from a conventional light NAPL (LNAPL). The following two environmental concerns related to using ethanol blended fuels versus conventional fuels have been identified (Powers et al., 2001b).

1. The physical chemical impact on the mobility of the volatile hydrocarbon contaminants typically found in gasoline (e.g., BTEX). Here the mobility includes the mobility of the NAPL phase in the porous media as well as the NAPL components that dissolve in the aqueous phase. Ethanol is miscible with both water and NAPL, and

addition of ethanol to a water NAPL mixture enhances the solubilities of hydrocarbon contaminants in the aqueous phase through ethanol's cosolvency effect. The changes in interfacial properties between NAPL-air-water phases in the capillary fringe and NAPL-water phases in the saturated region could also facilitate the movement of the NAPL phase depending on the fluid and porous media properties.

2. The microbial response associated with ethanol and the impact on the biodegradation of BTEX. The presence of ethanol will consume nutrients and electron acceptors that would otherwise be used for the degradation of other hydrocarbons, thereby reducing the natural attenuation of the hydrocarbons (Lovanh et al., 2002). Other possible hazards include generation of ethanol degradation byproducts like methane and volatile fatty acids (VFAs) which could pose an explosion hazard or impact groundwater aesthetics (Ma et al., 2011).

Experimental studies have been conducted regarding the physical modeling of transport characteristics of ethanol blended fuels in the subsurface (Cápiro et al., 2007; He et al., 2011; Ma et al., 2011). However, very limited work has been done to address the phase transport behavior computationally or develop/use a proper model to describe such problems. Most of the modeling work regarding this issue has focused on very specific aspects of the problem, such as the use of an equilibrium phase partitioning model to investigate ethanol's cosolvency effect for different NAPL-water mixtures (Groves, 1988; Lee, 2010; Lee, 2008a); simulation of gasoline remobilization by addition of ethanol on an NAPL source zone and its impact on capillary fringe depression (Yu et al., 2009); and numerical flow simulations to analyze the buoyancy effects with different amount of ethanol added into the NAPL (Molson et al., 2008). The conclusions of these

studies were limited by highly simplified assumptions or were restricted to single-phase flow.

1.4 Problem Statement

Previous studies have focused on whether the "cosolvent effect" caused by the presence of alcohol could potentially increase the dissolved hydrocarbon concentrations in the aqueous phase. These studies have shown that when the ethanol concentration in the aqueous phase is less than 10 % (v/v) that the cosolvent effect would be insignificant for BTEX (Powers et al., 2001a). For typical release scenarios, conventional ethanol fuel blends (E10) are likely to yield ethanol pore water concentrations less than 10% (v/v).

However, the impact of releases of medium- to high-ethanol content fuels on cosolvency are unknown. In addition, ethanol's cosolvency effect may be only one factor that impacts pore water concentrations of hydrocarbons. The complex phase behavior at the source region caused by ethanol may result in different NAPL source behavior which may directly impact the longer-term dissolution characteristics of BTEX from the residual NAPL after ethanol has been depleted from the source.

In this study, experiments were conducted to investigate the transport behavior of various alcohol NAPL fuel mixtures released in the subsurface to better answer the question: what are the principal potential impacts from a release of alcohol blended gasoline to the subsurface on groundwater quality. The main focus was on ethanol gasoline fuel blends. The specific topics investigated in this study were:

(1) The level of alcohol and hydrocarbon pore water concentrations that can be expected near the source of a spill, and the longevity of these concentrations.

(2) The impact of alcohol content in the gasoline on the size and distribution of the NAPL source that is generated.

(3) Transport characteristics of the alcohol plume for fuel blends with various alcohol content, focusing on the impact of buoyancy on the transport of alcohols following a release and the corresponding hydrocarbon concentrations in the dissolved plume.

(4) Longer-term dissolution characteristics of BTEX from different NAPL distributions generated from releases of various alcohol fuel blends.

In addition, due to the complex equilibrium phase behavior and other physical-chemical properties associated with alcohol-water-gasoline mixtures, a multi-phase flow simulator (UTCEM) was used to model transport of the dissolved ethanol and hydrocarbon plume and to model NAPL source generation/migration. Numerical simulations were compared with the results of physical model experiments. Simulations were also used to determine the contributions of the following properties to the overall transport characteristics associated with releases of alcohol fuel blends: viscosity, interfacial tension, relative permeability, and capillary pressure.

CHAPTER 2 LITERATURE REVIEW

2.1 Introduction

For better understanding of the transport and displacement behavior of spills of alcohol blended fuels in porous media as well as for modeling purposes, it is essential to acquire accurate petrophysical properties for the systems of interest. Properties that determine multiphase fluid transport behavior include: phase equilibria, interfacial tension, fluid phase densities, viscosities, etc. Among these properties, a good phase equilibria model for the NAPL-alcohol-water system is of primary importance. Phase equilibria data are available for several alcohol-hydrocarbon-water systems. Quantitative frameworks based on theoretical equation of state models as well as empirical or semi-empirical models can be used to model phase equilibria concentration data for a specific system. Empirical models can provide excellent fits to experimental data and provide for more efficient multi-phase flow simulations than the more rigorous phase equilibria models. Recent ethanol-hydrocarbon-water system phase equilibria data and corresponding phase equilibria models were incorporated into this research.

Gasoline containing ethanol spill studies have been conducted at various scales. Two-dimensional (2-D) laboratory physical model experiments are effective for characterizing source generation, migration, partitioning, and transport of the dissolved plumes. Visualization studies using hydrophilic and hydrophobic dyes have been used to help investigate partitioning and transport behavior of the dissolved alcohol and hydrocarbon aqueous phase plume and the distribution of the immobile residual hydrocarbon phase, respectively. As a validation and extension of the laboratory-scale work, three-dimensional (3-D) field scale studies have also been conducted to

quantitatively measure hydrocarbon saturation and concentration profiles for releases of ethanol blended fuels. These studies have focused on releases in the vadose zone. In this chapter, a summary of the results of these laboratory and field measurements along with related numerical modeling studies to characterize observed source behavior is presented.

2.2 Phase Behavior and Modeling

The alcohol-NAPL-water phase behavior plays a key role in the transport behavior of an alcohol fuel mixture released to the subsurface. Phase equilibria affect how much hydrocarbon partitions and transports with the dissolved alcohol plume, and how much hydrocarbon phase separates from the fuel mixture forming trapped NAPL. The concentrations of components in the various phases also affect fluid properties such as density, IFT, and viscosity which also impact transport.

For ethanol-hydrocarbon-water systems, phase composition measurements from partitioning experiments suggest that ethanol preferentially partitions to the aqueous phase relative to the non-aqueous phase (Heermann et al., 1998; Lee et al., 2004). Phase diagrams available in the literature usually use a single gasoline component to represent the NAPL component in a ternary diagram. Because gasoline is not a pure component, if one wants to generate an accurate phase partitioning model, phase equilibrium data acquired from laboratory experiments specifically designed for the target alcohol-gasoline-water system should be used. Pseudo-ternary diagrams are commonly used to illustrate the phase behavior of ethanol-gasoline-water systems. For an ethanol-gasoline-water system, it is most convenient to group the light hydrocarbons as a pseudo-component with cosolvent (alcohol) and water as the other two components in the ternary diagram.

Oliviera (1997) investigated the equilibrium phase partitioning behavior of the ethanol-gasoline-water system. Gasoline API-91-01 was used in his phase partitioning experiments. A total of 18 stock solutions was prepared for the determination of the binodal curve. Among these 18 solutions, ten were water and ethanol mixtures with ethanol volume fractions that varied from 10% to 80%. The other eight were different mixtures of ethanol and gasoline. The water-ethanol solutions were added to pure gasoline, and the gasoline-ethanol solutions were added to pure water. The phase diagram was obtained by the cloud-point technique. The mixtures were continuously agitated during the addition of the stock solutions for 24 hours to allow for equilibration. Eighteen compositional points were used to construct the binodal curve for the phase diagram. Both refractive index and density of each final solution were measured. To determine the tie lines, the compositions of the initial points that would fall within the two-phase region were selected based on previously published data (Letcher et al., 1986). Refractive indices for the two separate phases were measured and interpolated to achieve the end point concentration of the tie lines. Separate UV analyses were also conducted for comparison. The phase diagram generated from Oliveira's work was used for developing the phase equilibrium model used for numerical simulations for this research. The ternary phase diagram can be found in Figure 5.1 in Chapter 5.

Oliveira also measured the IFT between the oleic and aqueous phases for the various phase diagram tie-line concentrations. The phase compositional data and the corresponding IFT data measured by Oliveira were used as the basis for the IFT model used in this study. More details on the experimental procedures and methods used to determine the IFTs can be found in Oliveira's dissertation (1997).

Researchers have also used rigorous thermodynamic phase equilibrium models to develop ternary phase diagrams. UNIFAC (universal functional activity coefficient) has been used extensively to estimate the activity coefficients of each component in each phase based on a group contribution method. Once activity coefficients are known, by equating the chemical activities of a hydrocarbon component between the two phases, concentrations can be determined. Lee (2008a) used UNIFAC to investigate the equilibrium phase partitioning behavior of ethanol, isopropanol, and methanol in a two-phase liquid-liquid system consisting of water and individual BTEX components. The activity coefficients were estimated assuming the activity coefficient is composed of a combinatorial part and a residual part (Fredenslund et al., 1977). Appropriate UNIFAC group contribution parameters for the three alcohols and BTEX compounds were used in the model. The model initially determines the equilibrium mole fraction of the NAPL in the aqueous phase and the mole fraction of water in the NAPL phase, then the cosolvent was added and increased incrementally in the aqueous phase and the equilibrium mole fractions of other component were calculated for both phases until the plait point (where the composition of the two phases are equal) is reached. The UNIFAC-derived ternary phase diagrams showed fairly good agreement with the experimental data. The slopes of the simulated tie lines for all the cases matched the experimental slopes except for the low ethanol concentration. The author also conducted experiments to examine the phase separation point (mole fractions) by incrementally adding distilled water (0.1 ml) into a blend of 85% (v/v) alcohol and 15% NAPL (20 ml). The accuracy of the binodal curves derived from the UNIFAC model predictions was determined. The results showed good

agreement for the mixtures containing ethanol but not for mixtures containing isopropanol.

Although UNIFAC provides a theoretical framework for assessing phase behavior and cosolvency, its applicability is highly dependent on the systems that are being assessed. Due to the complex composition of a commercial gasoline, using a rigorous thermodynamic approach is computationally inefficient. In this study, an empirical model was adapted to calculate the phase equilibria data to provide a more efficient, yet accurate quantitative description of the phase equilibrium properties for a specified alcohol-gasoline-water system. This empirical approach is described in Chapter 5.

2.3 Laboratory Scale Studies of Ethanol Blended Fuel Spills in the Subsurface

Physical modeling experiments, an effective method for characterizing multiphase flow and transport, have been used to study source generation and plume transport processes. One-dimensional (1-D) and 2-D spill experiments have been conducted in the unsaturated zone to investigate the movement of gasoline and the partitioning behavior of ethanol. McDowell et al. (2003) conducted four 2-D spill experiments with ethanol-free gasoline and E10 gasohol released into the vadose zone to investigate the source behavior of the NAPL phase as well as the partitioning behavior of ethanol. Different dyes were used for visualization purposes. Immediately after the release, partitioning of ethanol from the NAPL phase into the pore water was observed. For a small E10 release, ethanol did not have a significant impact on the residual NAPL saturation and its distribution once the NAPL migrated downward to the capillary zone. This is due to ethanol partitioning from the fuel to pore water and remaining in the pore water within the

vadoze zone above the capillary fringe. Due to the enriched ethanol concentration in the vadose zone, the residual NAPL saturation was significantly reduced near the spill location. For a larger size spill, the amount of ethanol was sufficient to reach the capillary zone and caused a localized enrichment of the NAPL saturation upon its residual. Changes in interfacial properties, phase partitioning and density contributed to this overall effect. This series of experiments suggested that the assumption that most mathematical models used to describe the fate and transport of hydrocarbons and ethanol in groundwater was incorrect, which was: after the initial release, the composition of gasoline at the capillary fringe had the same ethanol content as that originally spilled. These experiments also demonstrated that better characterization of source behavior is needed to determine the impacts of alcohol blended fuels on groundwater quality.

Mamonkina (2011) conducted similar laboratory experiments with a 2-D cell by injecting spills with different spill volumes (20-ml, 50-ml and 100-ml spills) for different ethanol-gasoline fuel compositions that ranged from E15 to E85. The depression of the capillary fringe was observed for all the cases investigated and the area of the porous media contaminated with residual NAPL increased with increasing ethanol content for a given volume of fuel spilled, despite the lower hydrocarbon amount for the higher ethanol content fuels. In addition, the capillary fringe height recovered following depletion of ethanol from the system. For E15 and E25 fuels, full recovery of the capillary height occurred in one week. Capillary height recovery occurred in less time for the higher ethanol content fuels due to lower NAPL residual saturations. To simulate a spill in the saturated zone, 20 ml of E15 fuel was injected under the water table. Significant bypassing of groundwater flow around the NAPL region was observed. The

injection created a high NAPL saturation region, and the saturation remained constant even when the groundwater seepage velocity was increased. This is significant since bypassing leads to mass transfer limited dissolution of gasoline components from the NAPL source to pore water instead of equilibrium partitioning.

It has been shown that when an ethanol blended fuel is spilled in sufficient volume to reach the water table, ethanol partitions from the gasoline phase to pore water, along with dissolved NAPL components, and is largely confined to a thin, concentrated layer within the capillary zone (Cápiro et al., 2007; Stafford et al., 2009). Stafford (2007) conducted a series of 2-D visualization experiments to investigate the various impacts of ethanol release in the subsurface. For the case of a rapid injection of a 20-ml spill of E95 fuel injected 2 cm above the water table, the NAPL rose rapidly, spread and formed a highly saturated NAPL ring. Meanwhile, the ethanol partitioned from NAPL to the aqueous phase and spread out into the upper capillary region, and a reduction of the capillary fringe height was also observed. Another set of experiments was conducted using a larger 2-D tank to investigate the case of a continuous release of E100 onto a pre-existing residual NAPL source. Neat ethanol was spilled onto a source which was created by packing gasoline-contaminated sand into the cell. The ethanol dissolved and mobilized the residual NAPL. After ethanol left the system, redistributed NAPL remained at the edges of where the ethanol plume had been. The NAPL saturations were highest in the more water saturated region with lower saturations in the upper capillary region. Recovery of the capillary fringe height after the ethanol level was reduced below 25% (v/v) was observed, but complete recovery was not obtained by the end of the

experiment. More experimental details including ethanol recovery and dissolved NAPL recovery in the effluent can be found in the dissertation of Stafford (2007).

He et al. (2011) investigated the ethanol-enhanced dissolution of BTEX in gasoline near an existing NAPL source using batch partitioning and column experiments. Compared to ethanol-free water, benzene aqueous concentrations are enhanced by a factor of two or more for ethanol aqueous concentrations greater than 0.2 g/cm^3 (25% (v/v)). In column studies, two different volumes of ethanol were injected onto a residually trapped NAPL source. The aqueous concentration enhancement factors varied from 1.7 for benzene to 9.8 for n-octane. Also in this study a 1-D numerical transport model was used to analyze the data from the column experiments. The simulation results suggest that the impact of highly concentrated ethanol on existing gasoline contamination near the source can be reasonably simulated by an equilibrium dissolution model.

These experiments have all demonstrated that ethanol has a significant impact on NAPL source generation behavior. The amount of ethanol in the fuel mixture and the size of the spill are important factors to be considered when evaluating a gasohol spill in the subsurface.

2.4 Field Scale Study

Field investigations on source generation and transport related to alcohol-blended fuel spills are scarce. Most of the alcohol-related field studies have focused on the alcohol's impact on pre-existing NAPL contamination for DNAPLs such as TCE and PCE. The motivation was to investigate the feasibility of using alcohol as a displacing agent to remediate a site contaminated with residual NAPL. However, the observations

from those experiments also provided insights regarding the impact of ethanol on the mobility of the NAPL which is a principal goal of the research in this dissertation.

Jawitz et al. (2000) conducted an ethanol flushing experiment at a dry cleaner contaminated site in Jacksonville, Florida. This site was sandy soil contaminated with PCE that migrated below the water table. Tracer tests and in-situ alcohol flushing were conducted using three injection wells and six recovery wells. Partitioning tracer tests conducted before the alcohol flood provided an estimate of about 68 L of PCE within the zone swept by the wells. The test zone was flushed with 2 pore volumes of a 95% (v/v) ethanol and 5% (v/v) water mixture over a period of 3 days. Alcohol flushing removed approximately 43 L of PCE from the test zone (62% removal effectiveness). These results were in agreement with soil core data that indicated approximately 65% removal and a post-flushing partitioning tracer test that indicated approximately 26 L of PCE remaining (63% removal). Alcohol flushing successfully mobilized and removed a substantial volume of DNAPL, and the authors claimed that the evidence indicated that continued alcohol flushing would have resulted in a greater NAPL removal effectiveness. Based on the field experiment results, Liang et al. (2008) used a three-dimensional, compositional, multiphase flow simulator, UTCHEM, to model the field data. The simulation was carried out in three stages: first, an uncalibrated model was developed, where the simulation result roughly reproduced the alcohol recovery but not for PCE; then, the permeability model was refined to successfully match the breakthrough concentration of the alcohol, but PCE recovery was still accurately predicted; at the final stage, the initial PCE distribution was adjusted in order to achieve a good fit to the PCE effluent concentrations. This work indicated that UTCHEM can be used to model

alcohol, NAPL, and aqueous phase transport behavior. However, detailed site petro-physical data are usually needed to increase the model performance that includes information on the initial NAPL distribution and aquifer heterogeneity.

Freitas et al. (2011a) and Freitas et al. (2011b) conducted a series of field studies to investigate the fate and transport of gasoline containing oxygenates following a release in the unsaturated zone. The field experiment was conducted at a field site at a Canadian Air Force Base in Borden, Ontario. During the experiment, a total of 200 L of an E10 gasoline mixture containing 4.5% MTBE was released in the unsaturated zone, into a trench that was 20 cm deep and about 32 cm above the water table. Multilevel groundwater sampling wells were installed in three rows perpendicular to the water table; a total of 594 sampling points were employed. Three wells located downgradient of the source (RA-W06, RA-W07 and RB-W07) were sampled frequently to evaluate the evolution of the groundwater and capillary fringe water concentrations with time. Also, multiple wells at Row A were sampled periodically to provide a detailed cross-section of the dissolved plumes. Samples were analyzed for BTEX, and for TMB (tri-methylbenzenes), naphthalene, ethanol, MTBE and TBA (tert-butyl alcohol). Soil core samples were also taken to measure the distribution of the contaminants. According to the core sample measurements, most of the ethanol was retained in the source, above the capillary fringe which caused a delay in the time required for ethanol to be detected in the downgradient groundwater wells. For spills in the unsaturated zone, due to rapid phase separation in the unsaturated zone, by the time the NAPL phase reached the capillary zone, ethanol partitioned from NAPL into the pore water in the unsaturated zone. Only minor changes in the distribution of ethanol were noted following oscillations in the

water table. The authors claimed that due to this rapid partitioning of ethanol from NAPL to the pore water in the unsaturated zone, the leading edge of the dissolved hydrocarbon plume did not contain significant ethanol concentrations; therefore there was no enhanced solubility of hydrocarbons and no decrease in bioattenuation for hydrocarbons due to ethanol was anticipated. This conclusion may only be partially true. It is possible that the dissolved ethanol plume was missed (not sampled) as a result of vertical migration of the plume due to buoyancy. Due to cosolvency, the separated ethanol plume could have dissolved a considerable amount of hydrocarbons. Those dissolved hydrocarbons may phase separate and form NAPL further downstream as the ethanol plume is diluted by pore water. Another important factor that needs to be considered is that different ethanol content in the fuel mixture causes different partitioning and migration behavior that will result in different residual NAPL distributions following a spill. Previous studies have shown that the size and shape of the residual NAPL also has a significant impact on NAPL dissolution (Powers et al., 1992).

2.5 Numerical Models

Modeling efforts focusing on characterizing the impact of a cosolvent in gasoline on the fate and transport of light hydrocarbon contaminants such as BTEX are increasing due to the increasing use of ethanol in gasoline. Most of the recent work has used a single phase dissolution model to characterize the effect of ethanol on the transport behavior of the hydrocarbon contaminant dissolved plume in saturated porous media.

In Molson's paper (Molson et al., 2008), the dissolution and transport of plume containing dissolved hydrocarbons was simulated with BIONAPL, an advective-dispersive transport model. In his study, the dissolution rate was fixed and assumed to be

equilibrium dissolution. To incorporate the enhanced dissolution caused by ethanol, an enhancement factor was defined based on a linear cosolvency model (Ji et al., 1998). The model also included biodegradation of dissolved hydrocarbon contaminants. The model also assumed the fluid viscosity of the plume was constant. The effects of density were considered. The results of the simulation confirmed that buoyancy was significant near the source of the spill in high-ethanol content gasoline spill cases, but that the effect would decrease further downstream as the plume dispersed and degraded. One of the greatest limitations of this single-phase simulation was that the NAPL source was assumed constant throughout the simulation, thereby neglecting the impact of ethanol on the distribution of the NAPL source.

Yu et al. (2009) conducted two laboratory experiments of release of ethanol into a residual gasoline source zone in the capillary fringe. Depression of the capillary fringe was observed and residual gasoline was remobilized due to adding the ethanol. It was observed that injection of ethanol caused the NAPL to move downward toward the water table as the capillary fringe collapsed, which resulted in an increase in NAPL saturation. They also developed and applied a multiphase model, CompFlow Bio, to compare with the results. Two distinct processes were modeled: NAPL remobilization and capillary fringe collapse after ethanol was added to the system. The authors claimed that the simulation matched the NAPL remobilization results but did not predict capillary zone collapse. They also claimed that the most significant factor controlling the simulation results was ethanol partitioning. However, they used a constant equilibrium partitioning coefficient to distribute ethanol between the aqueous and non-aqueous phase instead of using a more realistic, non-linear phase equilibrium model that reflects changes in

ethanol partitioning for different aqueous ethanol concentrations. Another limitation was that the IFT between the aqueous and non-aqueous phases was not considered. IFT is dependent on ethanol concentration and would be expected to have an effect on the NAPL distribution in the source zone.

Most of the previous work involving multiphase fluid transport focused on alcohol flooding, the use of alcohol as a cosolvent to remobilize residual hydrocarbon. Thus, those models were specifically designed for enhanced remediation processes to improve the recovery of the DNAPL. Those models typically have rigorous numerical methods for solving multiphase and multicomponent fluid transport processes and can be adapted to many applications. In this study, the multiphase, multicomponent simulator, UTCHEM, was used to provide insights on effects that were neglected in the single-phase model studies. The main objective was to provide a better understanding regarding the impact of ethanol fuel blends on the size, shape, and distribution of a NAPL source as well as the transport characteristics of the dissolved ethanol plume in order to develop a more accurate evaluation of the transport behavior of the contaminants in the subsurface following releases of ethanol blended fuels.

CHAPTER 3 2-D PHYSICAL MODEL EXPERIMENTS – SOURCE GENERATION

3.1 Introduction

In this chapter the results of the 2-D physical model laboratory experiments that focus on hydrocarbon and ethanol source generation behavior are reported. A series of visualization experiments was conducted to investigate the phase partitioning and transport behavior of ethanol blended fuels released to the subsurface. Various ethanol and NAPL source characteristics resulting from spills of fuel blends with different ethanol contents were investigated.

The objectives were to: (1) use visualization studies to characterize phase partitioning behavior of the ethanol content in the fuel mixture once the fuel mixture was released into the aquifer, the transport behavior of the ethanol plume after it partitioned from the NAPL phase to the aqueous phase, and the evolution of the NAPL phase; (2) evaluate the dispersion, advection, and buoyancy effects on the transport of the less dense plume under water-saturated flow conditions; (3) use visualization studies to characterize residual NAPL distributions generated from different ethanol blended fuel spills (these residual NAPL distributions were also used for subsequent dissolution studies); (4) and provide experimental data for numerical model development and analysis.

3.2 Materials and Methods

3.2.1 Configuration

The laboratory experiments were carried out in a quasi-2-D glass tank as shown in Figure 3.1a. The design of the 2-D tank and the selection of the media allowed for good visualization of the movement of the aqueous phase plume and the NAPL phase by using

different dyes. The tank consisted of two tempered glass walls and an acrylic frame. The size of the tank provided for a sufficient number of sampling ports for quantitative analysis of the solute concentrations in the pore water.

The dimensions of the tank were 116 cm × 58 cm × 2 cm (Length×Height×Width). The thickness of the tank was assumed to be small enough that transverse transport was negligible. The water table level could be adjusted using three two-way valves located at heights of 4 cm, 14 cm, and 24 cm from the bottom of the tank. For this study, the water table was fixed at the top of the sand to create a fully saturated aquifer. Continuous groundwater flow was introduced into the tank using a Masterflex pump (Cole-Parmer) pumping deionized (DI) water directly into the aquifer using a port pre-packed at the same level as, but upstream of, the fuel injection port. Effluent was designed to flow through multiple holes distributed on the side of the cell. The effluent flow was then collected in a reservoir with dimensions of 4.5 cm × 55 cm × 4 cm (Length×Height×Width). The water level was controlled at a constant level by siphoning into an effluent reservoir (Figure 3.1b). The ethanol fuel blends were injected into the aquifer using a second Masterflex pump. Aqueous samples were withdrawn from the aquifer using specially designed stainless steel needles (Sigma-Aldrich) pre-packed at the locations of interest.

The groundwater inlet/outlet configurations, fuel injection port, pore water sampling ports and the dimensions of the aquifer system are shown in Figure 3.1b.

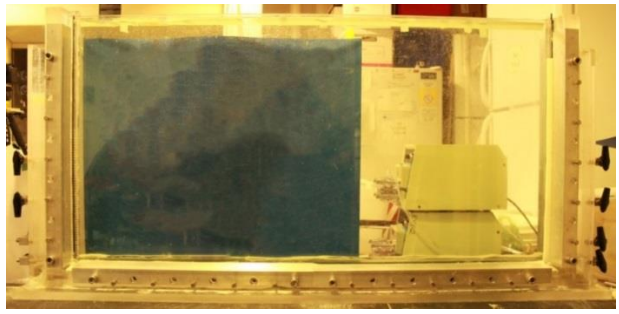

(a)

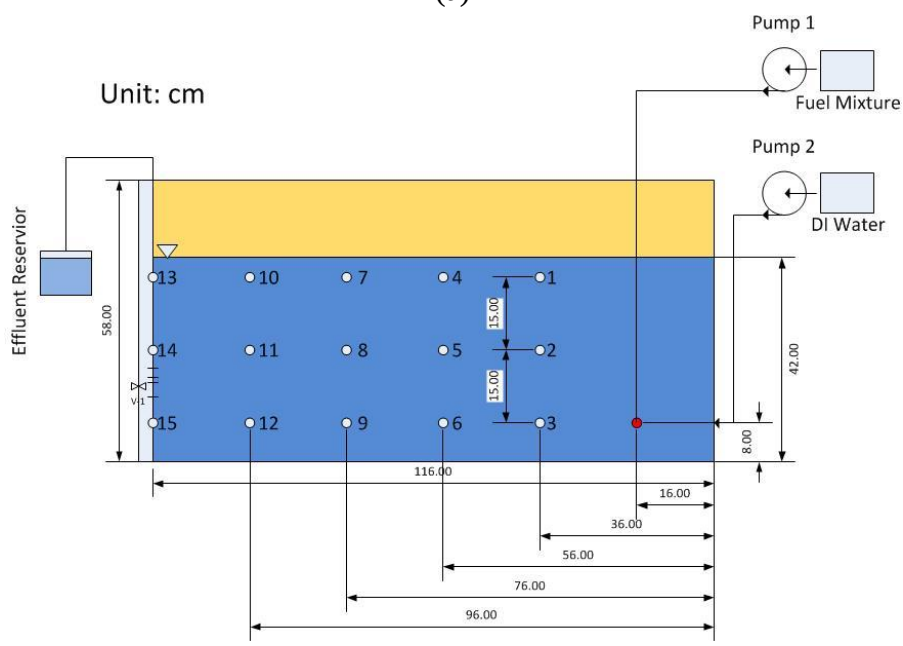

(b)

Figure 3.1 (a) Photograph of 2-D glass model aquifer; (b) 2-D physical model aquifer setup and dimensions. The red circle is the ethanol/hydrocarbon fuel injection port and white circles are the pore water sampling ports.

3.2.2 Fluids and Dyes

The NAPL used in this study was a synthetic gasoline consisting of a hydrocarbon mixture of benzene, toluene, m-xylene, 1,2,4-trimethylbenzene (TMB), and isooctane. The weight fractions of BTX in the mixture were similar to those found in gasoline. Those chemicals were ACS reagent grade products (purity ≥ 98 %) purchased from Sigma-Aldrich. The physical and chemical properties of these hydrocarbon components

can be found in Table 3.1. The ethanol used for the experiments was 200 proof ethyl alcohol manufactured by AAPER Alcohol and Chemical Co.

Dyes with different aqueous affinity were added to the fuel mixtures. A hydrophobic dye (Sudan-IV, red) was used to visualize NAPL phase movement as well as the residual NAPL distribution. A hydrophilic dye (Fluorescein, yellow) which has similar partition characteristics as ethanol (He, 2002; McDowell et al., 2003) was used to show the partitioning and transport behavior of the alcohol dissolved in the aqueous phase. In addition a dilute propylene glycol dye (green) was used as a non-reactive and non-retarded tracer to track groundwater flow paths and the seepage velocities. DI water was used during packing of the aquifer and was also used for continuous groundwater flow. It was also used for pore water sample dilution prior to quantitative analysis of alcohols and hydrocarbons.

Table 3.1 Physical-chemical properties of the hydrocarbons used in the synthetic gasoline.

Hydrocarbons	MW	Specific Gravity, kg/m^3	Viscosity, Cp [(a)]	Aq. Solubility, mg/L [(a)]	Interfacial Tension (HC-aq.), dynes/cm	Mass Fraction in NAPL	Oil-water partition coefficient, cm^3-w/cm^3-o
Benzene	78.1	0.879	0.60	1780	33.8 [(b)]	0.021	254
Toluene	92.1	0.867	0.56	515	35.4 [(b)]	0.056	1122
***m*-Xylene**	106.2	0.864	0.58	162	36 [(c)]	0.117	4269
1,2,4-TMB	120.2	0.878	-	57	36.4 [(b)]	0.294	12989
***iso*-Octane**	114.2	0.688	0.47	0.7	47.5 [(d)]	0.512	111537

a) Haynes (2013); b) Backes et al. (1990), measured at 25 ^{o}C; c) Cameo Chemicals MSDS sheet; d) Hassan et al. (1953), measured at 30 ^{o}C.

3.2.3 Media and the Packing Method

The 2-D aquifer was packed with Ottawa Federal Fine sand, a fine white sand which had been previously proven to be a good media for visualization of Sudan-IV and Fluorescein (Stafford, 2007). The size distribution of the sand is shown in Table 3.2. A wet packing method was used in which sand was always submerged under the water for each packing increment to minimize air entrapment in the water-saturated region. The sand was packed with small increments (1-cm lifts) to minimize stratification and channeling. Experiments have shown that the best wet packing technique to achieve a homogenous porous media is by deposition of thin layers of saturated sand into water with vibration of the media (Oliviera et al., 1996). However, vibration was not feasible given the size of the aquifer used in this experiment. Manual stirring was used instead during packing. For each packing lift, water was added first, and then the sand was evenly spread from the top of the tank until the lift reached the water level, then a plastic bar was used to stir the layer. Finally, a metal pestle was used to compact the layer. The cycle was repeated until the sand reached the desired height (42 cm from the bottom of the tank). Then the water was drained to the desired level, which was set by the position of the outlet port or by level of the effluent reservoir. Experiments were conducted under water-saturated conditions. The water table was maintained at the surface of the sand in the aquifer to ensure that the system remained saturated throughout the experiment.

The porosity was determined gravimetrically. Sand samples from the saturated region were excavated and weighed. Then the samples were put in an oven to dry at $100^{o}C$ for 12 hours. The dry sand samples were weighed again. The porosity was calculated from the weight difference between the saturated sand samples and the dry

sand samples, and from the densities of dry sand (Specific Gravity = 2.65) and water (Specific Gravity = 1). The same method was used to determine the water saturations at different heights (head vs. water saturation curve) for the unsaturated zone that includes the capillary zone. The measured capillary pressure-water saturation curve can be found in Appendix A.

The intrinsic permeability of the media was estimated to be 5210 mD based on measurements by Mamonkina (2011). This value is consistent with a reported value (5.3 Darcy) for Ottawa Sand (mesh 100-200) measured by Akin et al. (1998). Due to a slightly different packing method to prevent trapped air in the media, the actual permeability of the media for the experiments reported herein may be higher than 5210 mD.

Table 3.2 Ottawa Federal Fine Sieve analysis.

Mesh Size	% Retained	Cum. % retained
30	0	0
40	0.4	0.4
50	40	40.4
70	55.4	95.8
100	3.6	99.4
140	0.6	100
200	0	100

3.2.4 Fixed-volume Releases of Ethanol Fuel Blends

Prior to the each fuel injection experiment, a tracer test using a pulse injection of the hydrophilic dye (diluted propylene glycol) was conducted to characterize the seepage velocity of the groundwater and 2-D transport of a dilute aqueous solute in the aquifer. The DI water was pumped continuously into the aquifer through the inlet port at a flow rate of 2300 cm^3/day. The observed seepage velocity at the level of the injection port for this flow rate was 67 cm/day.

Fixed-volume pulse releases of ethanol fuel blends into the water-saturated aquifer were conducted. Ethanol was blended with the synthetic gasoline to produce ethanol fuel blends of various ethanol contents. A total of five spill cases was studied: 15% ethanol/85% hydrocarbon (E15), 25% ethanol/75% hydrocarbon (E25), 50% ethanol/50% hydrocarbon (E50), 85% ethanol/15% hydrocarbon (E85), and 100% ethanol (E100) (all in vol.%). The groundwater flow rate was the same as that used for the tracer study. A fixed volume, 40 mL, of an ethanol fuel mixture was injected at a constant flow rate of 4 mL/min into the injection port located 8 cm above the bottom of the aquifer. The total injection time was 10 minutes.

3.2.5 Visualization and Analytical Methods

Time-lapse photographs were used to record the transport behavior of the plumes and the evolution of the NAPL saturation distributions. A Canon camera equipped with a tripod was used to take photographs of the aquifer in a fixed location. An Insten remote timer was used to take pictures every 15 minutes throughout the experiment. Photographs were taken starting from the initial spill until the majority of the ethanol was removed from the system, usually two days after the spill. For better image quality, a

halogen field lamp was used to enhance the ambient light. Images were post processed with enhanced color saturation to increase the contrast between the color of the dyes and the color of the sand. Therefore, a better visual recognition of the ethanol plume as well as the NAPL distribution could be achieved.

Image processing software (Photoshop CS4) with a pixel-based image processing approach was used to calculate the average residual NAPL saturation. For each spill experiment, the image taken at the end of the experiment was used (2 days after the initial spill), by then there were no more changes in the NAPL saturation distribution with time. The software was used to count the total pixels inside the residual NAPL region as well as the total pixels of a reference object of known area. By comparing the pixels taken between the reference object and the residual NAPL zone, the area of the residual NAPL impacted zone could be calculated. In most cases images were processed automatically with the software. For some cases in order to distinguish the color intensity of the dye of the NAPL impacted region from background, manual processing was used.

Although using the hydrophilic and hydrophobic dyes worked well as indicators to help visualize the transport characteristics of the ethanol plume as well as the distribution of the NAPL phase, it had certain limitations. Sudan Red associates with the NAPL phase, therefore dissolved hydrocarbon in the aqueous phase could not be identified by Sudan Red. For fluorescein, the color intensity is not a linear function of aqueous concentration. Therefore the concentrations of ethanol in the aqueous phase could not be quantified from the visualization experiments. In order to quantitatively assess pore water impacts of ethanol and hydrocarbon contaminants, pore water concentration analyses were conducted simultaneously with the visualization experiments.

For each spill experiment, pore water was extracted from 15 downstream sampling ports using pre-washed syringes (BD) connected to 19-gauge, 24-inch sampling needles (304 stainless steel syringe needle, noncoring point, Sigma-Aldrich) pre-packed in the aquifer to quantify the ethanol and hydrocarbon concentrations at those sampling locations. Concentration profiles were generated every six hours for the first two days after the ethanol fuel releases. Pore water samples taken from the tank were 0.5 mL in volume and were diluted in a 2-mL vial (gas tight glass vial with a polypropylene cap and PTFE septum with zero head space, Sun-Sri) using DI water. The diluted samples were then injected into a gas chromatograph (Hewlett Packard 5890) equipped with an OI Analytical flame ionization detector (FID)) using an autosampler. The injection volume of each sample was 2 μl. The GC was equipped with a Supelco capillary column (Model SPB-5, 30 m × 0.53 mm × 5 μm). Ethanol, benzene, toluene and m-xylene were measured with a detection limit of 1 mg/L for all compounds. In order to minimize the impact of sampling on the aquifer hydraulics interference, only one sample was taken at a given sampling location every six hours. Due to the number of samples that needed to be analyzed and the fact that samples could not be stored prior to analysis due to potential losses due to volatilization, duplicate injections were not feasible. Only one injection was used for each sample. To ensure the quality of each injection, a known amount of TCE was added as an internal standard into each sample vial prior to injection.

3.3 Results and Discussion

3.3.1 NAPL Source Behavior

The presence of a NAPL phase is indicated by the red color (Sudan Red) in Figures 3.2-3.5. For all of the fuel spill cases investigated (E15, E25, E50, and E85), two

days after the release, all of the ethanol originally present in the fuel partitioned to the aqueous phase, leaving immobile NAPL behind which could not be displaced by groundwater. The distribution of residual NAPL and the transport characteristics of the dissolved ethanol plume varied with ethanol content in the fuel.

The average residual NAPL saturations calculated using imaging software are listed in Table 3.3. Image analysis data are presented in Appendix B. Increasing the ethanol content from E15 to E85 resulted in a smaller amount of hydrocarbon. Thus, it was expected that the average residual NAPL saturation would decrease from low to high ethanol content spills. This is in agreement with what was observed.

Based on the image analyses of the dyed area, immediately after the fuel was injected the injected fluid displaced most of the water originally inside the pores, leaving a very low water saturation. This initial displacement behavior was similar for all the spill cases investigated.

The spreading of the fuel mixture as it was injected occurred uniformly in the radial direction for all of the fuels studied (E15, E25, E50, E85). However, in separate experiments comparing an ethanol-free (E0) spill with E5 and E10 (Figure 3.6), the injection was irregular for ethanol contents less that 15%. This is likely due to ethanol lowering the interfacial tension, and, as a result, the pore entry pressure. This would make fuels containing ethanol less sensitive to heterogeneities (in these experiments due to stratification during packing) in permeability than the fuels with very low ethanol content. The injected non-wetting hydrocarbons enter the pores with the lowest entry pressure. When ethanol concentration was increased to 15 percent, the IFT was low enough to allow the hydrocarbon phase to enter the pores uniformly. Thus the

distribution of the fuel after the injection had very similar shapes for ethanol fuel blends with ethanol contents above 10 %.

For the E15 to E85 fuel experiments, after injection, the horizontal and vertical pressure gradients due to groundwater flow and density differences, respectively, were not sufficient to mobilize the NAPL in the highest saturation region to enter the surrounding pore space, thus this fraction of the NAPL was confined to the injection zone. However, the partitioning and migration of ethanol from the fuels had a significant impact on the migration of a second fraction of NAPL, and the NAPL distribution for this fraction was highly dependent on the ethanol content in the fuel mixture for E15 to E85.

For the E15 spill, the NAPL saturation profile did not vary much with time and was very similar to the profile generated immediately after injection. Water displaced only a small portion of the NAPL at the leading edge (right hand side in Figures 3.2a-d) based on changes in the color intensity of the dye. NAPL was redistributed in the source zone, but the average saturation within the NAPL zone remained constant.

For the E25 spill, the NAPL impacted area increased as ethanol migrated from the source. As ethanol migrated vertically by buoyancy, the pore space was recharged by the surrounding water, and a local redistribution of NAPL was observed. Thus, after ethanol was depleted from the source region, the final NAPL distribution consisted of an upper region with low NAPL saturation and a lower region with high NAPL saturation (Figure 3.3d).

For the E50 spill, formation of NAPL due to phase separation during vertical migration of the concentrated ethanol plume became evident. The vertical migration of ethanol also and had a significant effect on the movement and redistribution of NAPL

inside the source region. The NAPL impacted area increased significantly (relative to E25), and the final overall residual NAPL saturation was more uniform compared to E15 and E25 spill cases (Figure 3.4 d).

For the E85 spill, formation of NAPL due to phase separation during vertical migration and of the concentrated ethanol plume was much more pronounced. The NAPL phase separated at the leading and trailing edges of the ethanol plume, generating a NAPL "ring" of high saturation with low saturation within the core (Figure 3.5 d). The irregular shape formed at the upper region of the residual NAPL had an irregular shape resulting from some instabilities in the movement of the concentrated ethanol (corresponds to Fluorescein's green color) plume (Figure 3.5 b).

Table 3.3 NAPL residual saturation and impacted area formed from release of E15, E25, E50, and E85 fuel blends.

Spill case	NAPL content in the fuel mixture, mL	Average residual NAPL saturation	NAPL impacted area, % of aquifer
E15	34	0.79	1.1
E25	30	0.39	2.0
E50	20	0.19	2.7
E85	6	0.04	3.7

(a) 0 hour after release

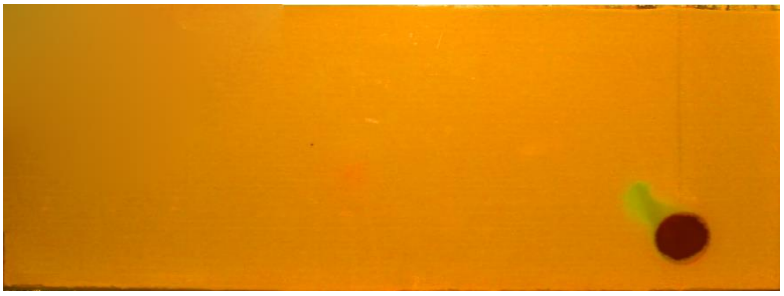

(b) 3 hours after release

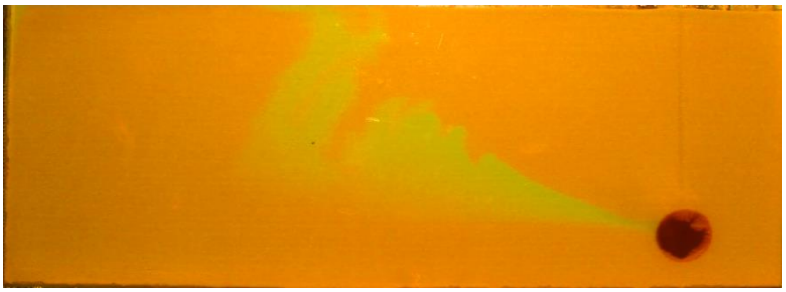

(c) 24 hours after release

(d) 48 hours after release

Figure 3.2 Ethanol plume transport and NAPL saturation profiles for a release of E15 into a saturated aquifer.

(a) 0 hour after release

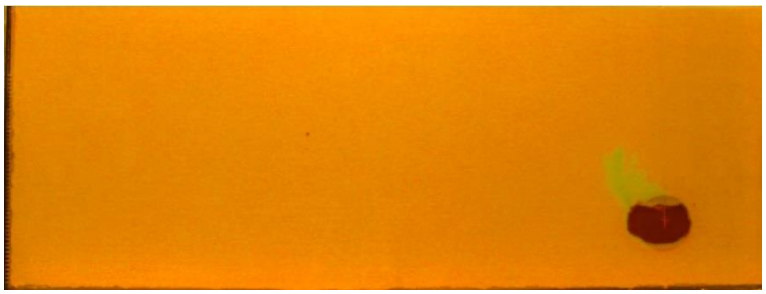

(b) 3 hours after release

(c) 24 hours after release

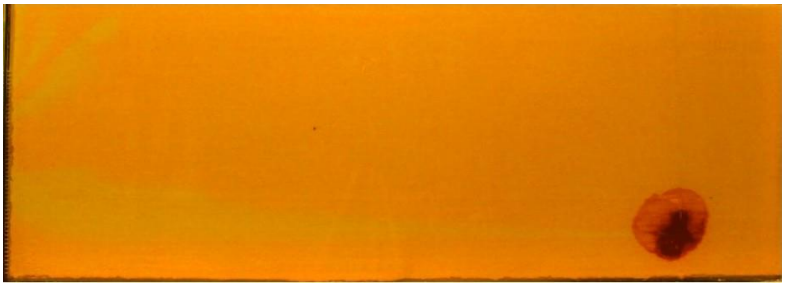

(d) 48 hours after release

Figure 3.3 Ethanol plume transport and NAPL saturation profiles for a release of E25 into a saturated aquifer.

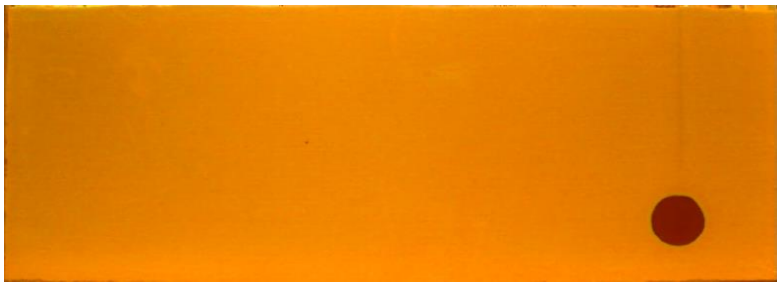

(a) 0 hour after release

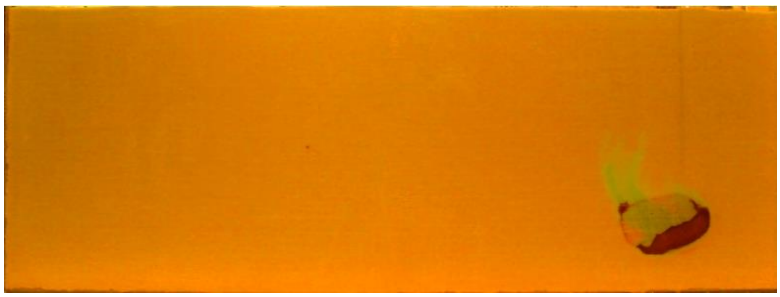

(b) 3 hours after release

(c) 24 hours after release

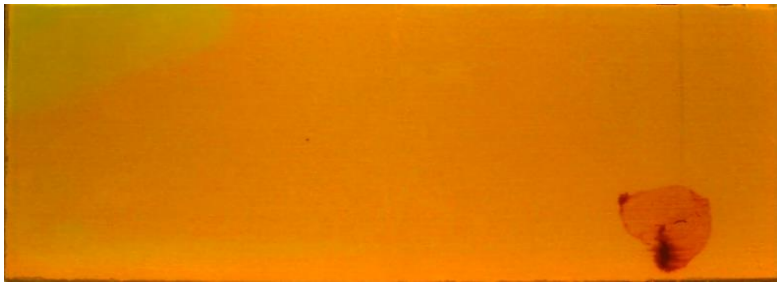

(d) 48 hours after release

Figure 3.4 Ethanol plume transport and NAPL saturation profiles for a release of E50 into a saturated aquifer

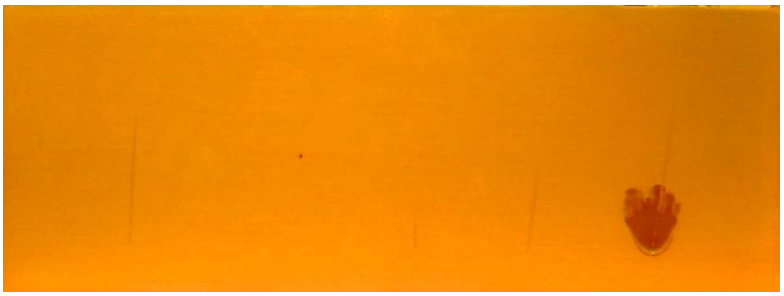

(a) 0 hour after release

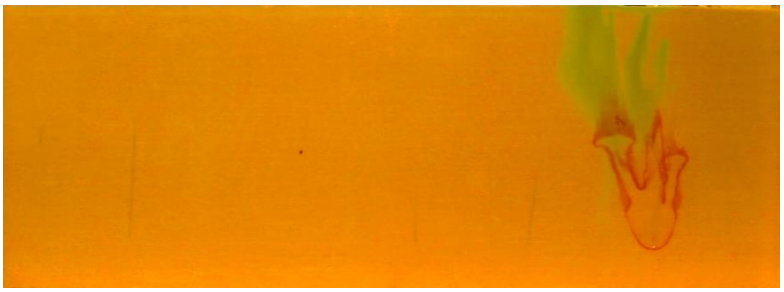

(b) 3 hours after release

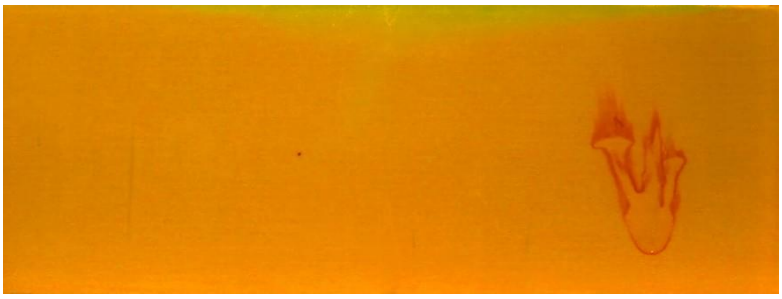

(c) 24 hours after release

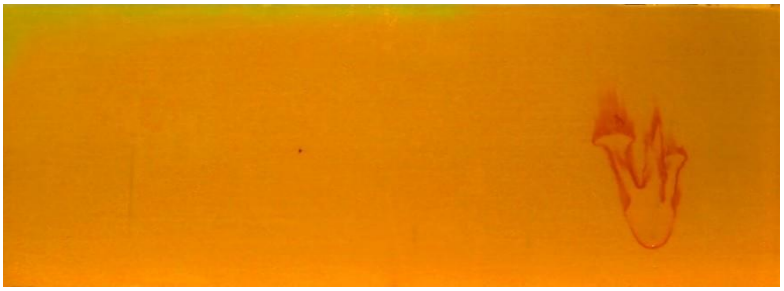

(d) 48 hours after release

Figure 3.5 Ethanol plume transport and NAPL saturation profiles for a release of E85 into a saturated aquifer.

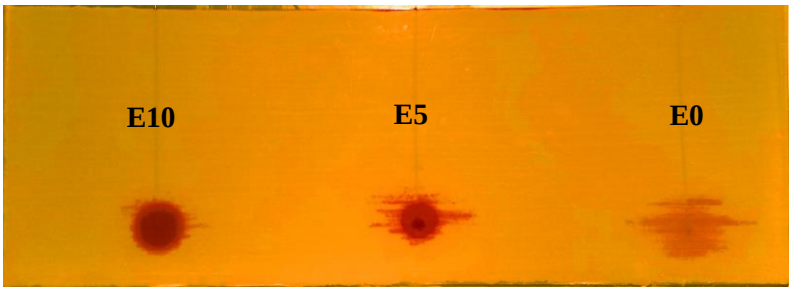

Figure 3.6 NAPL saturation profiles for releases of E0, E5, and E10.

3.3.2 Ethanol Partitioning and Transport Behavior

Ethanol was indicated by Fluorescein (a light green color) in Figures 3.2-3.5 and Figure 3.7. After the fuel was injected, ethanol partitioned from the fuel mixture into the surrounding aqueous phase and migrated due to buoyancy and groundwater flow. Depending on the concentration of the ethanol in the fuel mixture, the plume patterns were different for each spill. The velocities in the horizontal direction were the same due to the same groundwater flow rate, but there was more rapid vertical movement of the ethanol plume for fuel spills with higher ethanol contents.

For E15, E25 and E50 spill cases, while the majority of the ethanol in the fuel mixture partitioned into the aqueous phase immediately after the release, some ethanol remained in the NAPL phase and slowly emanated from the NAPL source until all of the ethanol was displaced by groundwater. Buoyancy resulting from lower densities for ethanol aqueous solutions determined how rapidly the ethanol plume migrated vertically from the NAPL source, and that depended on the concentration of ethanol in the fuel. Since E50 released a higher amount of ethanol compared to the E15 and E25 spills, ethanol plumes were more concentrated. Thus, a more rapid upward migration of the ethanol plume was observed for the E50 spill compared to the E15 and E25 spills. When

buoyancy effects were reduced due to the lower ethanol contents, horizontal groundwater flow controlled the removal of ethanol from the NAPL source. Ethanol released from the E15 spill was displaced by groundwater flow that passed through or around the NAPL impacted region. For E15, some rise in the ethanol plume was observed by the time the plume reached the tank outlet, but this was much less pronounced than for the higher ethanol content spills.

While the majority of the ethanol content for E15 and E25 spills was carried by the groundwater flow through/around the NAPL source, the flow that passed through the NAPL source was limited by the high NAPL saturation at the center area of the NAPL source. Thus, slow removal of ethanol from those areas was observed. The NAPL saturations decreased from E15 to E50 (Table 3.3), and the aqueous phase velocity in the source region also decreased from E15 to E50. Therefore, the time required for all of the ethanol to be displaced from the source also decreased from E15 to E50. The ethanol plumes released from the sources with high NAPL saturation were thin plumes with low ethanol concentration, and the low ethanol concentrations had a small effect on aqueous density yielding a more horizontal plume.

For the E85 spill, the ethanol concentration was high enough to yield a very buoyant plume that rose vertically, directly above the point of injection, to the top boundary of the aquifer. In this case essentially all of the ethanol rose vertically to the top of the aquifer; no release of ethanol from the remaining NAPL was observed. The concentrated layer of ethanol near the top boundary was slowly displaced by the groundwater flow toward the outlet. There was some apparent flow instability in the ethanol plume (Figure 3.5b). As discussed in the previous section, this was most likely

responsible for the irregularly shaped residual NAPL that was formed. This ethanol transport behavior was also observed in the E100 spill experiment (Figure 3.7).

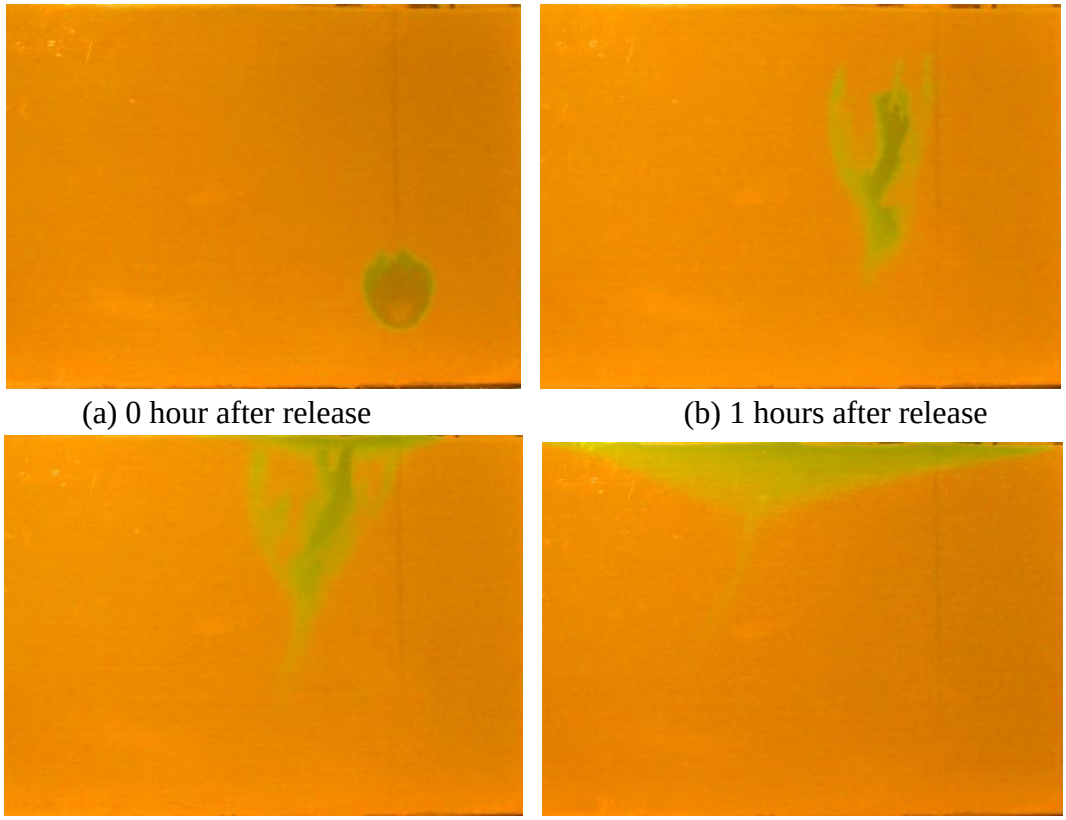

(a) 0 hour after release (b) 1 hours after release

(c) 3 hour after release (d) 6 hours after release

Figure 3.7 Ethanol transport for a release of pure ethanol (E100) into a saturated aquifer.

3.3.3 Quantitative Pore Water Measurements

Pore water concentrations for ethanol and hydrocarbons were measure at several sample locations (Figure 3.1b, and as described in 3.2.5). Results from these measurements are shown in Figures 3.8-3.11 and Table 3.4. The hydrocarbon concentrations are shown in these figures and table as total hydrocarbons (NAPL) to simplify the presentation of results to illustrate the general impact of ethanol on the dissolution and transport behavior of dissolved NAPL components. The concentration measurements of the individual components are listed in Appendix C, and the longer-

term dissolution characteristics of individual hydrocarbon components (BTX and 1,2,4-trimethylbenzene) after ethanol was removed are discussed in Chapter 4.

Table 3.4 Maximum dissolved ethanol and hydrocarbon concentrations and their corresponding locations* from spills of E15, E25, E50, and E85 fuel blends.

Spill case	Max. ethanol conc. (vol.%)	Hydrocarbon conc. associated with the max. ethanol conc. (mg/L)	Max. Hydrocarbon Conc. (mg/L)	Location of max. ethanol conc.	Location of max. hydrocarbon conc.	Time of max. ethanol conc. (hr)	Time of max. hydrocarbon conc. (hr)
E15	1.4	<10	<10	2	-	6	-
E25	1.9	<10	220	2	3	6	24
E50	3.0	208	220	1	9	6	48
E85	7.3	905	905	1	1	6	6

* See Figure 3.1b for sample locations

From the pore water concentration measurements (Figures 3.8-3.11), a clear difference can be observed for spills of fuels for different ethanol contents with respect to how hydrocarbon migrated along with the aqueous phase and how much the hydrocarbon dissolution was enhanced by the ethanol plume. The measured maximum total hydrocarbon concentration and ethanol concentration for each spill is listed in Table 3.4.

The trends observed in ethanol concentrations measured at the downstream sampling locations were generally consistent with the transport characteristics of the ethanol plume observed from the visualization experiments. For the E85 release, the maximum measured ethanol concentration was 7.3 % (v/v), and this occurred above the source of the spill, at sample location 1. The maximum measured ethanol concentration for E50 was 3.0% (v/v) and it was also measured at sample location 1. For E25 and E15, the maximum measured ethanol concentration was 1.9% (v/v) and 1.4 % (v/v),

respectively, and this occurred downstream at sample location 2, which was due to the less buoyant plumes.

For E85 spill, as described in the previous section, as the ethanol plume migrated upward from the spill location, it carried all of the hydrocarbons along with it until phase separation occurred. After phase separation, the concentrated ethanol plume still carried significant levels of dissolved hydrocarbons due to the enhanced solubilities (cosolvency) of the hydrocarbons by ethanol. The maximum total hydrocarbon concentration observed was 905 mg/L and corresponded to the maximum ethanol concentration. These maximum concentrations were measured at sample location 1 (See Figure 3.1b for sample locations), the highest sample location closest to the spill injection point.

For the E25 spill, the dissolved hydrocarbons were measured at the sampling ports that were the same elevation as the hydrocarbon injection port, which indicated that the dissolved hydrocarbon concentrations were controlled by dissolution from the NAPL by groundwater that passed (horizontally) through the NAPL source. Hydrocarbon concentrations were enhanced by ethanol for a short period which corresponded to a pulse of ethanol from the spill, as shown in Figure 3.9. At other times, the measured total hydrocarbon concentrations were at or below the detection limit (10 mg/L). For the E15 spill, hydrocarbons were below the detection limit at all times, thereby indicating that for ethanol contents 15% and below, cosolvency by ethanol is not significant.

For the intermediate ethanol content spill (E50), cosolvency by ethanol elevated the hydrocarbon concentrations in both the upper regions of the aquifer and as well as the lower regions downstream of the source of the spill. Thus, the intermediate content spill

resulted in a wider-spread pore water impact than that for the low (E15, E25) and high (E85) ethanol content spill cases.

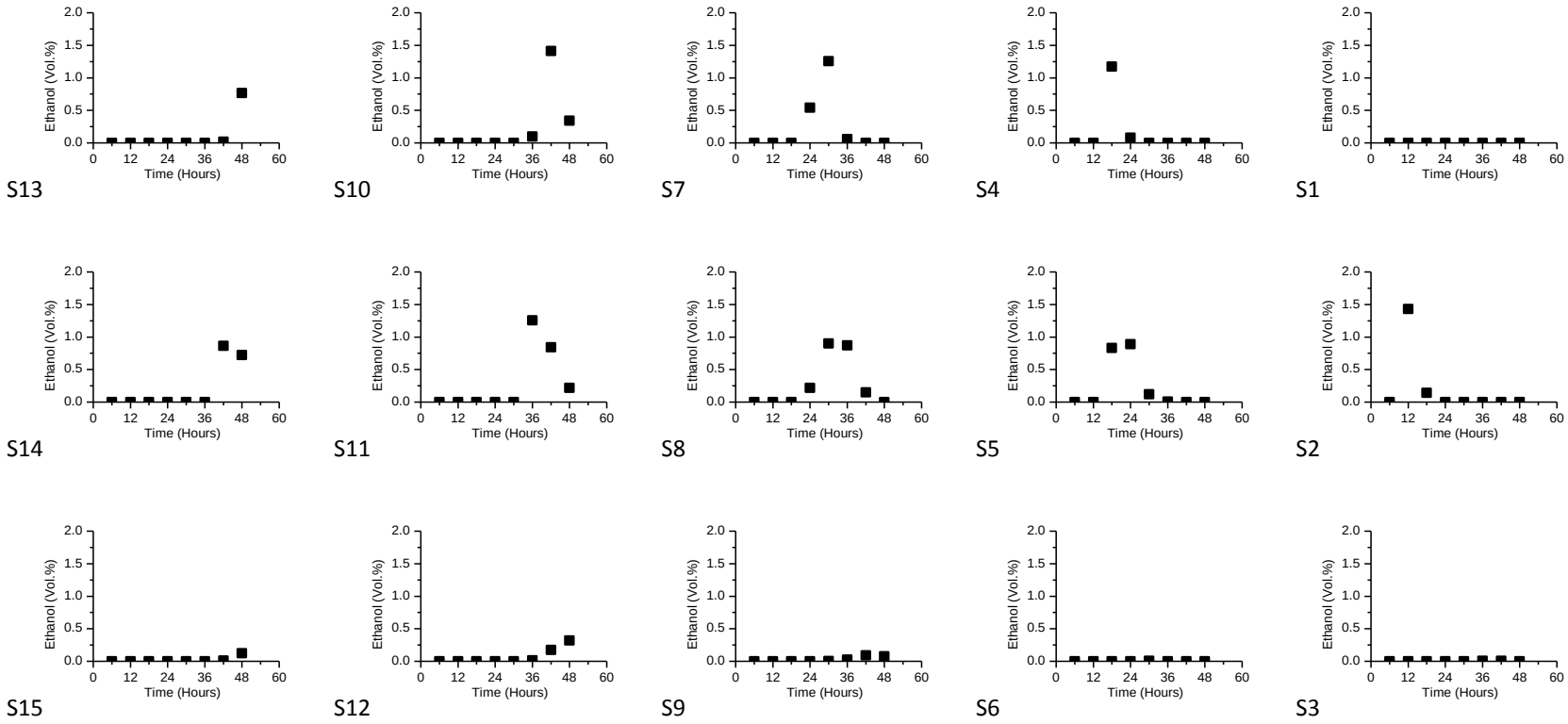

Figure 3.8 E15 Pore water concentrations. Ethanol (filled symbols).

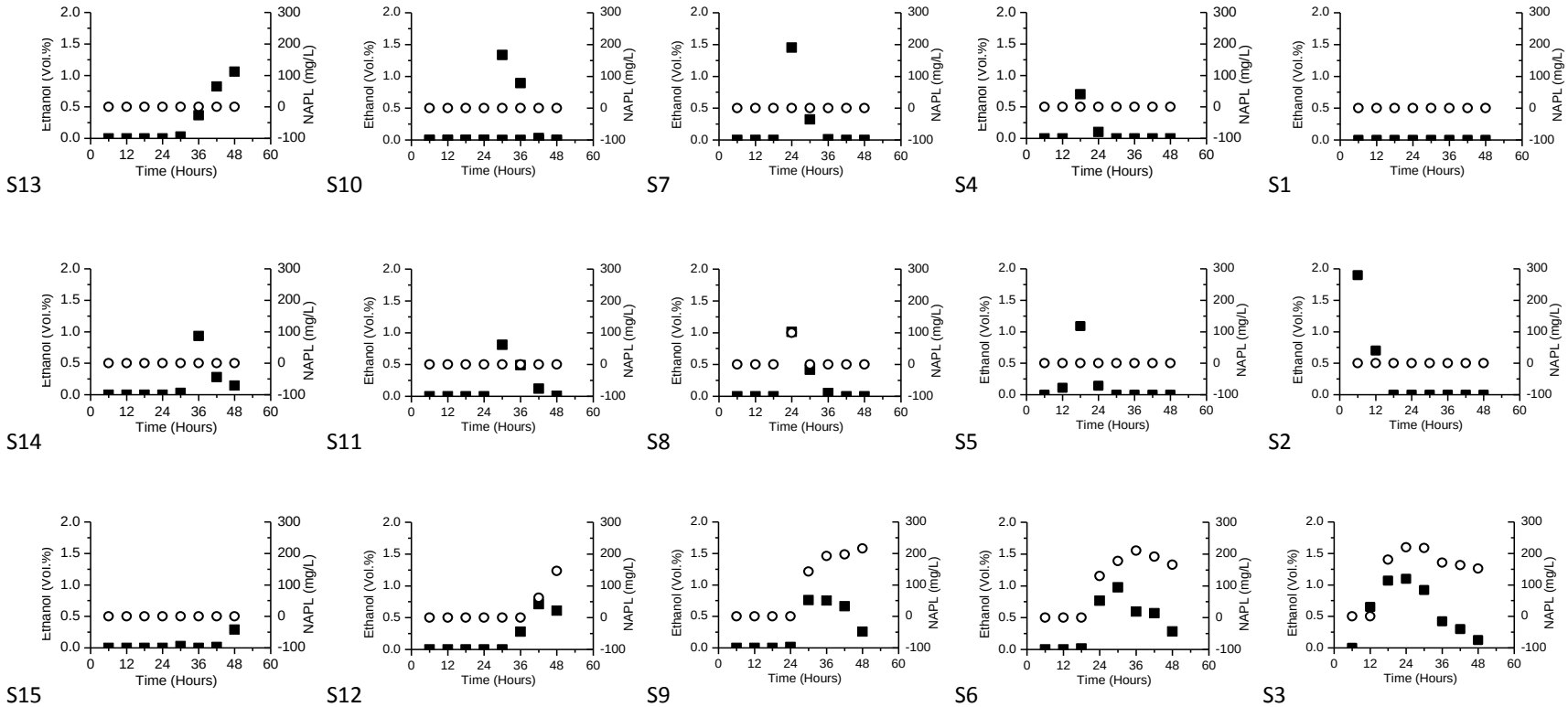

Figure 3.9 E25 Pore water concentrations. Ethanol (filled symbols), total hydrocarbons (NAPL) (open symbols).

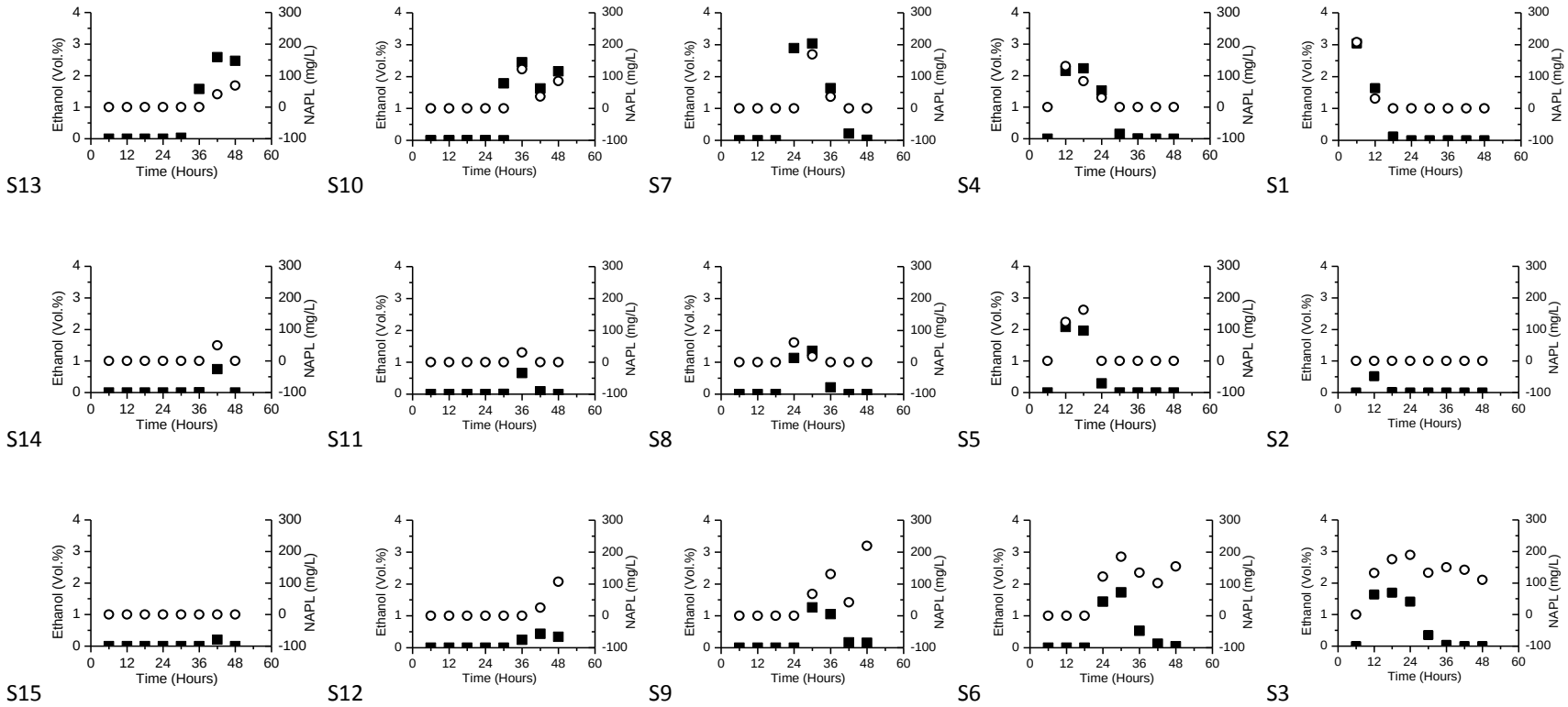

Figure 3.10 E50 Pore water concentrations. Ethanol (filled symbols), total hydrocarbons (NAPL) (open symbols).

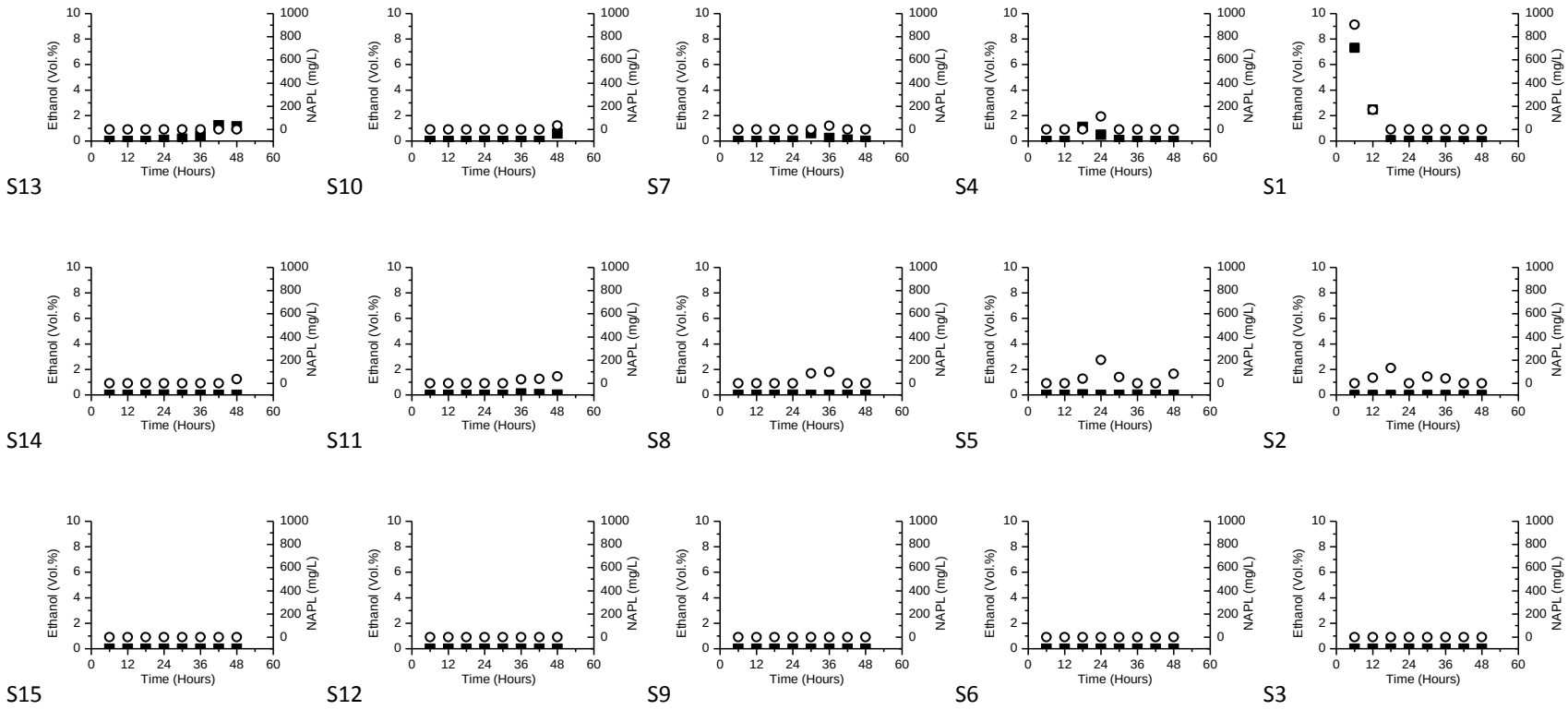

Figure 3.11 E85 Pore water concentrations. Ethanol (filled symbols), total hydrocarbons (NAPL) (open symbols).

CHAPTER 4 2-D PHYSICAL MODEL EXPERIMENTS – DISSOLUTION

4.1 Introduction

For release of an alcohol blended fuel to the subsurface, alcohol enters the surrounding pore water after a spill, leaving the majority of the NAPL content trapped in the pores. As discussed in Chapter 3, the resulting NAPL distribution (size, shape, and NAPL saturation) is highly dependent on the ethanol content in the fuel. These differences in NAPL distributions may lead to different longer-term hydrocarbon (e.g., BTX) dissolution characteristics from the NAPL sources that remain after ethanol has been depleted from the source of the spill.

For example, high NAPL saturations in the source region were observed for E15 and E25 in the 2-D visualization studies discussed in Chapter 3. For those cases, the high NAPL saturation resulted in a low relative permeability for the aqueous phase. Thus, a significant reduction in the groundwater velocity passing through the NAPL contaminated region and potential bypassing of the NAPL by the groundwater flow was expected. This may lead to mass transfer limited dissolution rates which can affect initial (immediately after ethanol has been depleted) pore water concentrations as well as the longevity of the concentrations emanating from the source. However, for the high ethanol content spill case, E85, a low average NAPL saturation was observed. This may allow sufficient contact between the NAPL phase and groundwater to achieve equilibrium dissolution rates which will yield maximum initial pore water concentrations and reduce the longevity of source pore water concentrations. To assess the impact of

NAPL distributions on longer-term hydrocarbon pore water impacts, separate dissolution experiments were conducted for several ethanol fuel blends (E10, E25, E50 and E85).

4.2 Methods

4.2.1 Post-tracer Visualization

Before conducting the pore water concentration analyses, post-tracer (after injection of ethanol fuel blend and formation of NAPL) studies were conducted to visualize how groundwater flows through the residual NAPL sources that were generated from releases of different ethanol-gasoline fuels. The groundwater velocity and the contact area between the flowing aqueous phase and the residual NAPL phase can be inferred from the visualization experiments. The residual NAPL distributions that remained from the E10, E25, E50 and E85 spill experiments described in Chapter 3 were used as the hydrocarbon sources for the dissolution experiments (Figures 3.3d, 3.4d, and 3.5d).

Post-tracer injections were conducted 2 days after the source generation experiments were completed (4 days after fuels were injected). A pulse injection of 400 mL of dilute propylene glycol (green) in DI water was used as a conservative tracer. The tracer was injected at the same flow rate used for normal DI water flow prior to and after tracer injection. The total injection time of the tracer solution was 250 min.

The same time-lapse photography method used for the short-term source generation characterization experiments (Chapter 3.2.5) was also used here. Pictures were taken every 30 min during the 2 days of monitoring of the transport behavior of the groundwater flow. The photos were also post processed to enhance the color of the tracer.

4.2.2 Quantitative Analyses of Dissolved Hydrocarbons

Two weeks after the initial injection, ethanol was depleted from the system. Pore water samples were then taken from the same downstream 15 sampling ports to measure dissolved hydrocarbon concentrations. Different from the short-term pore water sample analyses, for which pore water samples (2 μL) were analyzed by direct injection, larger samples were taken and purge and trap concentration was used to achieve lower detection limits. Pore water samples were taken once a week for three consecutive weeks, generating snapshots of the concentration distributions for individual hydrocarbon components (benzene, toluene, TMB, m-xylene) originally in the synthetic gasoline. Isooctane was also measured but results are not reported herein due to likely volatilization losses (high Henry's Law constant) during sample preparation for analysis.

At each sampling location, 0.5 mL of pore water was taken using a pre-washed 3-mL syringe (BD). Then the samples were instantly transferred to 5-mL vials and filled with 4.5 mL of DI water to eliminate any head space. The 5-mL samples were added to the purge and trap autosampler (Tekmar, Model 2016), which transferred individual samples to the concentrator (Tekmar, Model 3150). Samples were purged and concentrated and transferred directly to a GC (Agilent 6890N) equipped with a capillary column (J&W Scientific, model DB-624, 20 m length, 0.130 mm diameter) and a mass selective detector (Agilent 5973) for quantitative analysis. The detection limit was 1.0 μg/L for all the target hydrocarbons.

4.3 Results and Discussion

4.3.1 Post-tracer Visualization

When pore space is partially occupied by the non-wetting phase, the wetting phase fluid velocity will be reduced significantly due to the non-wetting phase occupying the larger pores. Based on the results of the post-tracer studies, the groundwater stream lines were altered differently when the flow front was in contact with the residual NAPL impacted regions.

The residual saturation regions generated from the E15, E25, and E50 cases had average residual NAPL saturations of 0.79, 0.39, and 0.19, respectively. It was observed within the residual NAPL region, that the NAPL saturation was not uniform, as indicated by the intensity of the Sudan Red dye (Figures 4.1-4.4). It can be seen that the flow velocity was reduced before entering the NAPL impacted region which resulted in a "concave" shape of the leading edge of the tracer.

For the E15 case, most of the groundwater bypassed the NAPL impacted region and only a very thin stream of the tracer was able to pass through, as indicated by a tracer "tail" that slowly emanated from the NAPL source. The tracer tail indicated that some groundwater passed through the NAPL at a significantly reduced velocity.

For the E25 and the E50 cases, the groundwater flow was able to enter regions with low NAPL saturations (indicated by a light red color) with slightly reduced velocities relative to the tracer velocity with no NAPL present. For these regions equilibrium dissolution from NAPL would be expected to occur resulting in high pore water concentrations from groundwater passing through these low NAPL saturation regions. The tracer results also showed that groundwater bypassed the high NAPL

saturation zone leaving a similar tracer “tail” as observed for the E15 case. This indicates that it may take a much longer time for the hydrocarbons to deplete from those highly NAPL saturated regions resulting from either mass transfer limited dissolution from the bypassed NAPL to groundwater or from slow advection of groundwater through the high saturation NAPL region.

For the E85 spill, the tracer flow was only slightly impacted by the residual NAPL due to the overall low NAPL saturation; the tracer velocity was reduced when passing through the left top region of the NAPL impacted area. A darker red color also indicated a higher NAPL saturation. However, the NAPL saturation was not high enough to create a tracer “tail” like that observed in the low ethanol content spill cases. Similar to the E25 and E50 cases, these tracer results indicate that for E85 spills, equilibrium dissolution from NAPL would be expected to occur resulting in initially (after ethanol has left the source) high hydrocarbon pore water concentrations from groundwater passing through the low NAPL saturation source. However, it would be expected that the source concentrations would deplete much more rapidly than for E25 and E50, due to the low NAPL saturation and equilibrium dissolution conditions, resulting in shorter-lived sources of dissolved hydrocarbons.

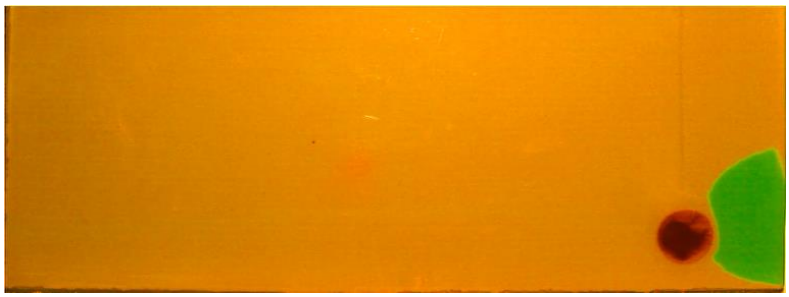

(a) 3 hours

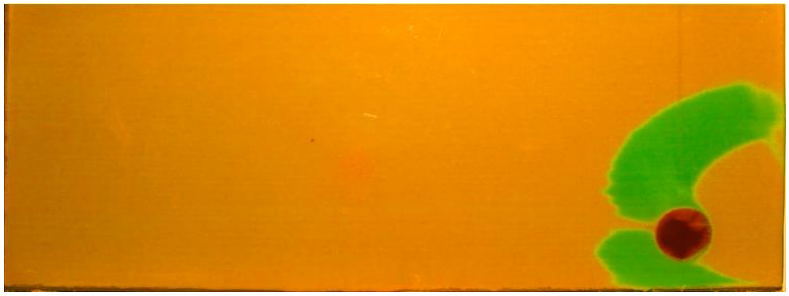

(b) 9 hours

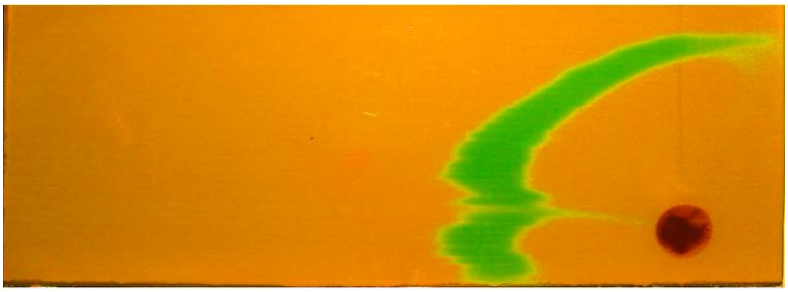

(c) 15 hours

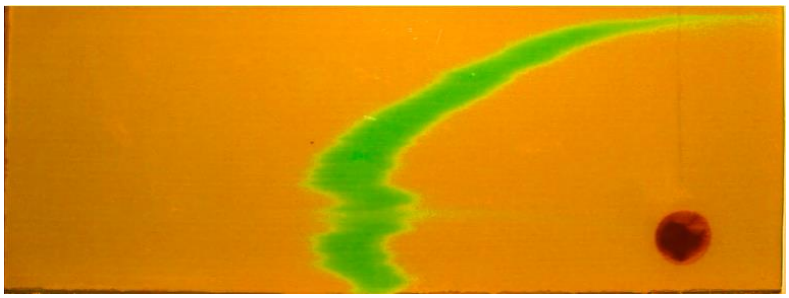

(d) 24 hours

Figure 4.1 Post-tracer study of groundwater passing through the residual NAPL source formed from an E15 spill.

(a) 3 hours

(b) 9 hours

(c) 15 hours

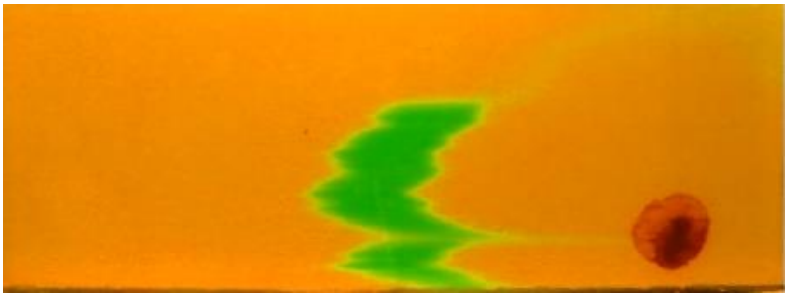

(d) 24 hours

Figure 4.2 Post-tracer study of groundwater passing through the residual NAPL source formed from an E25 spill.

(a) 3 hours

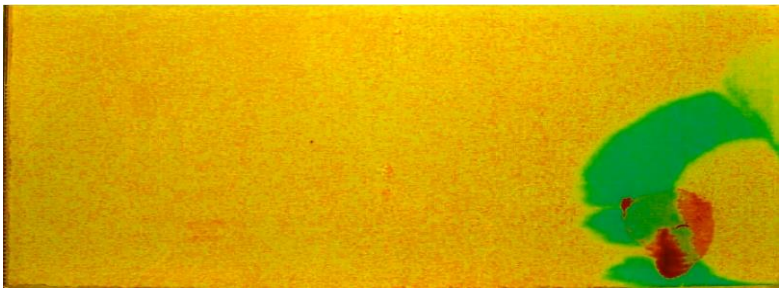

(b) 9 hours

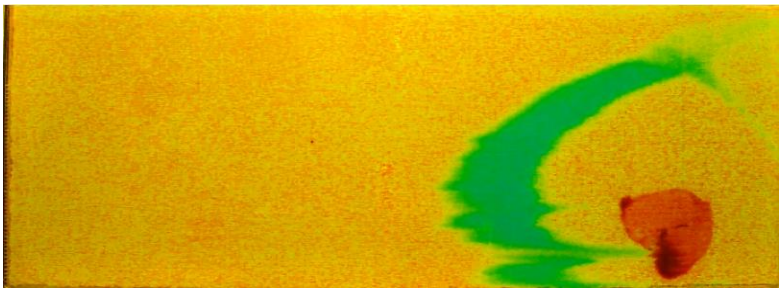

(c) 15 hours

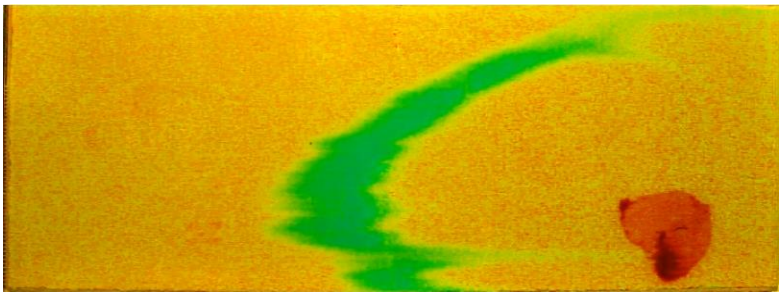

(d) 24 hours

Figure 4.3 Post-tracer study of groundwater passing through the residual NAPL source formed from an E50 spill.

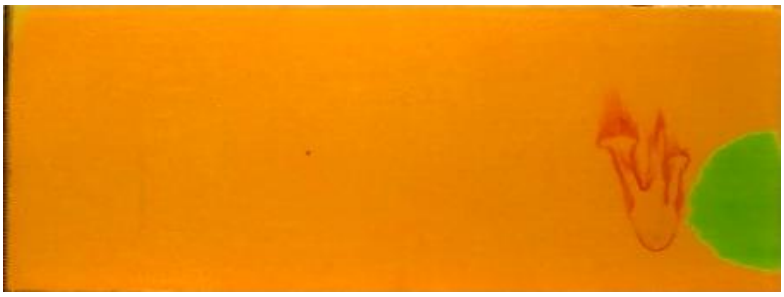

(a) 3 hours

(b) 9 hours

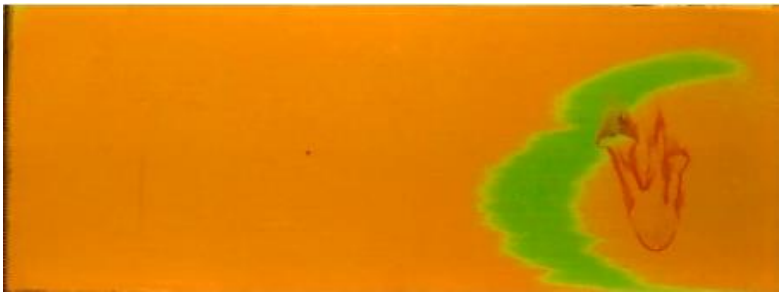

(c) 15 hours

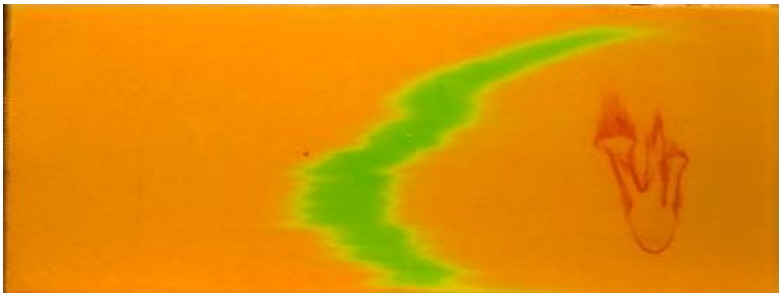

(d) 24 hours

Figure 4.4 Post-tracer study of groundwater passing through the residual NAPL source formed from an E85 spill.

4.3.2 Hydrocarbon Concentrations in Pore Water

Pore water hydrocarbon concentration measurement results are shown in Figures 4.5-4.7, and the highest concentrations from these measurements are listed in Table 4.1. For every spill case, hydrocarbon concentrations were highest at the sample ports located at the same elevation as the residual NAPL source, and the hydrocarbon concentrations at all locations downstream of the source at the same elevation were similar. This suggested that a thin, pseudo steady-state plume was formed from the residual NAPL source with a negligible amount of attenuation due to dispersion from the NAPL source to the aquifer outlet. For the E25 and the E50 cases, the highest hydrocarbon concentrations were detected at the bottom row of the sampling ports (3, 6, 9, 12, and 15) which were at the same elevation as the fuel injection port. However, for E85 the highest concentrations were observed at higher pts. (locations 2, 5, 8, 11, 14). This is consistent with the final NAPL source distribution for E85 which extends further vertically than the NAPL sources for E25 and E50. Also for E85, hydrocarbon concentrations were higher at other locations compared to the E25 and E50 spill cases which suggested a wider-spread NAPL impacted area for E85. Results for the individual compounds were as follows:

Benzene: Source depletion of benzene increased with ethanol fuel content. Benzene was completely depleted within 2 weeks following a spill of E85. Benzene did not deplete for E25 over the 4-week period.

Toluene: Depletion of toluene occurred for E50 but more slowly than toluene for E85. Toluene was completely depleted after 3 weeks for E85. No depletion of toluene occurred for E25 over the 4-week period.

m-Xylene: No depletion for E25 and E50 over 4 weeks. Some depletion was observed for E85. Interestingly, E50 yielded the highest longer-term m-xylene concentrations of all fuel the blends (E25, E50, E85).

Tri-methyl benzene (TMB): No depletion occurred over the 4-week period for all ethanol fuel blends. TMB is an interesting compound to track. Because it depletes slowly, it can be used as an indication of source strength (i.e., contact of NAPL with groundwater). Maximum TMB concentrations were lower for E25 (2.2 mg/L) than for E50 and E85 (3.3 and 3.4 mg/L). This may reflect some flow bypassing of NAPL by groundwater for the E25 case. This is consistent with the higher NAPL saturations for E25 and the post-tracer experiments which indicate flow bypassing occurs for E25. Interestingly, E85 yielded the highest longer-term TMB concentrations of all the fuel blends (E25, E50, E85).

Table 4.1 Maximum dissolved hydrocarbon concentrations from longer-term dissolution experiments following spills of E25, E50, and E85 fuel blends.

Fuel Blend	Benzene mg/L	Toluene mg/L	m-Xylene mg/L	TMB mg/L
E25	1.4	1.4	1.6	2.2
E50	0.8	2.1	2.4	3.3
E85	0	0.2	2.5	3.4

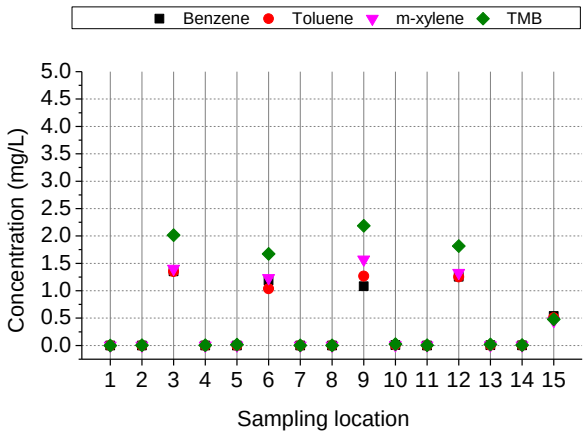

(a) 2 weeks after spill

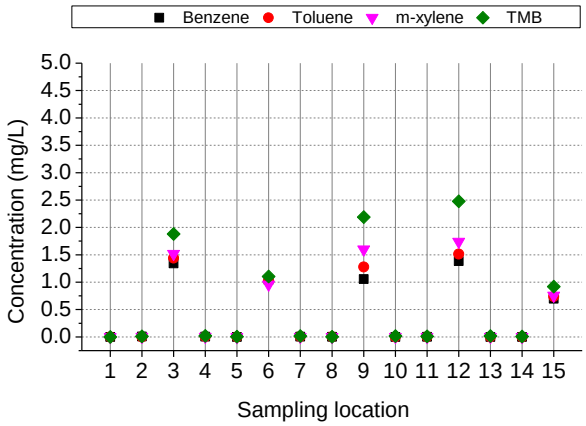

(b) 3 weeks after spill

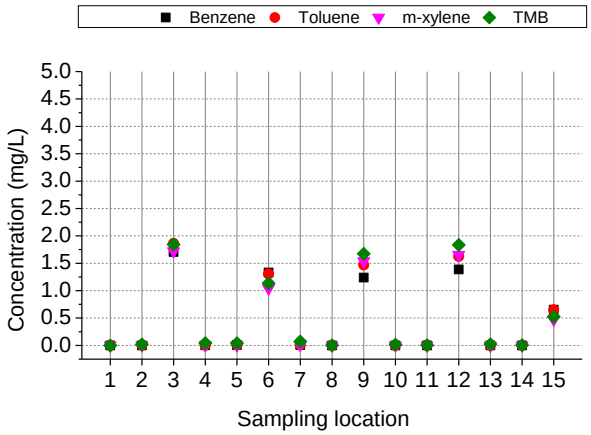

(c) 4 weeks after spill

Figure 4.5 Pore water hydrocarbon concentrations measured at 2, 3, 4 weeks after the spill of an E25 ethanol fuel blend.

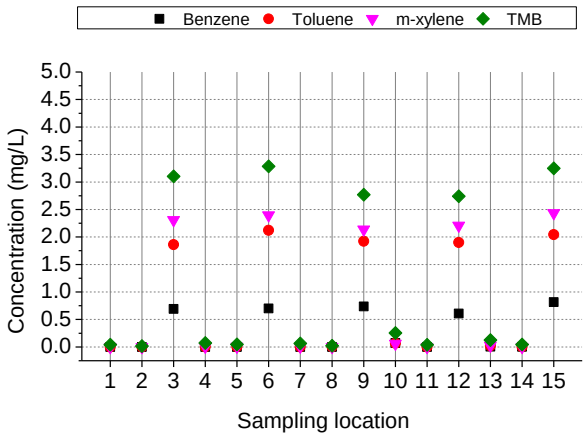

(a) 2 weeks after spill

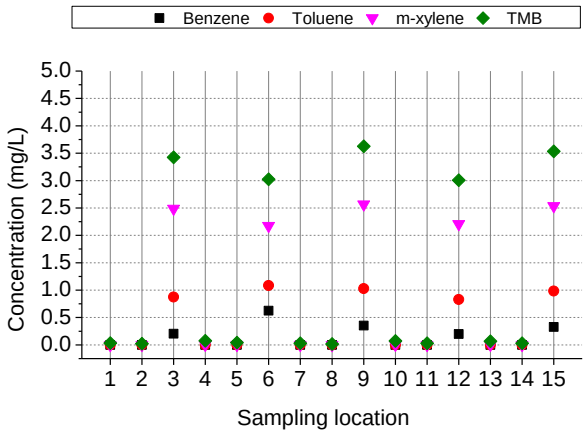

(b) 3 weeks after spill

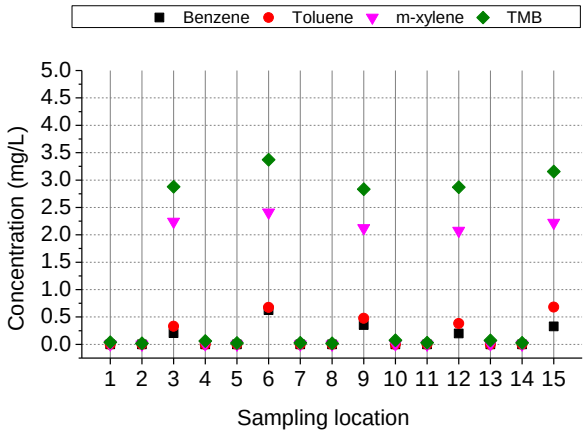

(c) 4 weeks after spill

Figure 4.6 Pore water hydrocarbon concentrations measured at 2, 3, 4 weeks after the spill of an E50 ethanol fuel blend.

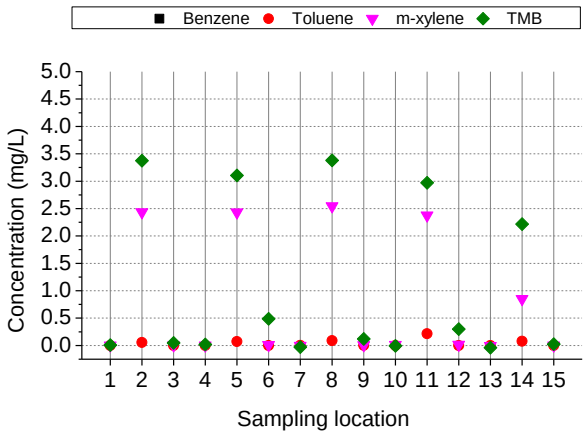

(a) 2 weeks after spill

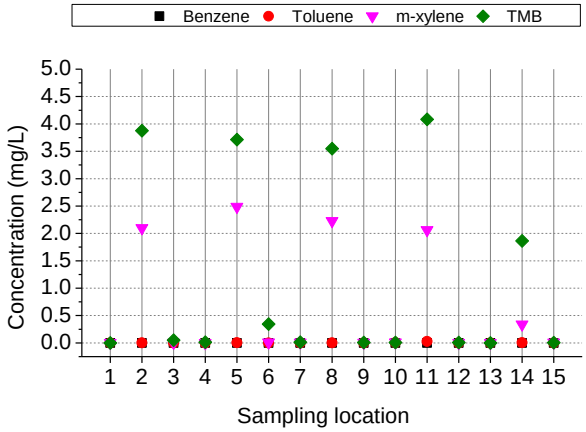

(b) 3 weeks after spill

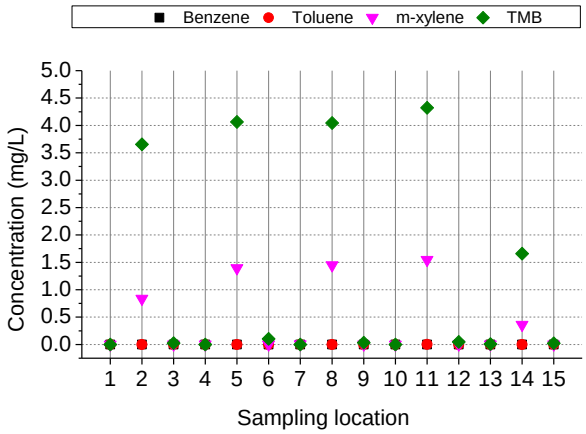

(c) 4 weeks after spill

Figure 4.7 Pore water hydrocarbon concentrations measured at 2, 3, 4 weeks after the spill of an E85 ethanol fuel blend.

4.3.3 Analysis with a NAPL Dissolution Model

An equilibrium dissolution model was used to analyze the pore water data in 4.3.2 to determine the extent to which equilibrium dissolution occurred for the NAPL sources formed for the various fuel blends.

For 1-D advection and dispersion in a source zone containing a multi-component, residually trapped NAPL of constant saturation, a component differential mass balance yields the following PDE

$$\frac{\partial C_i^w}{\partial t} + \frac{S_o}{S_w}\frac{\partial C_i^o}{\partial t} = D\frac{\partial^2 C_i^w}{\partial x^2} - v\frac{\partial C_i^w}{\partial x}, \qquad \text{4-1}$$

where

C_i^w = the concentration of hydrocarbon component "i" in the aqueous phase (mg/L),

C_i^o = concentration of the hydrocarbon "i" in the NAPL phase (mg/L),

S_o = NAPL phase saturation,

S_w = water phase saturation,

x = downstream location (cm),

v = interstitial velocity (cm/day),

D = dispersion coefficient (cm^2/day).

Assuming a linear partition coefficient, K_i^{o-w}, for the hydrocarbon component "i" between the NAPL phase and the aqueous phase, then

$$C_i^o = K_i^{o-w} C_i^w . \qquad \text{4-2}$$

Using the retardation coefficient written as

$$R_i = 1 + \frac{S_o}{S_w} K_i^{o-w} , \qquad 4\text{-}3$$

Equation 4-1 becomes

$$R_i \frac{\partial C_i^w}{\partial t} = D \frac{\partial^2 C_i^w}{\partial x^2} - v \frac{\partial C_i^w}{\partial x} . \qquad 4\text{-}4$$

Using the following initial and boundary conditions:

$t = 0$, $C_i^w = C_{i0}^w$;

$t > 0$, $x = 0$, $C_i^w = 0$;

$t > 0$, $x \approx \infty$, $\frac{\partial C_i^w}{\partial x} = 0$;

the analytical solution (Lapidus et al., 1952; Rixey et al., 1999) is:

$$\frac{C_i^w}{C_{i0}^w} = 1 - \frac{1}{2} erfc\left[\frac{L - vt / R_i}{2\sqrt{Dt / R_i}}\right] - \frac{1}{2}\exp(\frac{vL}{D}) erfc\left[\frac{L + vt / R_i}{2\sqrt{Dt / R_i}}\right], \qquad 4\text{-}5$$

where

C_{i0}^w = initial dissolved hydrocarbon component i concentration at the edge of the NAPL source (mg/L)

L = length of the NAPL source zone (cm).

Using the non-dimensionalized variables

$$C_i^{w*} = \frac{C_i^w}{C_{i0}^w}, \; x^* = \frac{x}{L}, \; t^* = \frac{vt}{LR_i}, \qquad 4\text{-}6$$

and Peclet number,

$$Pe = \frac{vL}{D}, \qquad 4\text{-}7$$

Equation 4-5 can be written as

$$C_i^{w*} = 1 - \frac{1}{2} erfc\left[\sqrt{\frac{Pe}{4t^*}}(1-t^*)\right] - \frac{1}{2}\exp(Pe) erfc\left[\sqrt{\frac{Pe}{4t^*}}(1+t^*)\right]. \qquad 4\text{-}8$$

Equation 4-8 was used to analyze the dissolution data for benzene, toluene, m-xylene, and TMB. Values of several of the parameters that were used for Equation 4-8 are shown in Table 4.2.

The lengths of the NAPL source, L, were determined from the visualization experiments. They were the lengths of the NAPL impacted zone at the same elevations as the sampling locations where the maximum dissolved hydrocarbon concentrations were measured. The interstitial velocity observed from the tracer study, v = 50 cm/day was used. The NAPL saturations were based on best fits of the data for all three compounds using Equation 4-8. The inferred saturation values are lower than the average

saturation values for the entire NAPL impacted areas presented in Table 3.3, but are consistent with the more localized visualization data for the NAPL regions where groundwater flow occurred. A Peclet number of 10 was used based on best overall fits of Equation 4-8 to the dissolution curves.

Hydrocarbon concentration values, C_i^w, used in Equation 4-8 were based on the average concentrations for a given sampling time (2, 3, or 4 weeks) for all sampling locations at the same elevation of the NAPL source. The initial concentrations, C_{i0}^w, for all compounds for E25 were determined from the 2-week sampling concentrations, since little depletion of hydrocarbons occurred for this case due to the high NAPL saturation. In addition, TMB concentrations did not deplete for all fuel blends, including E85, so initial values were known for all fuel blends. The initial concentrations for BTX for E50 and E85 were determined by prorating the measured BTX concentrations for E25 by the ratios of initial TMB concentrations for E50 and E85, respectively, relative to that for E25. Note that the initial values for BTX for E25 in Table 4.2 are lower than would be expected based on the initial value for TMB and considering the differences in the equilibrium partition coefficients between NAPL and pore water for BTX and TMB. For comparison initial values for BTX were estimated based on the ratio of equilibrium pore water concentrations for B, T, or X relative to that for TMB, multiplied by the measured initial value for TMB. The following calculated vs. measured values were obtained: benzene: 6.64 vs.1.22 mg/L; toluene: 4.01 vs. 1.23 mg/L; m-xylene: 2.20 vs. 1.38 mg/L, TMB: 1.82 vs. 1.82 mg/L. This is likely due to two factors: (1) non-equilibrium dissolution and (2) a change in the final NAPL composition due to cosolvency by ethanol. The decreasing ratio of equilibrium/measured values with decreasing hydrocarbon

solubility (from benzene to TMB) indicates that changes in NAPL composition occurred. The effects of non-equilibrium dissolution for E25 are reflected in the differences in equilibrium and measured values for TMB.

Values of R_i, were determined from the NAPL-water partition coefficients, K_i^{o-w}, for the various hydrocarbons. K_i^{o-w} was calculated from (Garg et al., 1999).

$$K_i^{o-w} = \frac{C_i^o}{C_i^w} = \frac{\gamma_i^w}{\gamma_i^o} \frac{\rho^o}{\rho^w} \frac{MW_{Avg}^w}{MW_{Avg}^o}, \qquad 4\text{-}9$$

where

γ_i^w = activity coefficient of hydrocarbon component "i" in the aqueous phase,

γ_i^o = activity coefficient of hydrocarbon component "i" in the NAPL phase,

MW_{Avg}^w = average molecular weight of the aqueous phase, and

MW_{Avg}^o = average molecular weight of the NAPL phase.

The calculated NAPL-water partition coefficients were given in Table 3-1. Activity coefficients for each hydrocarbon component were obtained from measured values for NAPLs of similar composition (Rixey et al., 2000). Best fits of the measured pore water concentration data with Equation 4-8 are shown in Figure 4.8.

Table 4.2 Source length, seepage velocity, NAPL saturation, and initial pore water concentration for hydrocarbon components after depletion of ethanol.

	E25	**E50**	**E85**
L, cm	9.0	13.3	10.9
v, cm/day	50	50	50
S_o, cm^3/cm^3	0.39	0.06	0.03
Pe, dimensionless	10	10	10
C^w_{TMB0}, mg/L	1.82	3.13	3.68
$C^w_{benzene0}$, mg/L	1.22	2.09	-
$C^w_{toluene0}$, mg/L	1.23	2.11	2.48
$C^w_{m-xylene0}$, mg/L	1.38	2.38	2.80

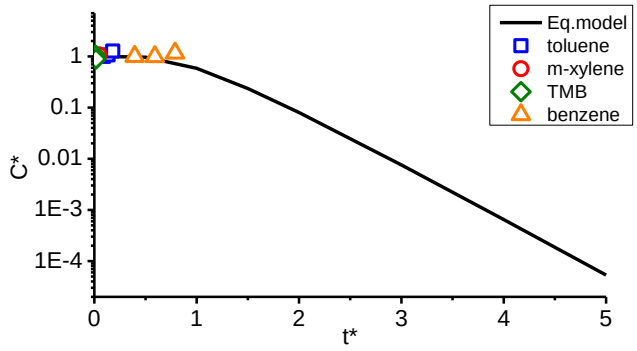

(a) E25

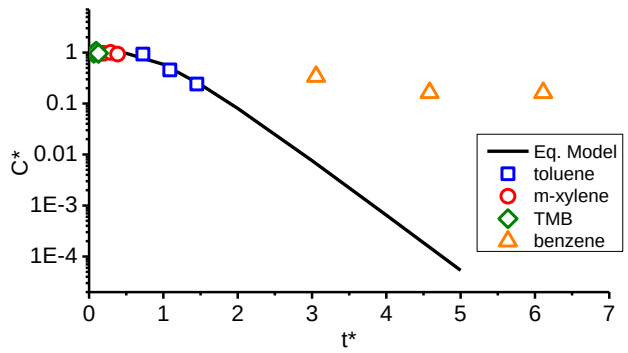

(b) E50

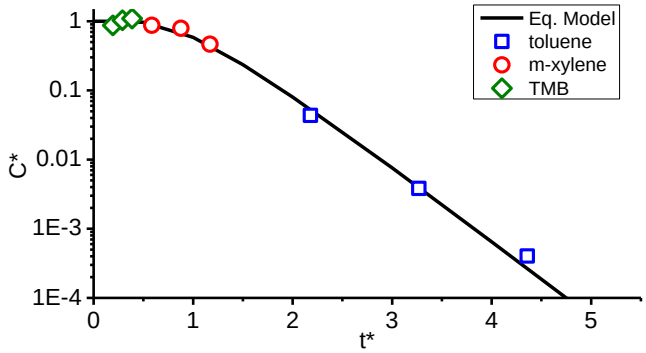

(c) E85

Figure 4.8 Comparison of experimental pore water measurements with an equilibrium dissolution model (Equation 4-8) for longer-term dissolution from NAPL sources for various fuel blends.

As shown in Figure 4.8c, the concentration measurements for all of the hydrocarbon components for the E85 spill case compared well with the equilibrium dissolution model. This indicates that dissolution for the hydrocarbon components from the residual NAPL phase followed equilibrium dissolution for the entire amount of NAPL in the source region. This was expected due to the low NAPL saturation throughout the source region which resulted in good contact between the NAPL and the groundwater passing through the NAPL source, and is consistent with the post-spill tracer results.

For E50, the pore water data for benzene departed significantly from the equilibrium dissolution model. This is an indication that benzene depletion from the NAPL source was mass-transfer limited. Recall that the tracer experiment for E50 indicated that there were two regions in the source: one region of lower NAPL saturation where groundwater flow readily passed through the NAPL, and a second region of higher NAPL saturation where groundwater flow was hindered. It is likely that benzene present in the first region with low NAPL saturation occurred under equilibrium dissolution conditions and was depleted by the time the first measurement was made (at 2 weeks), so that the benzene concentrations that were observed were due to mass-transfer limited dissolution from the bypassed NAPL. Equilibrium dissolution for the first region is consistent with the pore water measurements for toluene for which equilibrium dissolution was observed for the three sample times (Figure 4.8 b). Since toluene has a larger partition coefficient, it would deplete from the first region more slowly than benzene. So for a given time, benzene dissolution from NAPL could be mass-transfer limited while toluene dissolution could be equilibrium controlled. Overall, these dissolution results indicate that the hydrocarbons were partially available for equilibrium

dissolution from the NAPL formed for the E50 case, with a remaining fraction that was mass-transfer limited.

For E25, pore water concentrations remained constant for all hydrocarbons, even for benzene. This was due to the high NAPL saturation at the source. Figure 4.8a shows that for this level of saturation, little depletion for benzene would have been expected over the duration of the experiment (4 weeks) even under equilibrium dissolution conditions. Of course an equilibrium dissolution model is really not appropriate for E25, even for the first sampling time. Recall that the measured pore water concentrations at the first sampling time (2 weeks) were lower for E25 than for E50 and E85, when one compares measurements for solutes that did not deplete (m-xylene and TMB) for all three fuel blends (Table 4.2). For E25, these results indicate that dissolution of hydrocarbons from essentially the entire amount of NAPL present in the source was mass transfer limited.

CHAPTER 5 NUMERICAL SIMULATION

5.1 Introduction

Physical-chemical interactions between different phases, fluid properties, and media characteristics are important factors that determine the fluid transport behavior in porous media. A comprehensive numerical model was used to evaluate their importance on the solute transport and NAPL phase distributions from releases of alcohol blended fuels. The key fluid/media properties modeled include: fluid density, viscosity, IFT, phase equilibria, porosity, relative permeability, saturation, and capillary pressure.

The simulation tool used in this study was UTCHEM. It is a 3-D, multicomponent, multiphase, finite difference numerical model. It was originally developed for modeling enhanced oil recovery processes (Pope et al., 1978) and was subsequently modified to simulate the enhanced remediation of aquifers. The most unique feature of the tool for our investigations is that it accounts for complex phase behavior, therefore multi-phase flow and transport with compositional dependent fluid phase properties can be modeled to analyze the behavior of spills of alcohol blended fuels. The main focus of the numerical simulations was to model the impact of alcohol on physical chemical properties that are critical to source generation and transport behavior of alcohol and hydrocarbons.

After defining parameters in the model based on physical properties obtained from the literature for a specific ethanol-gasoline-water system, multiphase flow simulations were conducted to model the transport behavior of hydrocarbons and ethanol in both the NAPL and aqueous phases for spills of ethanol blended fuels in the saturated zone. Fixed volume spills of ethanol blended fuel mixtures with varying ethanol content

were investigated. The results of the simulations were compared with the results from the corresponding 2-D physical model experiments that were presented in Chapter 4. Simulations were then conducted to extend the results to other spill scenarios and aquifer conditions (Chapter 6).

5.2 Model Formulations

5.2.1 Conservation Equation

For compositional modeling, a mass balance was developed and solved for the concentration of the chemical components. In UTCHEM, up to 19 components can be specified and their concentrations can be calculated for each phase, and the total concentration of one component is the summation of all phase concentrations for that component. The following four phases can be modeled: an aqueous phase, an oleic phase, a gas phase and a microemulsion phase. The mass conservation equation for component κ can be written as

$$\frac{\partial}{\partial t}(\phi \tilde{C}_{\kappa} \rho_{\kappa}) + \vec{\nabla} \cdot \left[\sum_{l=1}^{n_p} \rho_{\kappa} (C_{\kappa l} \vec{u}_l - \vec{\tilde{D}}_{\kappa l}) \right] = R_{\kappa} , \qquad 5\text{-}1$$

where

ϕ = porosity (cm^3 PV/cm^3),

$\tilde{C}_{\kappa}$ = total volume concentration of the component κ in the mobile and stationary phases (cm^3/cm^3 PV),

$C_{\kappa l}$ = concentration of κ in phase l (cm^3/cm^3),

ρ_{κ} = density of the pure component κ (g/cm^3),

$\vec{u}_l$ = Darcy flux (cm/day), and

R_κ = source (+) or sink (-) term (g/cm^3·day).

$\vec{\tilde{D}}_{\kappa l}$ is the dispersive flux which is assumed to follow the Fickian form,

$$\vec{\tilde{D}}_{\kappa l} = nS_l \overline{\overline{K}}_{\kappa l} \cdot \vec{\nabla} C_{\kappa l}\,, \qquad 5\text{-}2$$

where

S_l = the saturation of phase l (cm^3/cm^3 PV),

$\overline{\overline{K}}_{\kappa l}$ = the dispersivity tensor (cm^2/day), defined by Bear (1979) which includes the effect of both molecular diffusivity, longitudinal dispersivity and transverse dispersivity.

The pressure equation is developed by summing the mass balance equations for all the components to calculate the phase fluxes, and by using Darcy's law and the definition of capillary pressure (capillary pressure is the pressure difference across the interface of the two immiscible phases) (UTCHEM Tech Documentation, 2000). The numerical solution uses the implicit pressure-explicit saturation (IMPES) method established by Aziz et al. (1979).

In this study, a water-saturated aquifer without entrapped air was assumed. Water and oleic phases were modeled for up to four components: ethanol, a gasoline hydrocarbon mixture (modeled as a single component), water, and, for some cases, a conservative tracer. The microemulsion phase in UTCHEM was used to describe the ethanol concentrations in the pore water. Although UTCHEM is able to handle the effects of pressure and temperature on fluid properties, in this study fluids were assumed to be

incompressible and the system was isothermal. A detailed description of UTCHEM can be found in the Technical Documentation of UTCHEM (2000). Key components of UTCHEM important to this study are described below.

5.2.2 Phase Equilbria

For a hydrocarbon-water mixture, when the concentration of hydrocarbon in the solution exceeds the solubility, two phases will be formed. Ethanol is completely miscible with water due to its hydroxyl group and short carbon chain, and it is very soluble in most non-polar hydrocarbons. If ethanol is added to a two-phase system, it will partition into both the aqueous phase and the hydrocarbon phase, and the amount of the hydrocarbon that dissolves in the aqueous phase can be enhanced due to the cosolvency effect. Ternary diagrams are commonly used to describe this phase equilibria as described in Chapter 1. In miscible displacement, the phase behavior relations of a reservoir fluid are commonly described by using a pseudo-ternary diagram in which the hydrocarbons are grouped into three pseudo-components based on their volatilities (Stalkup, 1983). For an ethanol-gasoline-water system, the light hydrocarbons in the gasoline are usually grouped as a pseudo-component and the cosolvent (alcohol) and water remain as the other two pure components in the ternary diagram.

Figure 5.1 is a pseudo-ternary diagram for a gasoline-water-ethanol system developed by Oliviera (1997). It is a typical type 1 (type II (-)) with negative slope tie lines. The curve that separates the one-phase region and the two-phase region is called the binodal curve. In UTCHEM, Hand's rule (Hand, 1929) is used to model the bimodal curve in which the compositions of ethanol, water, and gasoline are determined from the empirical equation

$$\frac{C_l^e}{C_l^o} = A\left(\frac{C_l^e}{C_l^w}\right)^B, \qquad 5\text{-}3$$

where C_l^e, C_l^o, and C_l^w are the concentrations of ethanol, gasoline oil, and water in the fluid phase "l", respectively. Both A and B are fitting parameters. UTCHEM assumes a value of $B = -1$ which produces a symmetric binodal curve. Parameter A is determined by the height of the binodal curve and is defined as

$$A = \left(\frac{2C_{e,\max}}{1 - C_{e,\max}}\right)^2, \qquad 5\text{-}4$$

where $C_{e,\max}$ is the maximum concentration of ethanol in a phase separated mixture above which only one phase can be formed. For the tie-line calculations, for given concentrations of ethanol and NAPL in the NAPL phase side of the binodal curve (C_o^e and C_o^o), the corresponding concentrations of ethanol and NAPL in the aqueous phase (C_w^e and C_w^w) can be calculated as

$$\frac{C_o^e}{C_o^o} = E\left(\frac{C_w^e}{C_w^w}\right), \qquad 5\text{-}5$$

where parameter E is determined by the concentrations at the plait point. Since the plait point should be on both the binodal curve and the tie line, parameter E can be determined from

$$E = \frac{1 - C_{o,pl} - \frac{1}{2}\left[-AC_{o,pl} + \sqrt{\left(AC_{o,pl}\right)^2 + 4AC_{o,pl}(1 - C_{o,pl})}\right]}{C_{o,pl}}, \qquad 5\text{-}6$$

where $C_{o,pl}$ is the hydrocarbon concentration at the plait point. Equation 5-6 follows from Equations 5-3, 5-4, and 5-5.

The comparison between the calculated binodal curve and tie lines from the experimental data measured by Oliviera (1997) for an ethanol-gasoline-water system is shown in Figure 5.1. The negative slopes of the tie lines indicate that ethanol partitions preferentially to the aqueous phase. Thus, strong partitioning of ethanol from a fuel mixture into the available pore water would be expected.

One of the major simplifications in the model formulation is the symmetry of the binodal curve. For the ethanol-gasoline-water system, the binodal curve is fairly symmetric. Since our primary focus is to predict accurate concentrations of dissolved hydrocarbons in pore water in the presence of ethanol, the aqueous phase portion of the binodal curve was the most important. As shown in Figure 5.1, the model provided a good fit to the experimental data for the aqueous phase.

The phase equilibria model is a key element of the simulator and determines the accuracy of the simulation results. Additional composition dependent physical properties such as IFT, viscosity, and density are determined from the phase equilibrium model.

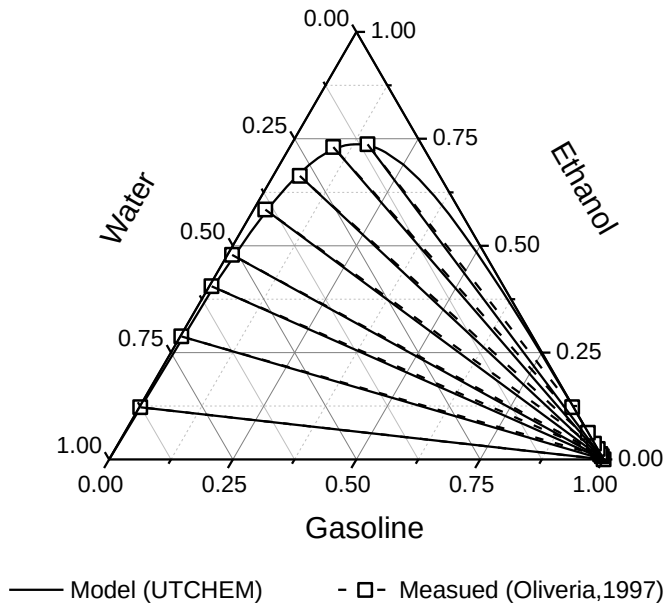

Figure 5.1 Binodal curve and tie lines for a typical ethanol-gasoline-water system.

5.2.3 Viscosity

Viscosity of the fluid has a direct impact on fluid phase flow and solute transport in porous media. Compositional changes of the plume will result in changes of the fluid viscosity. For our numerical simulations, composition dependent viscosities for ethanol-water mixtures were used to predict the transport behavior of the aqueous plume generated from spills of ethanol blended fuels.

For an ideal binary mixture, viscosity changes linearly with the solute's concentration. However, for real solutions, the viscosities of the mixtures often exhibit a maximum or a minimum and sometimes both (Poling et al., 2000). The theory for estimating the viscosity of the liquid mixtures is not well established. Thus, an empirical approach using pure component viscosities was used to model the liquid mixture viscosity. In UTCHEM, fluid viscosity is calculated using such a model. Pure

component viscosities and their phase concentrations are used to estimate the viscosity of the fluid mixture. The viscosity of the ethanol aqueous solution, μ'_w, is calculated using

$$\mu'_w = C_w^w \mu_w e^{\alpha 1(C_w^o + C_w^e)} + C_w^o \mu_o e^{\alpha 2(C_w^w + C_w^e)} + C_w^e \alpha_3 e^{(\alpha 4 C_w^w + \alpha 5 C_w^o)}, \quad 5\text{-}7$$

where μ_w, μ_0 are viscosities of water and gasoline, respectively, and $\alpha 1$, $\alpha 2$, $\alpha 3$, $\alpha 4$, $\alpha 5$ are fitting parameters. The parameter $\alpha 3$ represents the impact of the cosolvent on the viscosity of the aqueous mixture. For this study $\alpha 3$ is the viscosity of pure ethanol. The other four parameters are fitting parameters used to incorporate the impact of dissolved hydrocarbons and cosolvent on the viscosity of the aqueous solution. Lee (2008b) reported aqueous viscosity measurements for ethanol-gasoline water mixtures. The data were generated by adding water to E85 fuel until phase separation occurred. Figure 5.2a shows that hydrocarbons had a minor effect on the viscosity of the aqueous phase even up to 15% (v/v) gasoline in the solution. For the spill experiments conducted for this dissertation, the dissolved hydrocarbon content in the aqueous phase was low. Thus, it was considered reasonable to ignore the impact of dissolved hydrocarbons on the viscosity of the aqueous plume. Then only two parameters, α1 and α4, are needed to fit aqueous mixture viscosity data with Equation 5-7. Figure 5.2b shows that Equation 5-7 provides a good representation of aqueous solution viscosities for the ethanol-water mixture over the entire concentration range. Note in Figure 5.2 that the maximum mixture viscosity is more than twice the pure component viscosities, so changes in ethanol concentrations in pore water following a release can have a significant impact on pore water viscosity.

The viscosity of the gasoline phase was assumed to be the molar average viscosity of the hydrocarbons in the gasoline mixture. Lee et al. (2012) showed that water and alcohol dissolved in the hydrocarbon phase had little impact on the non-aqueous phase viscosity.

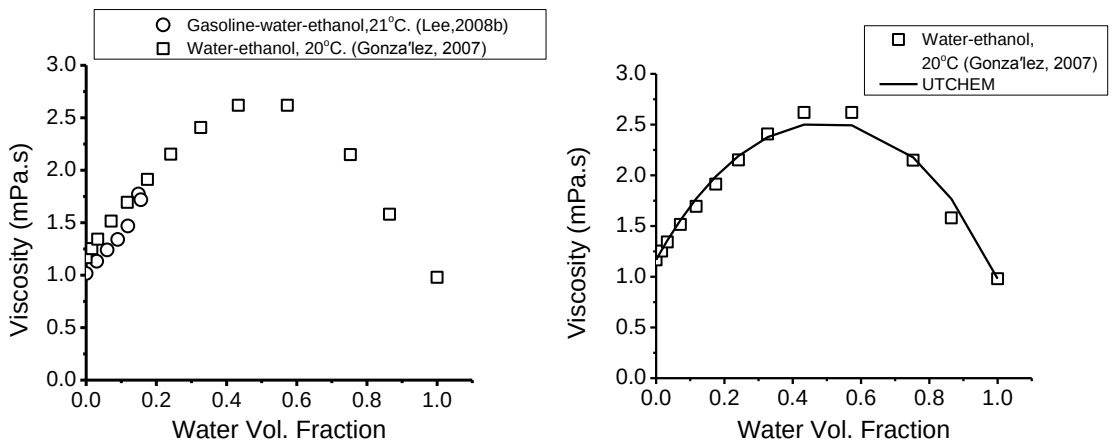

(a) (b)

Figure 5.2 (a) Comparison between the viscosities of ethanol-hydrocarbon-water aqueous mixtures and hydrocarbon-free ethanol-water mixtures; (b) Comparison of Equation 5-7 and experimental measurements for ethanol-water mixtures.

5.2.4 Interfacial Tension

Capillary forces are the result of the combined effect of the IFTs between different phases, pore size and geometry, and the wetting characteristics of the media. When ethanol is present in a water hydrocarbon mixture, the solubility of the hydrocarbon is enhanced in the aqueous phase and more water can be dissolved in the NAPL phase due to the cosolvency effect. Compositional changes in the aqueous phase and the non-aqueous phase due to flow and mass transport alter the IFT between the phases which directly affects the capillary pressure that holds the non-wetting oil phase in the pores against viscous and gravity forces. Based on the UTCHEM formulations, in

additional to the capillary pressure, relative permeability and residual saturation are also functions of the IFT.

In UTCHEM, two models are available to calculate the changes in IFT due to a third component partitioning between the two phases. They are Healy and Reed's model (1974) with Hirasaki's modification (1981) and Chun-Hun's model which was also modified with Hirasaki's correction factor that reduces the water-oil IFT to the correct value when the ethanol concentration approaches zero. Both methods were tested and compared with laboratory measured IFT data (Oliviera, 1997). Both models yielded similar predictions of IFT for the ethanol-water-gasoline system, Chun-Huh's model was selected due to its simplicity compared to the Healy and Reed model.

In Huh's model it is assumed that the IFT between the oleic phase and the aqueous phase is related to the solubility ratio. The solubility ratio, R_{ow}, is defined as

$$R_{ow} = \frac{C_w^o}{C_w^e} \equiv \frac{V_o}{V_e}, \qquad 5\text{-}8$$

where the hydrocarbon and ethanol concentrations in the aqueous phase are expressed in volume fractions. The IFT between the aqueous phase and the NAPL phase can be calculated using

$$\sigma_{ow} = \sigma_{ow}^0 \exp(-aR_{ow}) + \frac{cF_o}{R_{ow}^2}(1 - \exp(-aR_{ow}^3)), \qquad 5\text{-}9$$

where σ_{ow}^{0} is the IFT between the oil phase and the aqueous phase without ethanol present. In Equation 5-9, a and c are both curve fitting parameters. F_o is a composition dependent factor that reduce σ_{ow} to σ_{ow}^{0} as the ethanol concentration approaches zero, and is defined as

$$F_o = \frac{1-\exp(-\sqrt{(C_o^w - C_w^w)^2 + (C_o^o - C_w^o)^2 + (C_o^e - C_w^e)^2})}{1-\exp(-\sqrt{2})} . \qquad 5\text{-}10$$

A comparison between the model results and experimental data is shown in Figure 5.3.

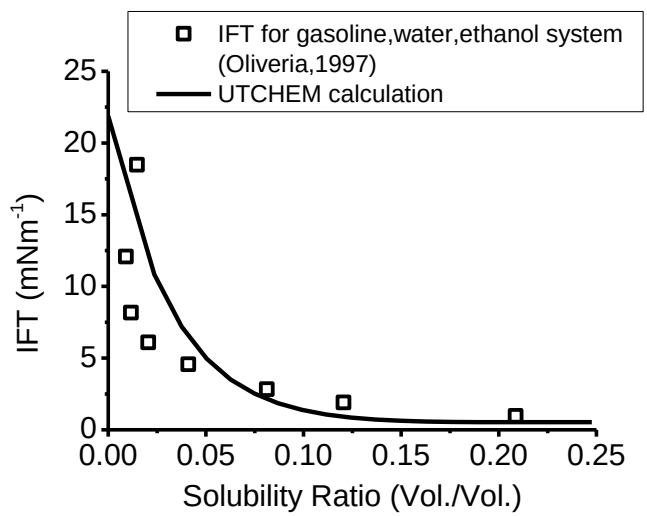

Figure 5.3 Comparison between IFT values using Equation 5-9 and experimental measurements.

5.2.5 Relative Permeability & Capillary Pressure

When evaluating fluid transport in porous media when multiple fluid phases are present, it is necessary to specify the permeability in terms of relative permeabilities for each phase. The relative permeabilities for an oil-water system are defined as

$$k_{ro} = \frac{k_o}{k} \qquad 5\text{-}11$$

and

$$k_{rw} = \frac{k_w}{k}, \qquad 5\text{-}12$$

where k_{ro}, k_{rw} are the relative permeabilities for the oil and water phases, respectively, k_o and k_w are the permeabilities for each phase, and k is the intrinsic permeability.

Relative permeability is a function of the saturation of the corresponding fluid phase. The Brooks and Corey method is used in UTCHEM to estimate relative permeabilites for different phases at different saturations. For oil/water two-phase flow, the relative permeabilites can be expressed in terms of the normalized water saturation as

$$k_{rw} = k_{rw}^0 (S^*)^{n_w} \qquad 5\text{-}13$$

and

$$k_{ro} = k_{ro}^0 (1 - S^*)^{n_o}, \qquad 5\text{-}14$$

where k_{rw}^0, k_{ro}^0 are the relative permeability endpoints, and n^w, n^o are the exponents for the water and oil phases, respectively. The normalized water saturation S^* is defined

depending on the media saturation history. For a NAPL spill into a water-saturated aquifer, assuming NAPL is the non-wetting phase, the displacement occurs by drainage and S^* is defined as

$$S^* = \frac{S_w - S_{wr}}{1 - S_{wr}}. \qquad 5\text{-}15$$

When the media is saturated with the non-wetting phase NAPL and is displaced by the wetting phase, imbibition occurs and S^* is defined as

$$S^* = \frac{S_w - S_{wr}}{1 - S_{wr} - S_{or}}, \qquad 5\text{-}16$$

where S_w is the aqueous phase saturation, and S_{wr} and S_{or} are the residual saturations of water and oil, respectively.

Parameters k_{rw}^0 , k_{ro}^0 , n_w , and n_0 are usually estimated by the least-squares method of fitting experimental relative permeability and capillary pressure data. Since laboratory permeability data were not available for the specific system used in the 2-D experiments, some relative permeability and capillary pressure parameters were estimated based on available literature data for similar systems. The relative permeability exponents determine the shape of the relative permeability-saturation curves. Values of "4" and "2" were used for the wetting and non-wetting phases, respectively, as suggested by Corey (1954). The end point relative permeability parameters k_{ro}^0 and k_{rw}^0 were

initially based on values from Brown et al. (1994), where “1” and “0.65” were used as the relative permeability of the NAPL and water phases at their residual saturations, respectively, for drainage. However, due to the high residual NAPL saturation formed for the low ethanol content spill cases, a significant reduction in the groundwater velocity through the NAPL region and by-passing of groundwater flow around the NAPL region was observed in the physical model experiments. In order to calibrate the model with the experimental observation, the end point relative permeabilities were adjusted to reduce the water velocity passing through the residual NAPL source.

The relative permeability is also a function of the IFT. When IFT decreases, both water and oil residual saturations are reduced due to the reduction in capillary forces. The reduction of IFT results in an increase in both k_{ro}^{0} and k_{rw}^{0} due to reduced residual saturations. Wetting phase residual saturations have a limited impact on the non-wetting phase permeability because the wetting phase occupies the smaller pores. By contrast, non-wetting phase residual saturations significantly impact the relative permeability of the wetting phase. For low IFT conditions (resulting in a high trapping number; trapping number is introduced in section 5.2.6), it was assumed both non-wetting phase permeability and wetting phase permeability are equal to the intrinsic permeability when the other phase saturation approaches zero. The relative permeability curve exponents were assumed to be constant regardless of the changes in IFT. Parameters that were used for the relative permeability curves are summarized in Table 5.1.

Table 5.1 Parameters used for relative permeability curves.

	High trapping number	**Low trapping number**
S_{wr}	0	0.1
S_{or}	0	0.3
k	12000 mD	12000 mD
k_{rw}^{0}	1	0.01
k_{ro}^{0}	1	0.6
n_w	4	4
n_o	2	2

For capillary pressure modeling, UTCHEM uses a modified Brooks-Corey function. As previously mentioned, a hydrocarbon spill in the water-saturated zone was taken to be in the drainage direction. The relationship between the capillary pressure, P_c, and the normalized water saturation for drainage is

$$\left(P_b / P_c\right)^{\lambda_d} = S^* . \qquad 5\text{-}17$$

During imbibition the capillary pressure equation is

$$\left(P_b / P_c\right)^{\lambda_i} = (1 - S^*) , \qquad 5\text{-}18$$

where the normalized water saturation, S^*, is defined by Equation 5-15 and Equation 5-16 for drainage and imbibition processes, respectively; and P_b is the entry pressure which is dependent on soil permeability and porosity. Because the entry pressure is a function of the characteristics of the media as well as the IFT between the phases, it was calculated using equations $\sigma c_i(\phi / k)^{1/2}$ and $\sigma c_d(\phi / k)^{1/2}$ with c_i and c_d as fitting parameters for the imbibition and drainage curves, respectively. Here σ is the IFT between the aqueous and oil phases normalized by the IFT between the two fluid phases without ethanol present. This scaling is based on the work by Leverett (1941) that describes capillary pressure for similar beds with different permeability, porosity, and wetting properties. The parameters c_i, c_d, λ^i, and λ^d were selected from capillary pressure measurements (Kueper, 1989) for drainage in an unconsolidated media. Based on the 2-D physical model experiment results, highly saturated hydrocarbon source regions were formed for low ethanol content fuel spills, and the local displacement direction in those regions would follow the imbibition direction. However, again, possibly due to a significant bypassing of the groundwater, the hydrocarbon phase in those NAPL saturated regions was not able to be displaced by the groundwater, thus the fitting parameters for drainage displacement were used throughout the experiment.

Table 5.2 Capillary pressure parameters.

Imbibition		**Drainage**	
c_i, psi (darcies)$^{1/2}$	0.44	c_d, psi (darcies)$^{1/2}$	0.21
λ^i	-0.5	λ^d	1.92

5.2.6 Residual Saturation and Capillary Desaturation

Quantifying the residual NAPL content in a source of contamination is important for assessing the impact of spills on groundwater quality and for the design and analysis of remediation processes. It is common to assume constant residual NAPL saturation will be formed after a fuel spill occurs, that is: when NAPL in the pores is displaced by water, some residual NAPL remains in the pores that cannot be further displaced by groundwater. However, when a cosolvent or surfactant like ethanol is added to the system, the residual saturation can be significantly reduced. Therefore, spills of high ethanol content fuel blends may produce NAPL sources of lower residual NAPL saturation compared to spills of fuels with low ethanol content.

For trapped residual oil to be mobilized, viscous and/or buoyancy forces must exceed the capillary force within the pores. The capillary number and bond number are commonly used to quantify viscous and buoyancy effects, respectively. The capillary number and Bond number are defined as

$$N_c = \frac{|\mu \cdot u|}{\sigma_{ll'}} \qquad \text{5-19}$$

and

$$N_B = \frac{kg(\rho_l - \rho_{l'})}{\sigma_{ll'}}, \qquad \text{5-20}$$

respectively, where $\sigma_{ll'}$ is the IFT between the phases, ρ_l and $\rho_{l'}$ are the densities of the contacting liquids, μ and u are the viscosity and velocity of the displacing fluid, respectively, k is the intrinsic permeability, and g is the acceleration due to gravity.

In UTCHEM the trapping number concept is used which combines the effects of both viscous (characterized by the capillary number) and buoyancy (Bond number) forces on residual saturation. For 2-D flow, the trapping number is defined as

$$N_T = \sqrt{N_{Cl}^2 + 2N_{Cl}N_{Bl}\sin\theta + N_{Bl}^2}\ , \qquad 5\text{-}21$$

where θ is the angle of the local flow vector relative to the horizontal direction. The normalized residual oil saturation S_{or}^* can be related to the trapping number through

$$\frac{S_{or}^* - S_{or}^{high}}{S_{or}^{low} - S_{or}^{high}} = \frac{1}{1 + T_o N_T}\ , \qquad 5\text{-}22$$

where T_o is a parameter determined from experimental measurements of residual saturations at corresponding trapping numbers. In this study, we assumed that the residual oil saturation at high trapping number, S_{or}^{high}, = 0. The residual oil saturation at low trapping number was taken to be the residual oil saturation for displacement by ethanol-free water (Table 5.1). A value for the parameter T_o of 6000 was selected from the literature (UTCHEM Tech Documentation, 2000) for Equation 5-22 which defines the capillary desaturation curve. The normalized residual oil saturation, S_{or}^*, versus the trapping number, N_T , curve is shown in Figure 5.4.

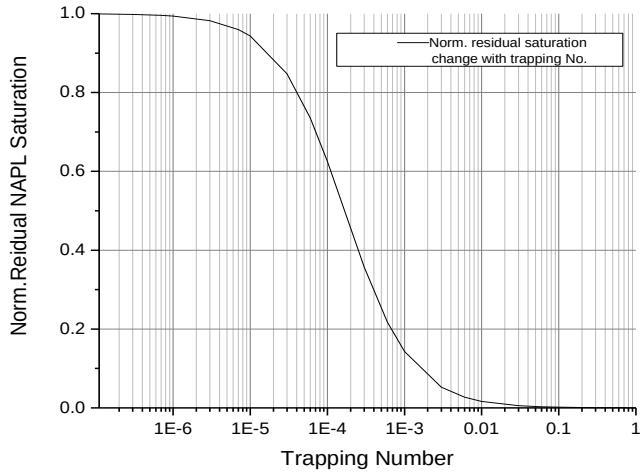

Figure 5.4 NAPL capillary desaturation curve.

From Figure 5.4, higher values of residual NAPL saturation are expected when the ethanol concentration is low, and lower values when the ethanol concentration is high, due primarily to a lowering of IFT (high capillary and corresponding trapping numbers). When the IFT is very low, the NAPL saturation approaches zero. Of course, for very high ethanol concentrations, NAPL is completely dissolved in the aqueous phase.

5.3 2-D Numerical Model

The numerical simulations were based on the 2-D physical model experiments described in Chapter 3. The dimensions of the packed sand (116 cm × 2 cm × 42 cm, Length × Width × Height) were used as the dimensions of the grid system which was discretized into 4872 grid blocks with individual cells having dimensions of 1 cm × 2 cm × 1 cm (Length × Width × Height). The initial pressure inside the aquifer was assumed to be atmospheric pressure and the media was assumed to be initially fully saturated with water. The upper and bottom boundaries were closed boundaries, with no flow and no mass flux across the boundaries. Three wells were built into the grid system which

corresponded to the groundwater inlet port, the flow outlet port, and the fuel injection port in the physical model aquifer (Figure 5.5). The groundwater inlet well and the fuel injection well were single point injection wells with controlled flow rates to simulate the injection and displacement steps used in the physical model experiments. The outlet well was screened over a vertical layer to match the design of the physical apparatus. Hydrocarbon and ethanol concentrations can be calculated at any specified location in the grid system at any given time.

Each simulation consisted of three stages: a fixed volume release of an ethanol/hydrocarbon mixture (10 min) was followed by displacement by groundwater (2 days), which was then followed by injection of a tracer (2 days). During the first stage, a 40-mL ethanol/hydrocarbon fuel blend was released into the saturated zone as a point source at a constant injection rate of 4 ml/min for 10 minutes. The groundwater flow was maintained at a constant injection rate of water through the inlet well. After 10 minutes, the hydrocarbon injection was shut off and groundwater flow continued for another two days to simulate the water displacement process. For the last stage, an aqueous solution containing a conservative tracer was introduced in the inlet well. A total volume of 400 mL of the tracer solution was injected, then tracer-free groundwater flow continued for another 2 days. The process conditions for the simulations corresponded to those for the physical model experiment. Five fuel blends with varying ethanol content were investigated: E15, E25, E50, E85, and E100.

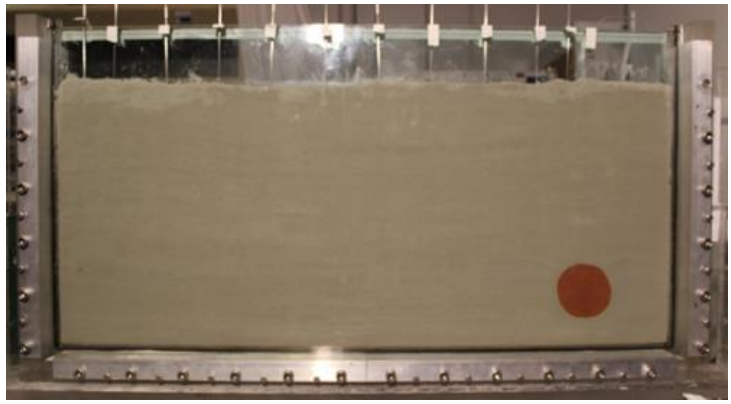

(a)

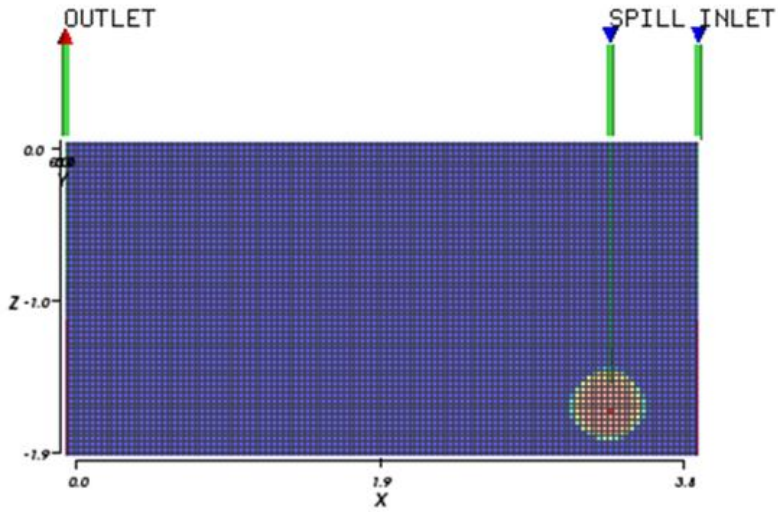

(b)

Figure 5.5 (a) 2-D physical model aquifer used for laboratory experiments. (b) Corresponding grid design for the 2-D numerical simulations.

5.4 Simulation Results and Discussion

5.4.1 History Matching Approaches

Initial values for the numerical model parameters were estimated from literature values for the physical properties of the fluids and the media as described in previous sections. In order to provide a best fit to the experimental results the following parameters were adjusted: intrinsic permeability, solute dispersivity, and parameters for

relative permeability. The intrinsic permeability in the vertical direction was determined from the vertical movement of the ethanol plume. Since accurate head measurements were not available, the horizontal permeability was taken as equal to the vertical intrinsic permeability for the simulations. The longitudinal dispersivity was determined based on the visualization of the ethanol plumes. A value of 0.3 cm for the longitudinal dispersivity was used in the model. Typically, transverse dispersivities measured are 5 to 100 times smaller than longitudinal dispersivities (Charbeneau, 2000). However in this study, both the experiments and the simulation results suggested that the transverse dispersivity was not a significant contribution to solute transport and spreading, thus the same value, 0.3 cm, was also used for the transverse dispersivity throughout the simulations.

Recall from Chapter 3, after ethanol was depleted from the source, the source region was highly saturated with NAPL for the low ethanol content spill cases. However, since the residual NAPL saturation value used in the model was lower than these observed NAPL saturations, in order to compensate for the reduction in the groundwater velocity passing through the high NAPL saturation regions, the relative permeability end point of the aqueous phase at residual NAPL saturation was adjusted based on the observed behavior of the ethanol "tails" generated for the low- to medium-ethanol content spill experiments. These three parameters were determined by a best overall fit of the ethanol plume results considering all of the spill cases. The values for intrinsic permeability and the relative permeability parameters were presented in Table 5.1. The impact of these parameters on the model results are discussed further in Chapter 6.

5.4.2 Ethanol Transport Behavior

The numerical simulation results are compared with the corresponding visualization experimental results in Figures 5.6-5.9. The general agreement between the simulations and the experiments for the ethanol plume behavior for the various fuel blends indicates that the numerical model captures the effect of ethanol concentrations on the fluid properties (e.g., density, viscosity) that results in a buoyant plume following a release into an aquifer under constant groundwater flow conditions.

For E15, E25 and E50 spills, the visualization experimental results indicated two distinct ethanol plumes. While the majority of the ethanol in the fuel mixture partitioned into the aqueous phase and transported vertically due to buoyancy and horizontal groundwater flow, some ethanol remained in the NAPL phase and slowly emanated from the NAPL source. Several factors may contribute to this behavior: the complex phase behavior occurring near the source of the release, the effects of buoyancy and horizontal groundwater flow on the ethanol plume, the flow path of the displacing water which is influence in part by the presence of NAPL in the pores, and the heterogeneity of the media.

The results from the post-tracer experiments described in Chapter 4.3.1 indicated that significant bypassing of the NAPL source area by groundwater flow occurred, especially for the low ethanol content fuels that produced NAPL regions of high saturation. In the simulations, a low aqueous phase relative permeability endpoint was used for calculating groundwater flow in the source region in order to capture the observed transport behavior of the ethanol plume for the fraction of ethanol that slowly emanated from the NAPL source. With decreasing ethanol content in the fuel mixture,

the effects of buoyancy were reduced resulting in a more horizontal plume. The lower the ethanol content in the spilled fuel mixture, the longer the time required for all of the ethanol to be removed from the NAPL source. This was in agreement with the observations from the 2-D physical experiments. Using the same fluid and aquifer parameters, when the ethanol content in the fuel increased to 85% (E85), the simulations predicted an ethanol plume that migrated vertically to the upper part of the tank with a negligible fraction of ethanol remaining in the NAPL phase, in agreement with the physical model experiment for E85. For this case, the simulations also captured the flow instability behavior resulting in plume separation (fingering) that was observed in the visualization experiments. Since the simulations assumed a homogeneous aquifer, this plume separation effect is not due to media heterogeneity. Also, since similar behavior was observed for E100 (Figure 3.7), the effect is not due to ethanol/water/NAPL phase behavior. This likely reflects the effect of composition dependent fluid properties (viscosity, density) of ethanol-water mixtures.

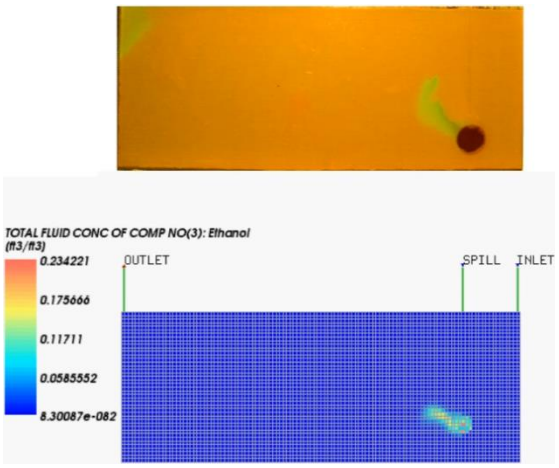

(a) 6 hours

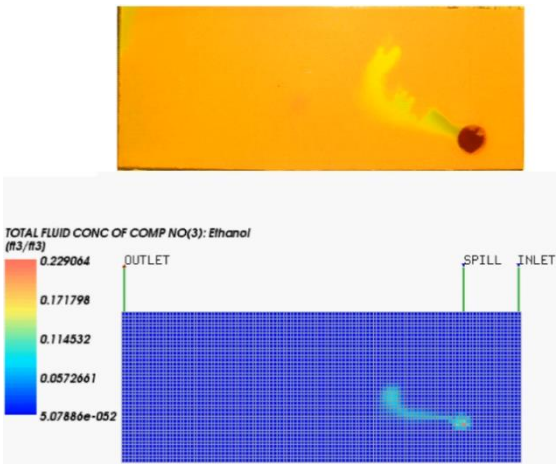

(b) 12 hours

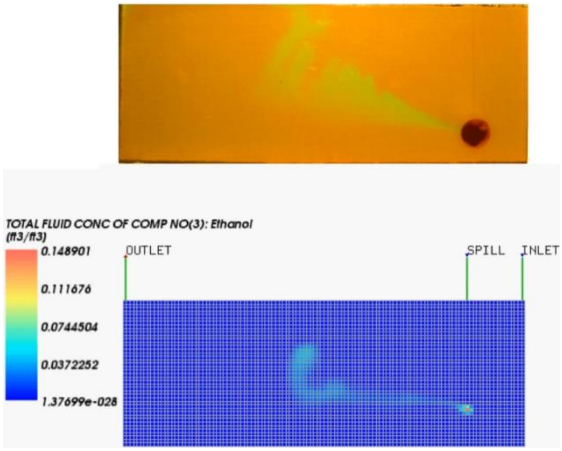

(c) 24 hours

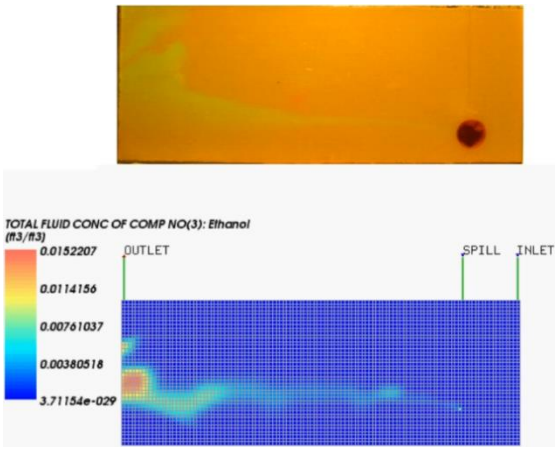

(d) 48 hours

Figure 5.6 Ethanol plume transport for a release of E15. Comparisons of visualization experiments (upper figures) and numerical simulations (lower figures).

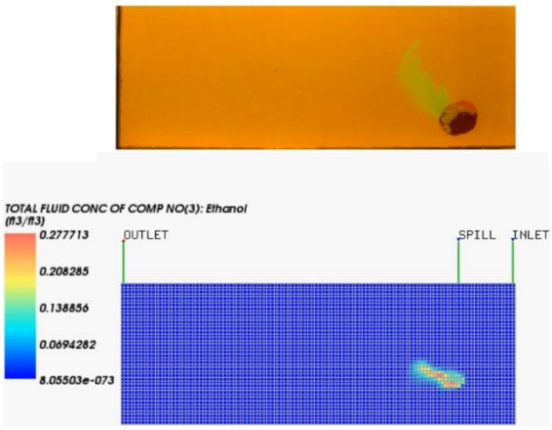

(a) 6 hours

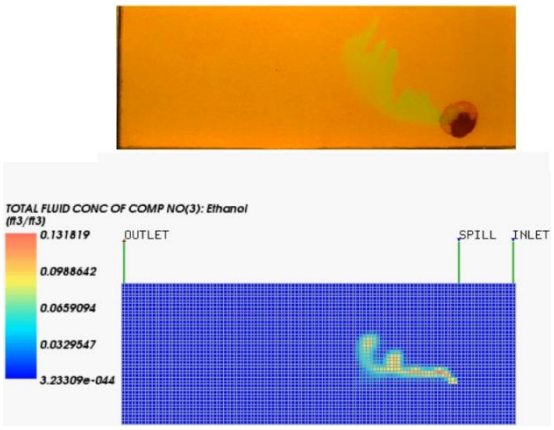

(b) 12 hours

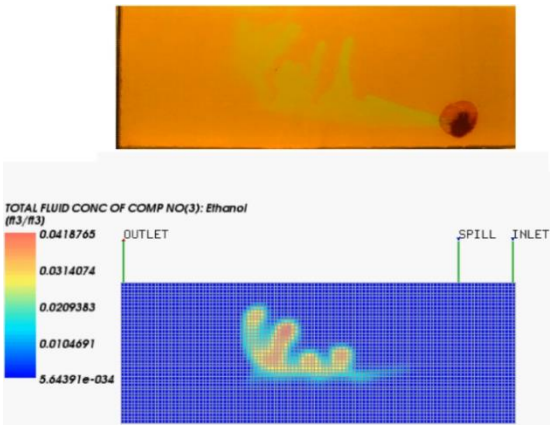

(c) 24 hours

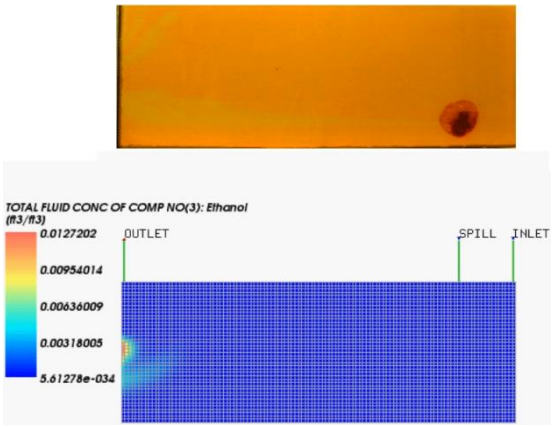

(d) 48 hours

Figure 5.7 Ethanol plume transport for a release of E25. Comparisons of visualization experiments (upper figures) and numerical simulations (lower figures).

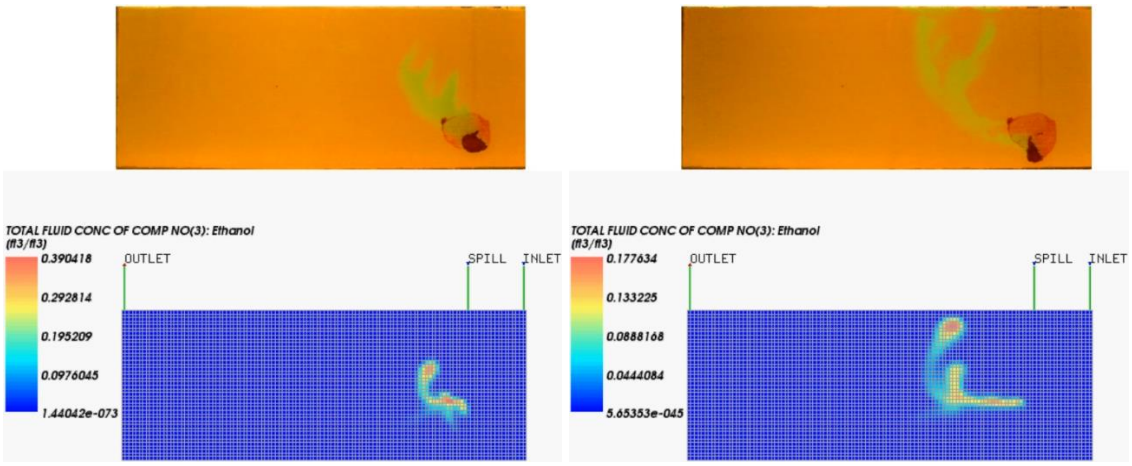

(a) 6 hours (b) 12 hours

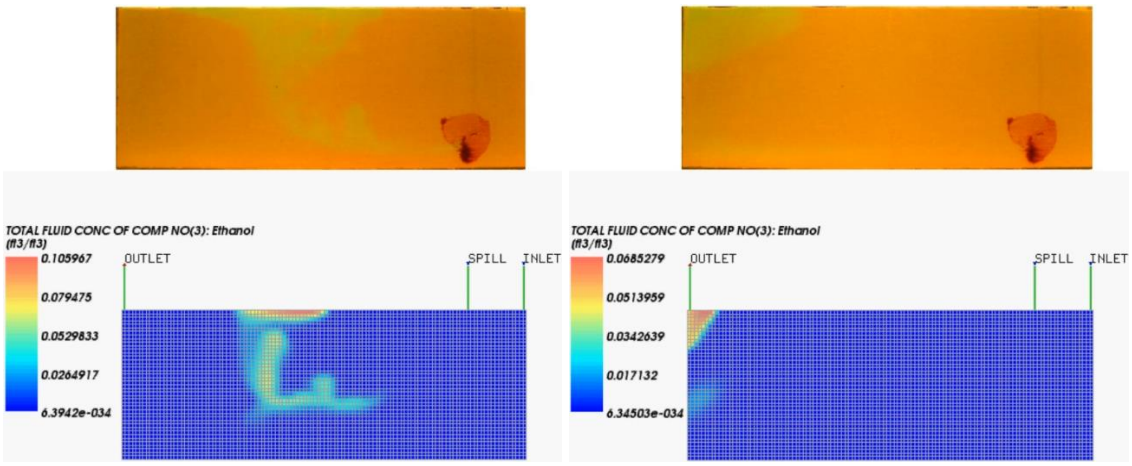

(c) 24 hours (d) 48 hours

Figure 5.8 Ethanol plume transport for a release of E50. Comparisons of visualization experiments (upper figures) and numerical simulations (lower figures).

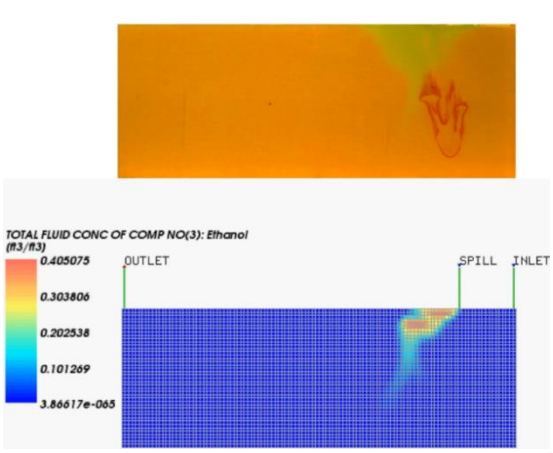

(a) 6 hours

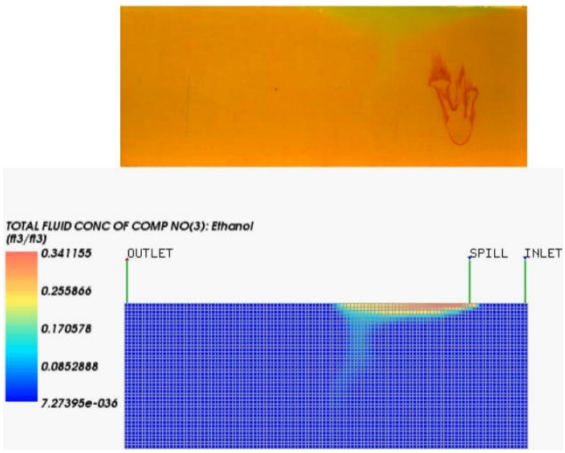

(b) 12 hours

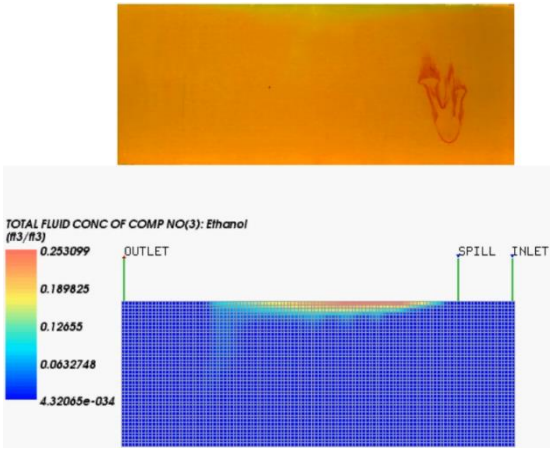

(c) 24 hours

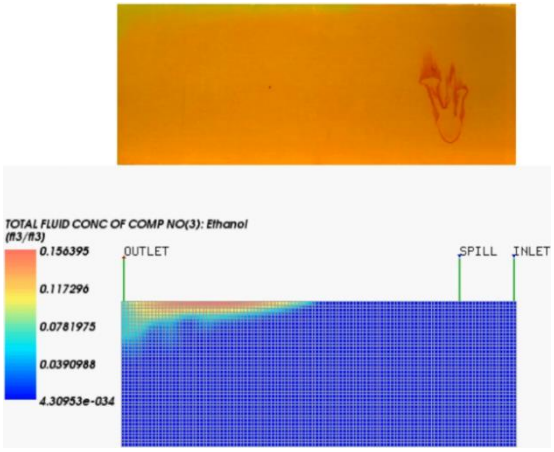

(d) 48 hours

Figure 5.9 Ethanol plume transport for a release of E85. Comparisons of visualization experiments (upper figures) and numerical simulations (lower figures).

5.4.3 NAPL Formation and Migration

The numerical simulations are compared with the visualization results for the residual NAPL source distributions formed from different ethanol fuel spills in Figure 5.10. The simulations were able to capture the general trends in NAPL formation observed in the physical model experiments for the various ethanol fuel blends. The simulations and experiments both show that as the ethanol content increases, the average saturation of the NAPL remaining after the spill decreases. For the higher ethanol content fuel (especially E85), the NAPL saturation is low in the core and high around the edges of the NAPL region.

Despite predicting the general trends, some differences between simulations and experiments were observed for the various fuel blends. For the E15 spill case, the expected behavior was that the NAPL phase would migrate vertically due to buoyancy and laterally due to the hydraulic gradient with displacement by groundwater until residual saturation was reached (typically a residual NAPL saturation of 0.3 for water-wet media). However, this was not observed in the experiments where little displacement of NAPL by water occurred with an apparent average remaining NAPL saturation of 0.79 (Table 3.3). Significant bypassing of the groundwater flow occurred around the NAPL impacted region, thereby impeding further NAPL displacement. The simulations were conducted assuming a residual NAPL saturation of 0.3 (at low values of trapping number). As a result, the simulations predicted a larger NAPL source area of lower average saturation (Figure 5.10a). Note for this case, the NAPL saturations in the upper portion of the NAPL region had not yet reached residual saturation (0.3) two days after the fuel release.

For the E25 spill, two distinct NAPL regions were formed in the experiments: an upper region of low saturation and a lower region with high saturation (Figure 5.10b). The results of the simulations showed more evenly distributed NAPL. Both simulations and experiments yielded a NAPL source that extended upward at an angle reflecting the direction of groundwater flow with a larger areal extent than for the E15 spill.

For the E50 spill, formation of NAPL due to phase separation during vertical migration of the concentrated ethanol plume was observed in both the experiments and the simulations. The NAPL areal extent increased significantly relative to E25 with a much lower average NAPL saturation of 0.19 (Table 3.3). The simulations yielded a toroidal-shaped NAPL with an outer NAPL region with a (residual) saturation of 0.3 and an inner core at lower NAPL saturation. This was somewhat different from the experimental results, where the NAPL saturation was more uniform over a larger area that included the central part of the NAPL impacted region (Figure 5.10c).

For E85, both the experiments and simulations showed a more pronounced formation of NAPL due to phase separation during migration of the ethanol plume. In both the simulations and experiments, a NAPL "ring" of high saturation was formed with a large core area of very low NAPL saturation. However, the irregular shape of the upper NAPL region observed in the experiments, likely due to fingering from instabilities in the upward movement of the ethanol plume, was not observed in the simulations. A trail of NAPL (above the main NAPL impacted area) that precipitated from the ethanol plume as it traveled away from the source was observed in both the experiments and simulations.

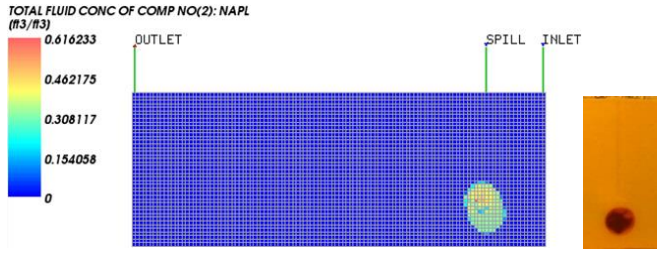

(a) E15

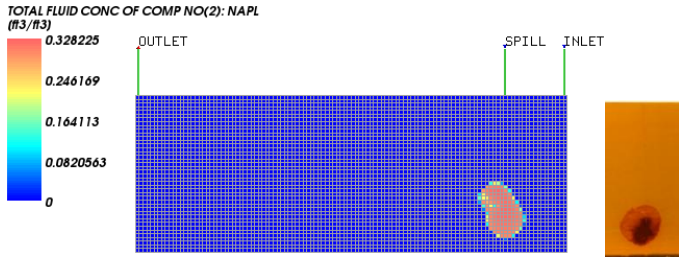

(b) E25

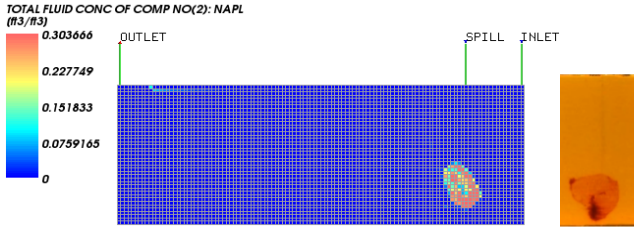

(c) E50

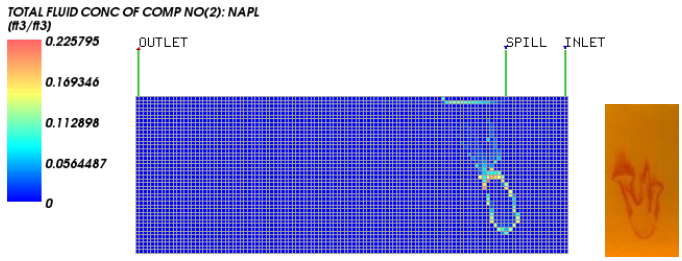

(d) E85

Figure 5.10 NAPL saturation distributions two days after ethanol fuel blend releases. Comparisons of numerical simulations (left) and visualization experiments (right).

5.4.4 Post-tracer analysis

As described in 5.4.1 the residual NAPL saturation used in the simulations was lower than that observed in the low ethanol fuel content 2-D physical model experiments. Since the residual saturation value used in the model was lower than the observed NAPL saturations, in order to compensate for the reduction in groundwater velocity passing through the high NAPL saturation regions, the relative permeability end point for the aqueous phase was reduced based on the observed tailing of the ethanol plume. As further confirmation of the simulated reduced velocity, post-tracer numerical simulations were conducted and compared with the post-tracer 2-D experiment. Results are shown in Figures 5.11-5.14.

For E15, using the adjusted relative permeability parameters to compensate for the lower simulated vs. experimental residual NAPL saturation, the simulations captured the flow path and velocity of groundwater passing through the NAPL impacted region. The aqueous velocity through the NAPL region was significantly reduced with groundwater flowing around the NAPL source area, similar to what was observed in the 2-D experiment (Figure 5.11b).

For E25, as discussed in 5.4.3, the simulations yielded a more evenly distributed NAPL region than that observed in the experiments. A redistribution of the NAPL occurred when ethanol was being removed from the NAPL phase and formed a high NAPL saturation area in the lower central area with a lower NAPL saturation in the upper region. The groundwater velocity was greatly reduced in the lower region which resulted in tailing of the tracer. The simulations did not capture the tailing that was observed (Figures 5.12c and d).

For E50, similar to E25, there were some difference in the simulated vs. experiments NAPL distributions as discussed in the previous section. The simulations did show a reduced velocity through the NAPL source as indicated by the tracer simulations and experiments (Figures 5.13 a-d), and also captured some of the tailing that was observed (Figures 5.13c and d).

For E85, in both the simulations and experiments, the movement of the tracer was only slightly impacted by the residual NAPL due to the overall low residual saturation. The model correctly showed that the groundwater velocity was slightly reduced in the upper portion of the NAPL region, where phase separation was greatest and the NAPL saturation was slightly higher (Figures 15.14b and c). See Section 4.3.1 for a discussion on the implications of these tracer tests for the longer-term dissolution of hydrocarbons from the NAPL sources generated for the various ethanol fuel blends.

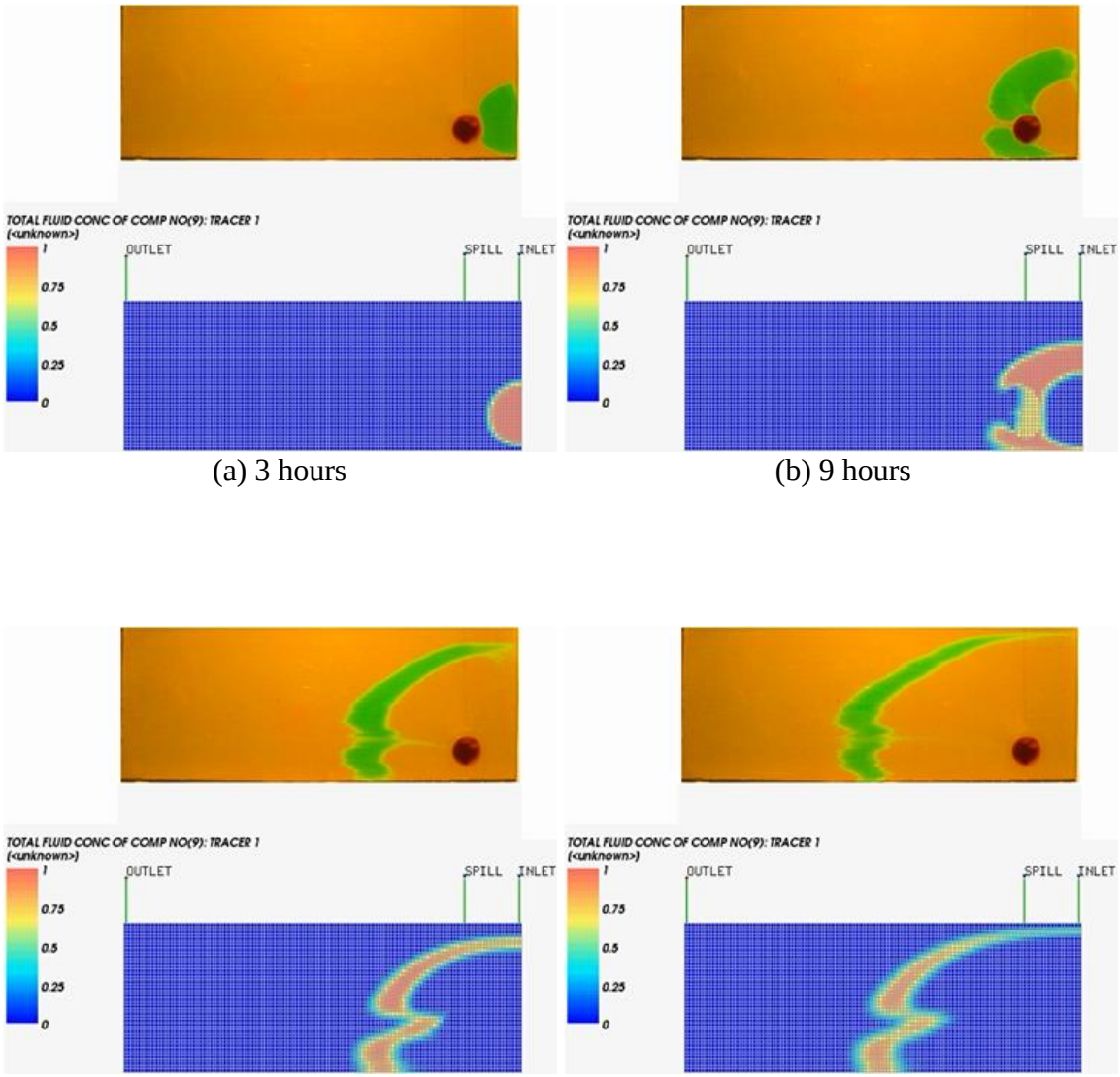

(a) 3 hours (b) 9 hours

(c) 15 hours (d) 24 hours

Figure 5.11 Post-tracer study of groundwater passing through the NAPL source formed from an E15 spill. Comparison of numerical simulations (bottom) and experiments (top).

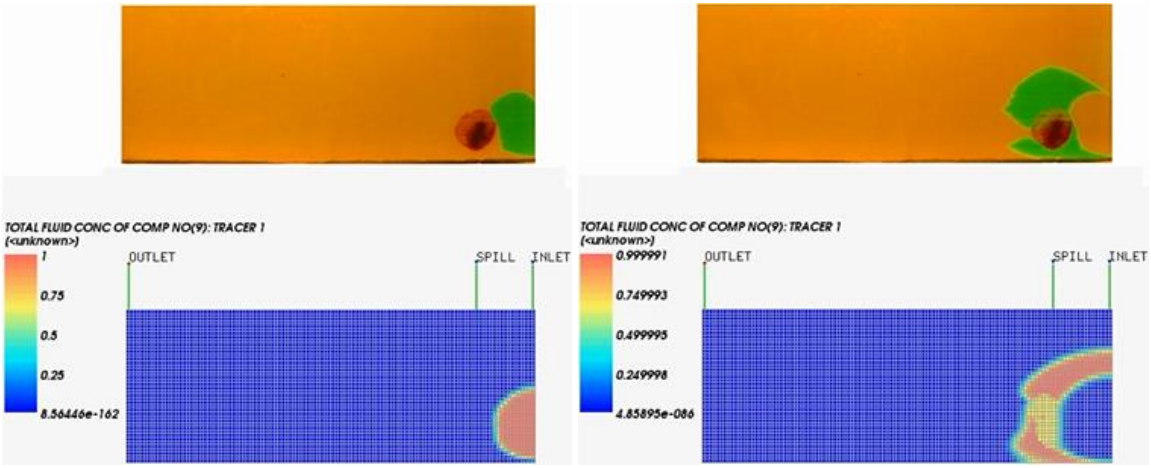

(a) 3 hours

(b) 9 hours

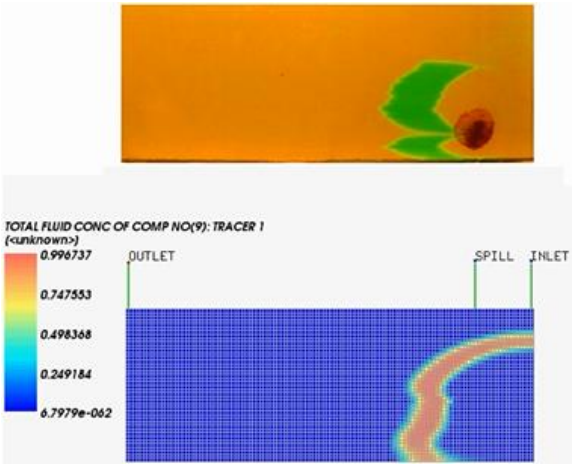

(c) 15 hours

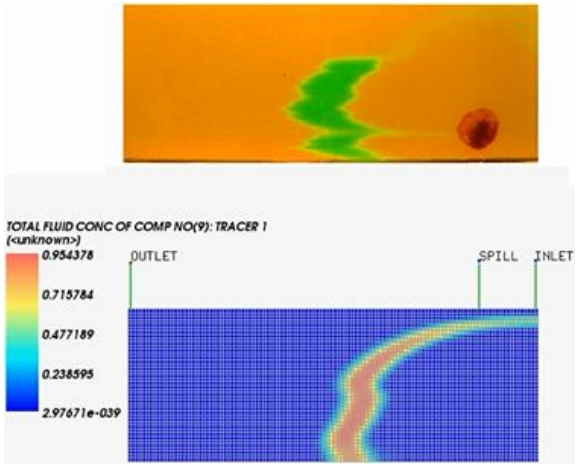

(d) 24 hours

Figure 5.12 Post-tracer study of groundwater passing through the NAPL source formed from an E25 spill. Comparison of numerical simulations (bottom) and experiments (top).

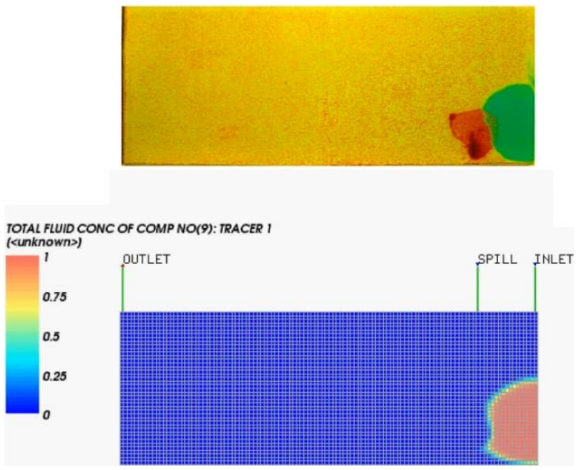

(a) 3 hours

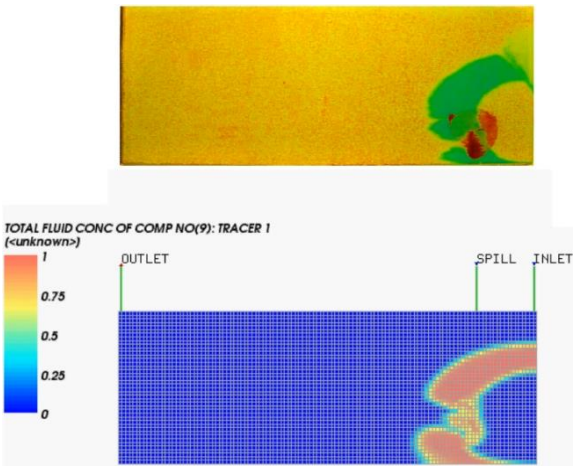

(b) 9 hours

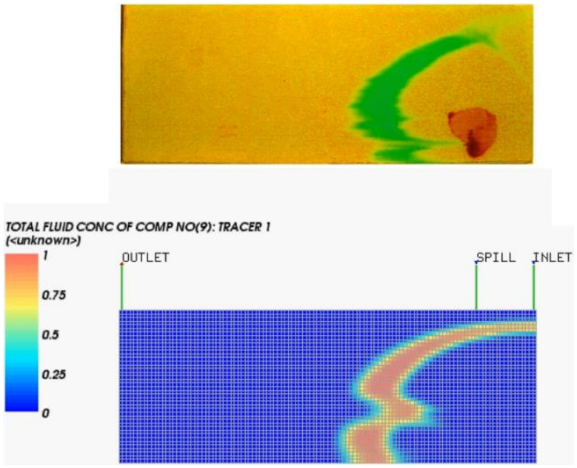

(c) 15 hours

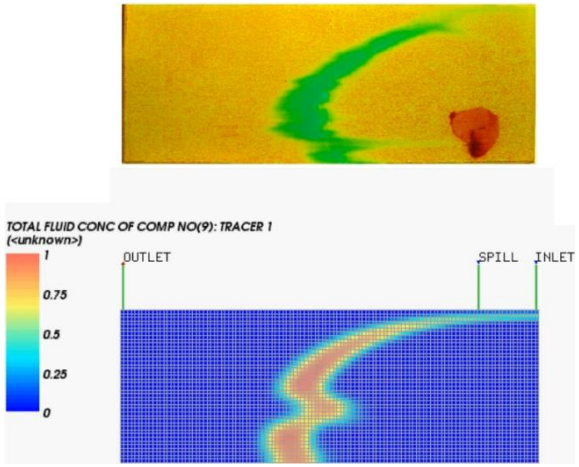

(d) 24 hours

Figure 5.13 Post-tracer study of groundwater passing through the NAPL source formed from an E50 spill. Comparison of numerical simulations (bottom) and experiments (top).

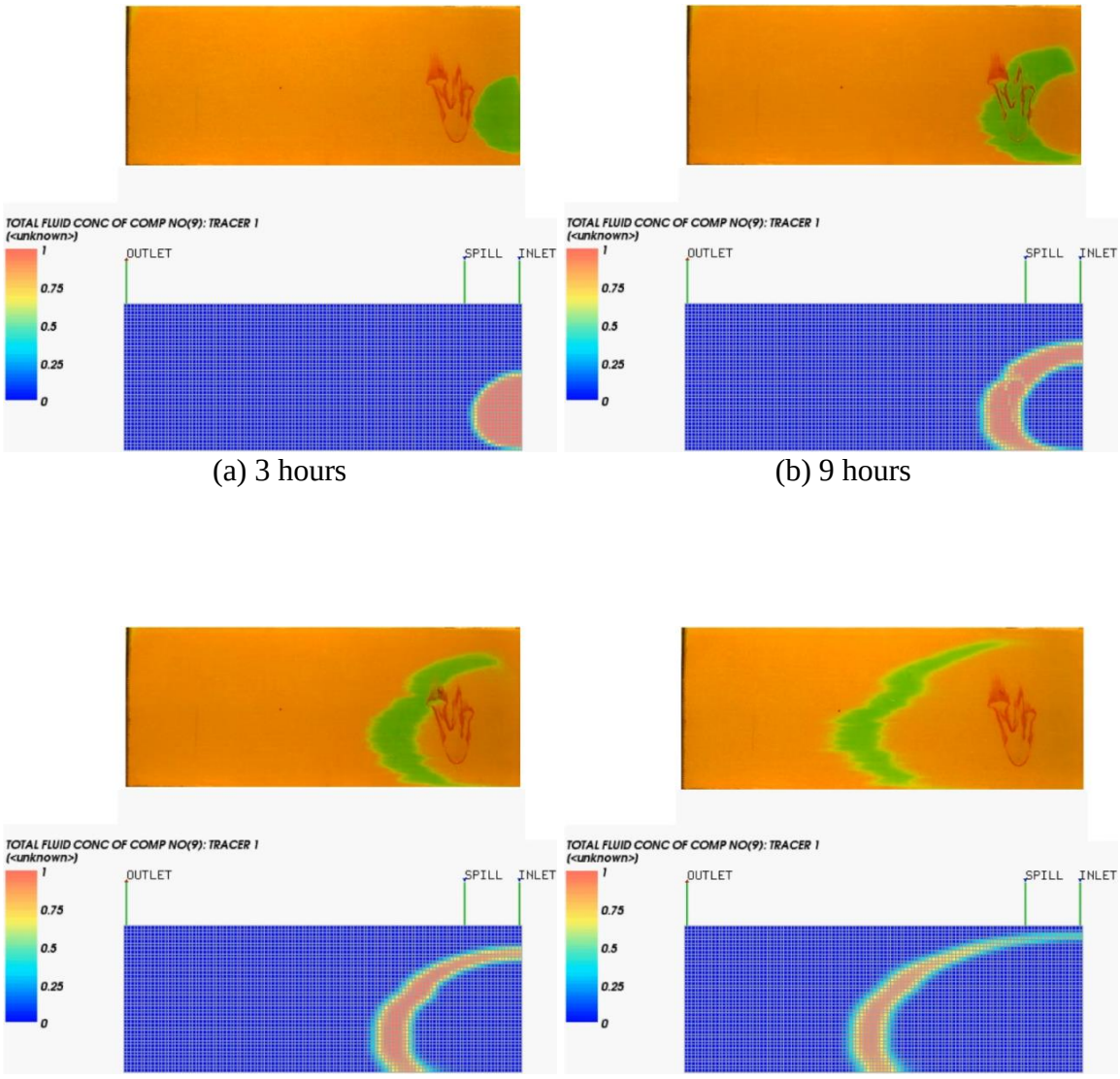

(a) 3 hours (b) 9 hours

(c) 15 hours (d) 24 hours

Figure 5.14 Post-tracer study of groundwater passing through the NAPL source formed from an E85 spill. Comparison of numerical simulations (bottom) and experiments (top).

CHAPTER 6 SENSITIVITY ANALYSIS

6.1 Introduction

In the simulation studies described in the previous chapters, the numerical model parameter inputs were initially determined based on literature experimental data and then were calibrated based on the 2-D physical model experimental results. However a well calibrated model does not necessarily represent the real physical conditions; the complex heterogeneity in a real aquifer system and the uncertainly of the input parameters from the data gaps often pose challenges which may affect the model performance significantly. In this chapter, sensitivity analyses were conducted for the parameter inputs regarding the fluid and media properties that may have considerable impact on the overall simulation results. The objectives of the sensitivity analyses were to: (1) increase understanding of the relationships between the input parameters and the simulation output; (2) identify the inputs that have no or minor effect on the overall output, thereby reducing the amount of information required for a particular simulation to simplify the simulations; and (3) estimate the level of uncertainty in the simulation results.

6.2 Parameter Selection

6.2.1 Porosity and Permeability

Permeability and the porosity of the media are principal media properties of a reservoir. Porosity is a function of the sorting of the media, while permeability is dependent on both grain size and sorting. Both porosity and permeability increase with improved sorting (Figure 6.1). When sorting decreases, smaller particles can fill the pore space between the larger grains, resulting in a decrease in porosity and permeability.

Fluid phase parameters, such as capillary pressure, are also dependent on porosity and permeability.

The permeability used in the simulations discussed in Chapter 5 is consistent with a very well sorted fine sand (Figure 6.1). In this chapter, simulations were conducted to determine the impact of permeability and porosity on plume transport and NAPL distributions. Three simulation cases were conducted by varying permeability at a constant porosity, and two simulations cases were conducted by using lower porosity values compared to the one used in all previous simulations in Chapter 5, while the permeability was held constant. The permeability and porosity values selected for the different cases are listed in Table 6.1.

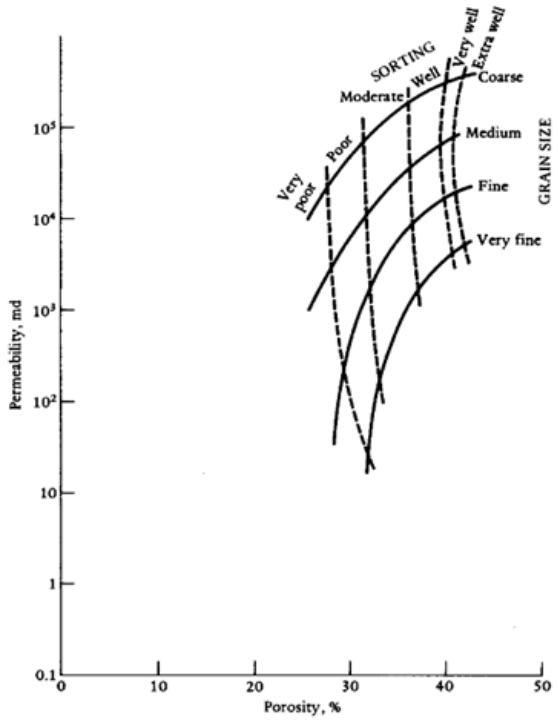

Figure 6.1 Effect of grain size and sorting on permeability and porosity for uncemented sands. Selly (1998)

Table 6.1 Simulations to assess impact of permeability and porosity.

	Sorting	Media size	Porosity	Permeability
Case 1	Well sorted	Medium	0.4	30000
Case 2	Poor	Fine	0.4	1500
Case 3	Well	Fine	0.4	8500
Case 4	Very well	Fine	0.3	12000
Case 5	Very well	Fine	0.2	12000

In addition to the effects on permeability for different soil types for a homogeneous aquifer, heterogeneity is another important factor that needs to be considered. In this study, two typical layered aquifers were constructed, each with two hypothetical layers. The first case assumed the layer above the layer where the spill occurred (0-27 cm) had an intrinsic permeability two times higher than the permeability of the spill region. In the second case, the permeability above the spill region was reduced to 1/2 and 1/10 of its original value. The results were compared with the simulation results for a homogeneous aquifer.

6.2.2 Viscosity

In addition to permeability, fluid viscosity is another important property that has direct impact on the fluid velocity. For multiphase flow, it also affects the mobility of the displacing phase, which determines the displacement efficiency.

As shown in Figure 6.2, the viscosity of aqueous solutions of ethanol has a maximum over the range of alcohol concentrations from 0 % to 100 %. The mixture viscosity equation used in the previous simulations in Chapter 5 was able to capture such

characteristics. However, linear curves are more commonly used to determine fluid mixture properties in multiphase flow models when mixture data are not available. In order to investigate the impact of assuming linear viscosity curves on the transport process, additional simulations were conducted for which ethanol aqueous solution viscosity was assumed to be linear function of alcohol concentration as shown in Figure 6.2.

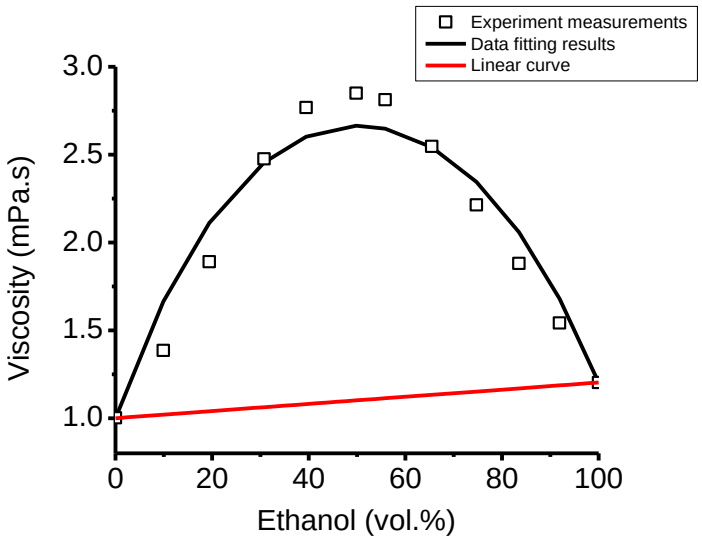

Figure 6.2 Ethanol-water mixture viscosities.

6.2.3 Interfacial Tension

Interfacial tensions between the oil phase and water phase were calculated from the phase compositional data generated from the phase equilibrium model in UTCHEM. IFT is used to calculate many other important fluid media properties such as capillary pressure, residual phase saturation, and the trapping number. IFTs are usually acquired from laboratory measurements for a specific fluid system of interest. These data are not generally available. In this study, IFTs were not measured for the fluid system used in the 2-D physical model experiment. Instead, IFT data for a typical gasoline-water system

were used. Since there were some differences in the gasoline compositions used in the model vs. experiment, additional simulations were conducted to determine the sensitivity of the simulated transport behavior to changes in IFT.

In order to investigate the importance of the IFT on alcohol fuel transport behavior, the E15, E25, E50, and E85 spill simulations conducted in Chapter 5 were repeated with the compositional dependent IFT model replaced with a constant IFT model. The IFT between the hydrocarbon phase and the water phase was fixed at the value without the presence of any alcohol. The results were then compared with the corresponding cases with alcohol.

6.2.4 Relative Permeability Curves

One of the major assumptions in the previous simulations was assuming that groundwater flow was significantly hindered when passing through the NAPL phase. This was achieved by assigning a small value for the oil phase end point permeability (the permeability at residual oil saturation). This value is normally determined from imbibition/drainage capillary pressure experiments for the specific media and fluid system. To assess the effect that this endpoint permeability value has on the displacement process, additional simulations were conducted using hypothetical relative permeability curve exponents and endpoint values based on more typical relative permeability curves (Brown et al., 1994). For this case, the water displacement process was assumed to follow imbibition, and the fuel injection process was assumed to follow drainage. The model parameters that were used are listed in Table 6.2 and corresponding capillary pressure and relative permeability vs. saturation plots are shown in Figure 6.3.

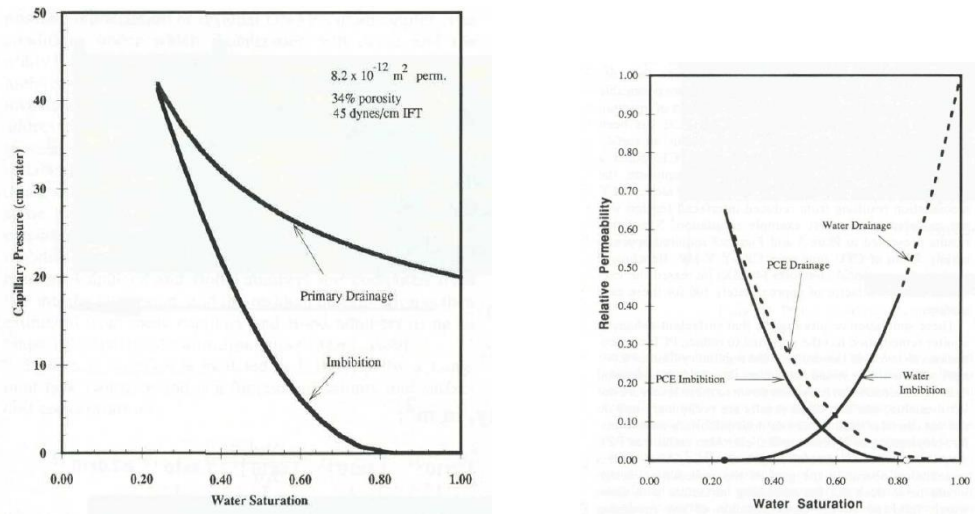

(a) (b)

Figure 6.3 (a) Capillary pressure-saturation curve and (b) relative permeability-saturation curve derived from a typical capillary pressure-saturation experiment. (Brown et al.,1994)

Table 6.2 Typical relative permeability parameters and values used in the simulations.*

	Imbibition	Drainage
S_{ow}	-	0.24 (0.1)
S_{or}	0.17 (0.3)	-
k_{ro}	0.49	1 (0.6)
k_{rw}	0.65	0.65 (0.01)
n_o	2.7	2.7 (2)
n_w	2.85	2.85 (4)
c	0.44	0.21
λ	-0.5	1.92

* Values used in the simulations are shown in parentheses.

6.3 Results and Discussion

6.3.1 Impact of Permeability and Porosity

For the homogenous media Cases 1 to 3 (Table 6.1), the permeability varied from 1,500 mD to 30,000 mD. The E50 spill case was used to study the impacts. Compared to the simulation results of previous chapters for a permeability of 12,000 mD (referred to as the "base case" in the following discussion), a decrease in permeability caused the ethanol plume to rise more slowly, and an increase in permeability caused a more rapid rise. The effect was not significant for Cases 1 and 3, for which the permeability differed by factors of 2.5 and 0.7, respectively. However when the permeability was reduced to 1500 mD (Case 2), the ethanol plume migrated horizontally with the groundwater flow with negligible upward movement. The change in permeability did not have a significant impact on the distribution of the NAPL phase as the vertical extent of the hydrocarbon phase was limited even for the high permeability cases. For Cases 4 and 5, the porosity was reduced to 0.3 and 0.2, respectively for a constant permeability of 12,000 mD. With reduced porosity, the constant fuel volume injected impacts a larger area. Therefore a larger area residual NAPL source was formed compared to the base case. For the same reason, the ethanol plume traveled faster in both the horizontal and vertical directions. The results for Cases 1 to 5 can be found in Appendix D.

For the heterogeneity studies, increasing or decreasing the permeability in the layer above the spill layer by a factor of two did not have a significant impact on the overall transport behavior of the ethanol plume, as already indicated in the homogenous media studies (Case 1 and 3). A slight increase (higher permeability in upper layer) or decrease (lower permeability in upper layer) in the degree of vertical movement of the

ethanol plume was observed, as shown in Figures 6.4 and 6.5, respectively. However, when the upper layer permeability was decreased to 1/10 that of the spill layer, the upward movement of the ethanol plume was restricted by the upper layer. The vertical component to the velocity of the ethanol plumes was significantly reduced when the ethanol plume hit the low permeability layer as shown in Figure 6.6. A similar effect was observed for the higher ethanol content case (E85), as shown in Figure 6.7. For the NAPL distributions that were generated, lower permeability for the upper layer impacted the E85 case significantly. The vertical extent of the residual NAPL was limited due to the lower vertical migration of the ethanol plume from which the NAPL phase separates. This resulted in a more horizontal shaped residual NAPL distribution profile, and the differences in the overall shapes and areal extents between the residual NAPL distributions generated from the E50 and E85 spills were reduced (compare Figures 6.8c and d with Figure 5.10c and d). This would be expected to impact the longer-term dissolution characteristics of hydrocarbons (e.g., BTX) from NAPL.

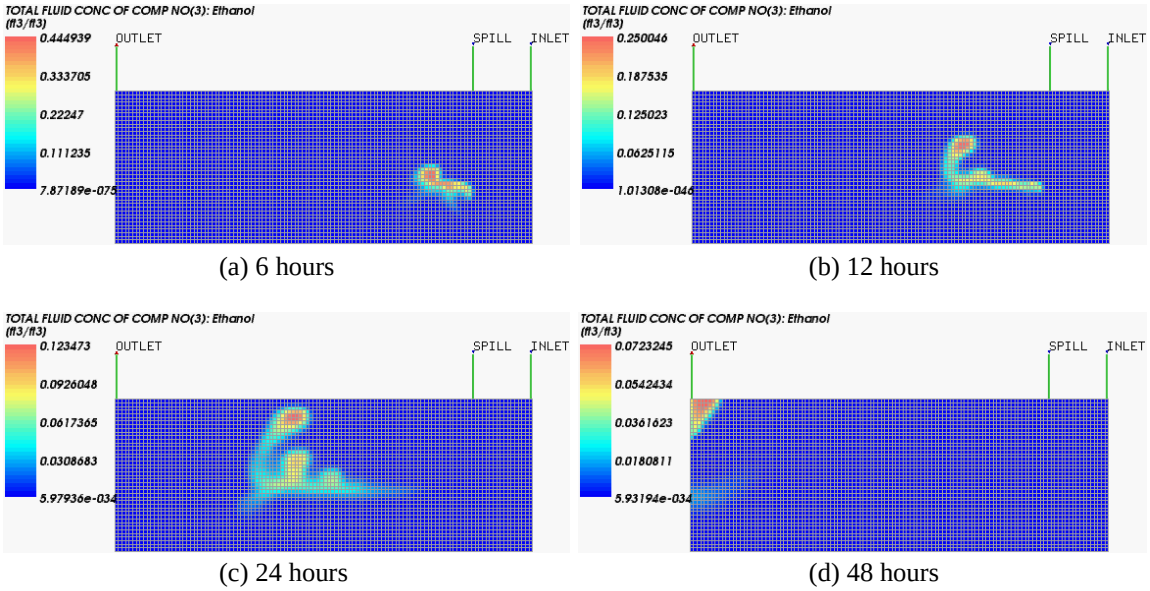

(a) 6 hours (b) 12 hours

(c) 24 hours (d) 48 hours

Figure 6.4 E50 ethanol plume behavior in a layered system. Permeability above the spill region was ½ that of the spill layer

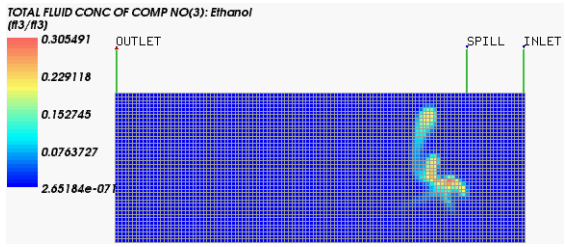

(a) 6 hours

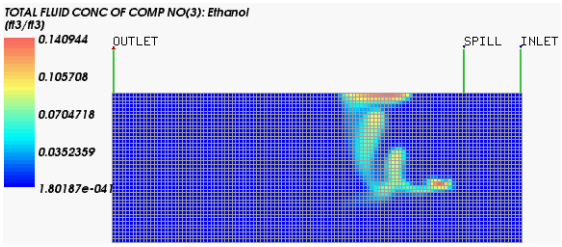

(b) 12 hours

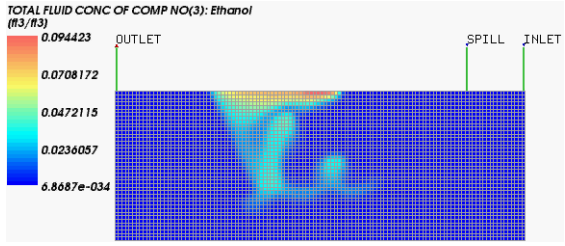

(c) 24 hours

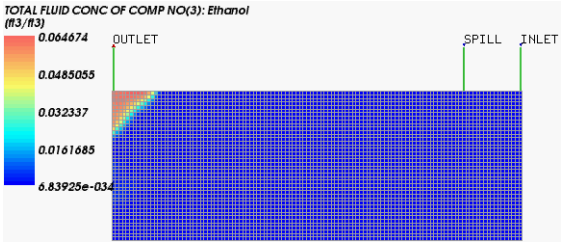

(d) 48 hours

Figure 6.5 E50 ethanol plume behavior in a layered system. Permeability above the spill region was two times that of the spill layer.

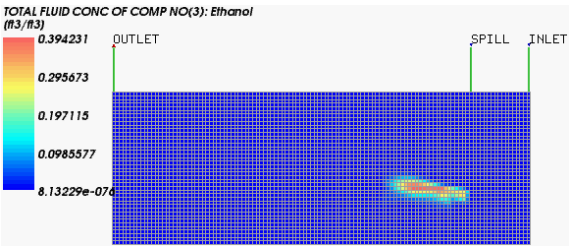

(a) 6 hours

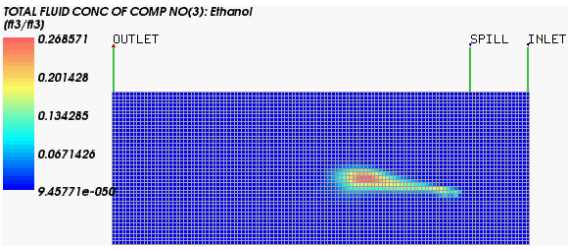

(b) 12 hours

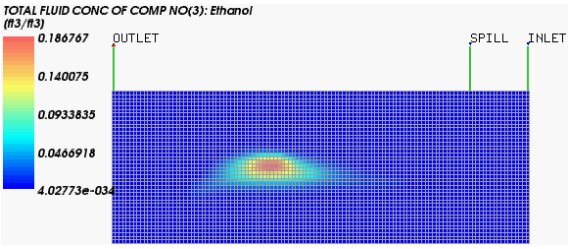

(c) 24 hours

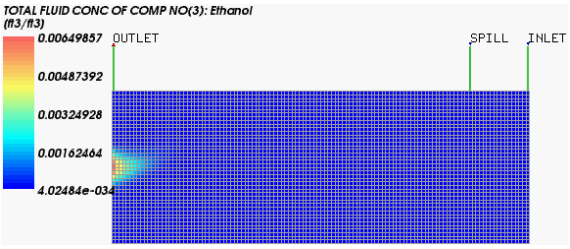

(d) 48 hours

Figure 6.6 E50 ethanol plume behavior in a layered system. Permeability above the spill region was 1/10 that of the spill layer.

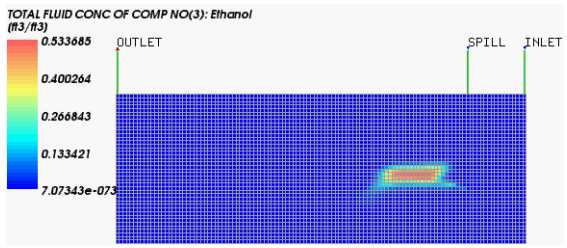

(a) 6 hours

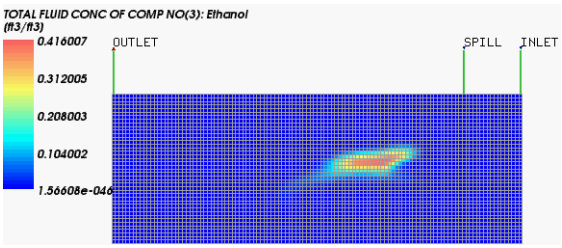

(b) 12 hours

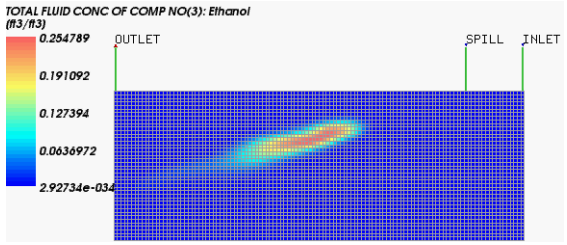

(c) 24 hours

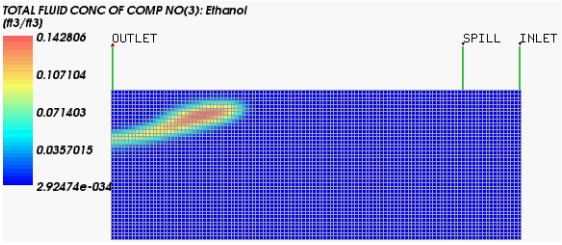

(d) 48 hours

Figure 6.7 E85 ethanol plume behavior in a layered system. Permeability above the spill region was 1/10 that of the spill layer.

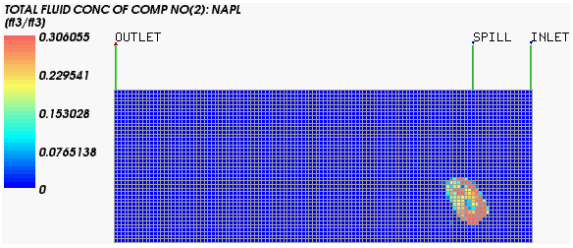

(a) E50, 1/2 permeability in layer above the spill region

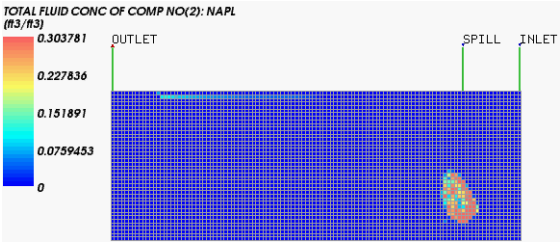

(b) E50, 2x permeability in layer above the spill region

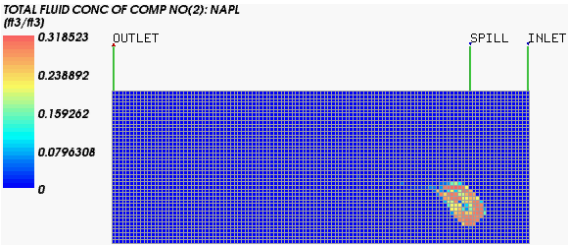

(c) E50, 1/10 permeability in layer above the spill region

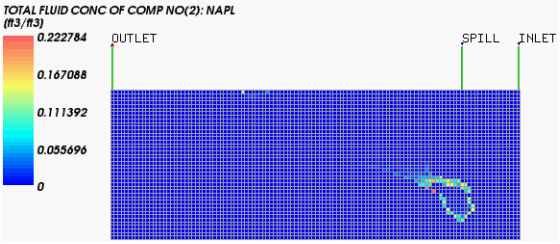

(d) E85, 1/10 permeability in layer above the spill region

Figure 6.8 Residual NAPL saturation distributions for E50 and E85 spills in a layered system. Values for the permeability in the layer above the spill point are expressed in fraction of the permeability in the spill layer.

6.3.2 Impact of Composition Dependent Viscosities

The simulation results in Figure 6.9 shows that a linear dependence of aqueous mixture viscosities on alcohol concentration produced an alcohol plume that rose more rapidly compared to those using the actual, non-linear mixture viscosity (Figure 5.8). The more rapid rise was due to the reduced average viscosity of the alcohol plume. The difference in plume rise was greatest at the early times after the release when the dissolved alcohol concentrations were in the concentration range where the actual mixture viscosities were at a maximum (Figure 6.2). As the alcohol plume attenuated during migration, the impact from the lower viscosity was less significant due to the lower ethanol concentrations.

The NAPL distributions generated assuming linear mixture viscosities (Figure 6.10) were the same as those using actual mixture (non-linear) viscosities (Figure 5.10). Thus, the viscosity of the alcohol-water mixtures may not have a significant impact on the overall NAPL source behavior for releases of ethanol-blended fuels.

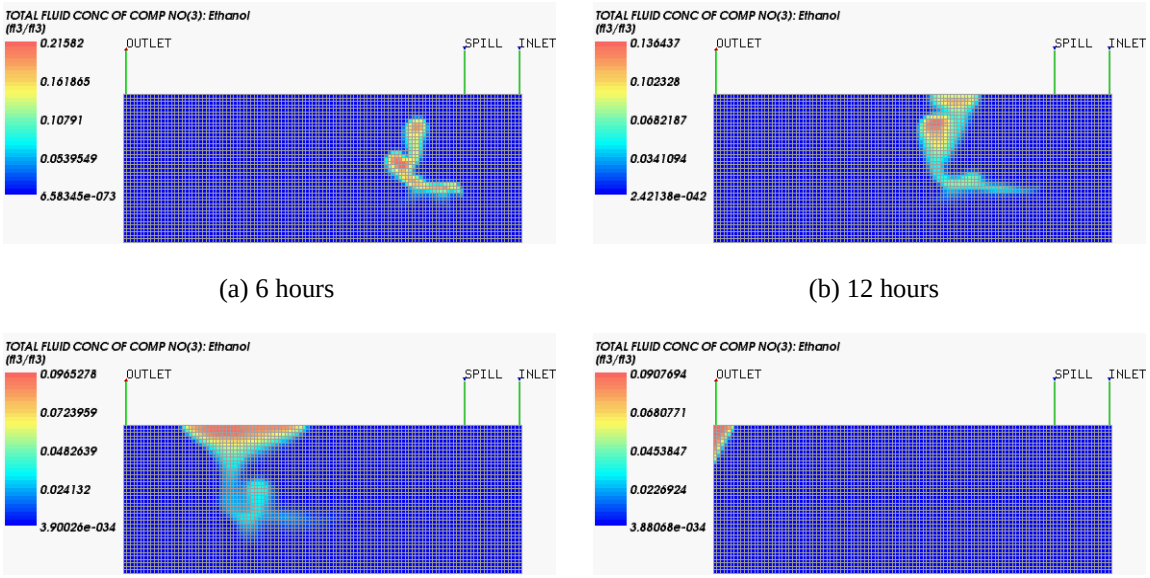

(a) 6 hours (b) 12 hours

(c) 24 hours (d) 48 hours

Figure 6.9 E50 ethanol plume behavior with linear aqueous mixture viscosities.

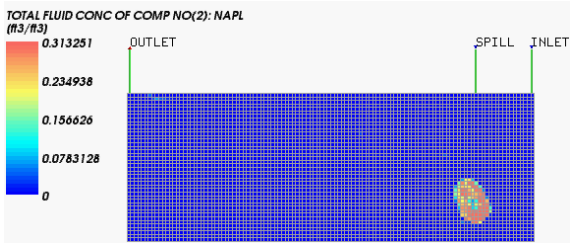

Figure 6.10 Residual NAPL saturation distributions for E50 spill with linear aqueous mixture viscosities.

6.3.3 Impact of interfacial tension

The composition dependent IFT model was replaced with a constant IFT between the aqueous and NAPL phases. As shown in Figures 6.11 and 6.12 (vs. Figures 5.6 and 5.7) partitioning of ethanol from the NAPL phase to the aqueous phase occurred more rapidly after the fuel release for both E15 and E25 spills, and "tailing" of the ethanol plumes emanating from the NAPL sources was not observed. The ethanol plumes were more concentrated and rose more quickly. The residual NAPL footprint generated for the E25 spill was reduced, and the residual NAPL phase was more uniformly distributed (Figure 6.15b vs. Figure 5.10b).

For E50 and E85, constant IFT did not have a significant impact on the overall results; the transport of the ethanol plume (Figures 6.13 and 6.14) and the distribution of the NAPL phase (Figures 6.15c and d) were almost identical to the results using a composition dependent IFT model (Figures 5.8 and 5.9 and Figure 5.10c-d). For E85, a NAPL impacted area was formed that had an outer ring of high NAPL saturation with a low NAPL saturation in the core, identical to what was generated for E85 using a composition dependent IFT model. NAPL generation was solely dependent on the equilibrium phase behavior for NAPL and aqueous phases in the presence of ethanol; changes in IFT had a neglible impact.

Thus, for high ethanol content spills, a phase equilibrium model may be sufficient for modeling alcohol plume transport and NAPL source generation. For low ethanol content spills, changes in interfacial tension need to be considered.

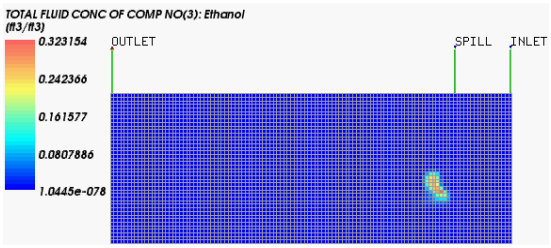

(a) 6 hours

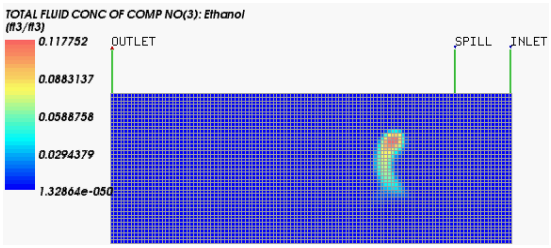

(b) 12 hours

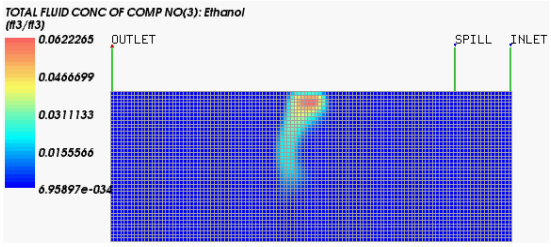

(c) 24 hours

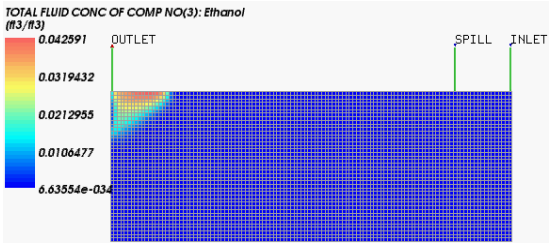

(d) 48 hours

Figure 6.11 E15 ethanol plume behavior for constant IFT.

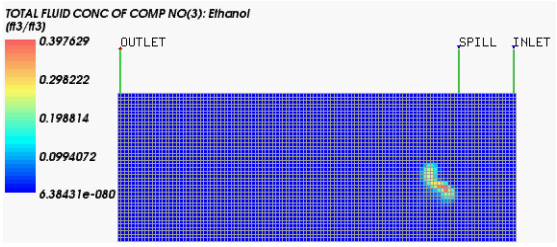

(a) 6 hours

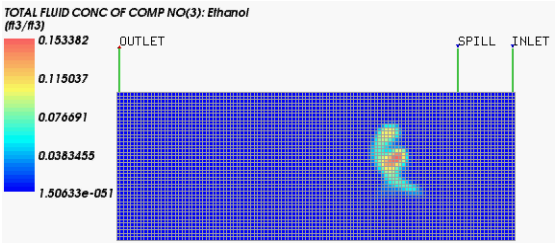

(b) 12 hours

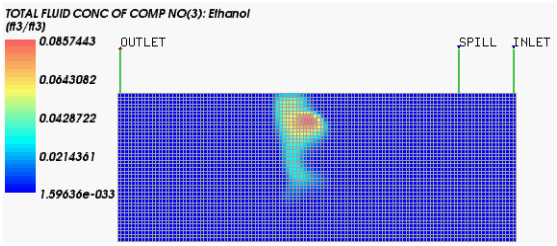

(c) 24 hours

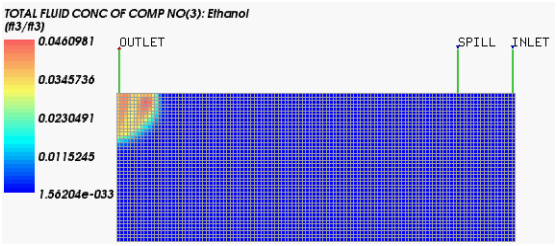

(d) 48 hours

Figure 6.12 E25 ethanol plume behavior for constant IFT.

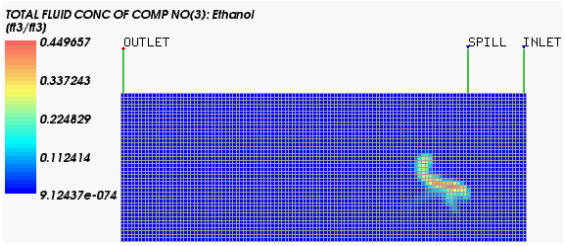

(a) 6 hours

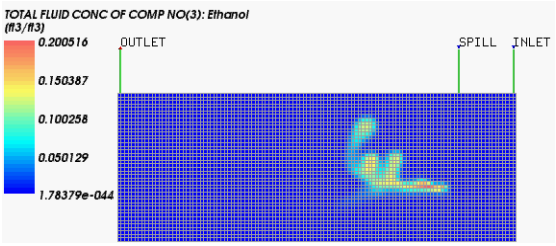

(b) 12 hours

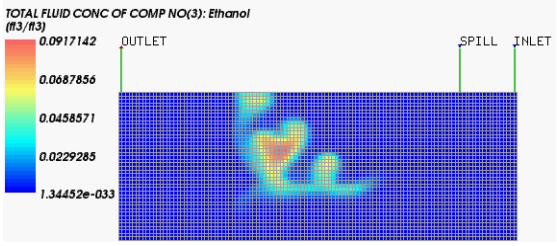

(c) 24 hours

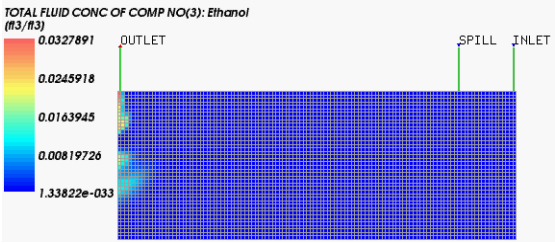

(d) 48 hours

Figure 6.13 E50 ethanol plume behavior for constant IFT.

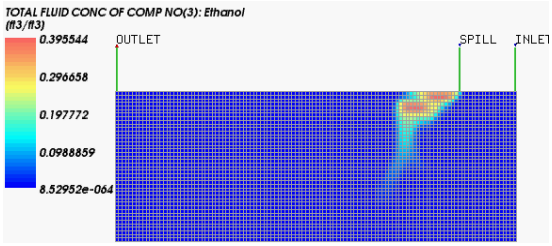

(a) 6 hours

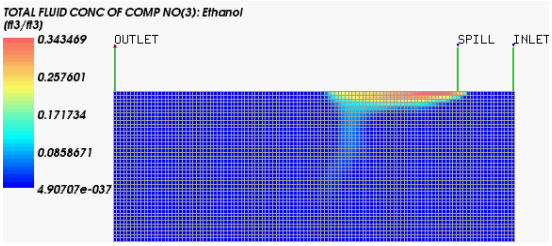

(b) 12 hours

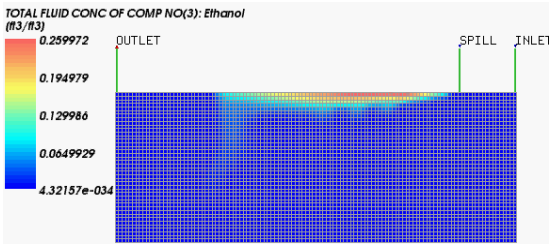

(c) 24 hours

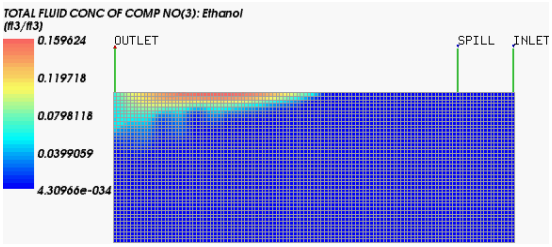

(d) 48 hours

Figure 6.14 E85 ethanol plume behavior for constant IFT.

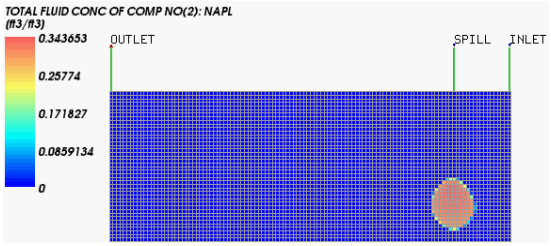

(a) E15

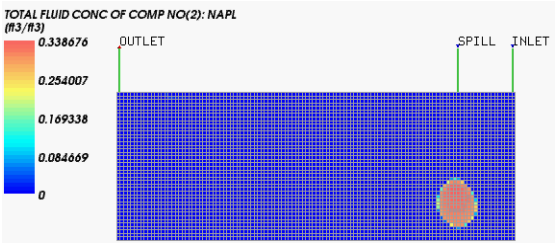

(b) E25

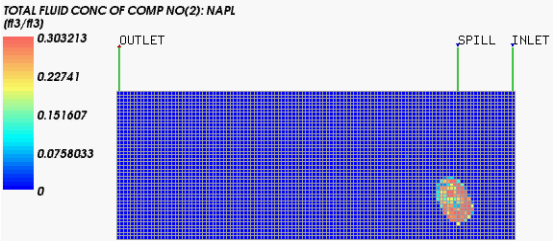

(a) E50

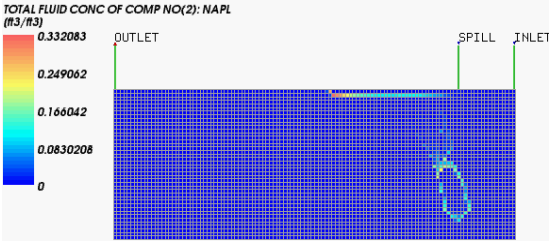

(b) E85

Figure 6.15 Residual NAPL saturation profiles for (a) E15, (b) E25, (c) E50, and (d) E85 for constant IFT.

6.3.4 Effect of Relative Permeability Curves

Using a more typical value for the relative permeability endpoint for the aqueous phase increased the groundwater flow velocity that passed through the NAPL source region. As a result, the ethanol plume became more uniform and was less impacted by NAPL (Figure 6.16 vs. Figure 5.8). This produced a more concentrated plume that rose more rapidly compared to the base case. Higher ethanol concentrations increased the solubilities of hydrocarbons resulting in phase separation further downstream that formed a wider residual NAPL source distribution (Figure 6.17 vs. 5.10d).

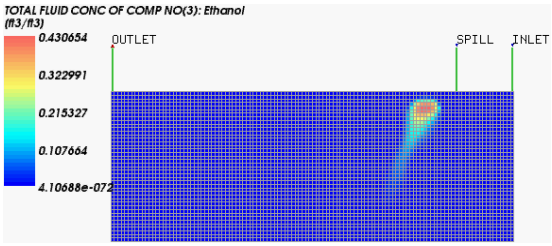

(a) 6 hours

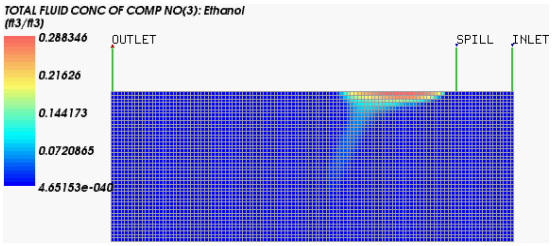

(b) 12 hours

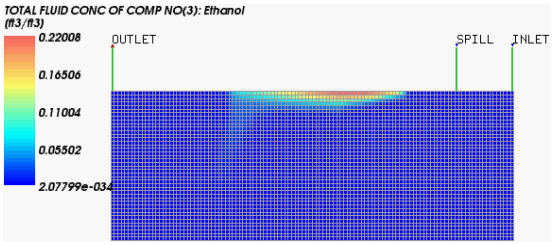

(c) 24 hours

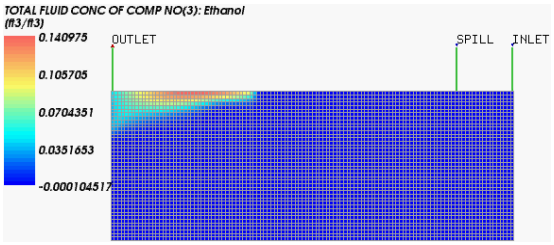

(d) 48 hours

Figure 6.16 E50 ethanol plume behavior simulated using typical capillary pressure, relative permeability, and residual saturation parameters.

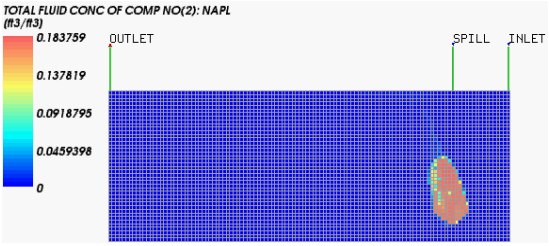

Figure 6.17 E50 residual NAPL saturation profile simulated using typical capillary pressure, relative permeability, and residual saturation parameters.

CHAPTER 7 CONCLUSIONS

7.1 Physical model experiments

7.1.1 Source Generation and Transport Behavior

2-D visualization experiments for ethanol fuel blends have shown that the presence of an alcohol can significantly impact NAPL source behavior. The size, shape, and distribution of the NAPL phase were dependent on the alcohol content in the fuel mixture.

The presence of alcohol in the fuel mixture reduces interfacial tension, thereby reducing the pore entry pressure for a non-wetting fluid. Thus, media heterogeneity did not affect the spreading of the fuel mixtures as they were injected for all of the fuels studied (E15, E25, E50, and E85). This was in contrast to experiments for fuels with ethanol contents < 15% (E10, E5, and E0). For these fuels, the distribution of the NAPL phase was irregular which was likely due to some stratification of the media during packing.

After fuels were injected into the aquifer, a fraction of the hydrocarbons remained as an immobile NAPL phase. However, the partitioning and transport of ethanol from the fuels had a significant impact on the migration of a second fraction of NAPL, and the NAPL distribution for this fraction was highly dependent on the alcohol content in the fuel mixture. Spills of fuels of high ethanol content produced concentrated ethanol plumes that rapidly rose due to buoyancy which led to the formation of NAPL during subsequent phase separation along the path of the alcohol plume. For the low ethanol content spill cases, the areal extent of the final NAPL source distribution increased only slightly from the areal extent observed immediately after the fuel was injected. As

ethanol left the source area, a local redistribution of NAPL was observed which was dependent on ethanol content in the fuel. Overall, based on the visualization results for E15 to E85, the size of the NAPL impacted area increased with increasing ethanol content.

Enhanced dissolution of hydrocarbons was observed in the ethanol plumes. This enhanced dissolution was observed for spills of ethanol blended fuel blends with ethanol contents above 25% (E25). The measured pore water concentrations for the individual hydrocarbons were close to the equilibrium concentrations for aqueous ethanol solutions (in equilibrium with NAPL), and the enhancements were higher for the hydrocarbons with lower pure component solubilities. The enhanced dissolution was greatest for the high alcohol content spill cases, and decreased when the alcohol concentration decreased. High measured hydrocarbon concentrations were generally associated with the high alcohol concentrations.

The migration of the alcohol plume occurred both vertically by buoyancy and laterally by groundwater flow. For spills of high ethanol content fuels (e.g., E85), buoyancy was significant, and a rapid rise of the alcohol plume was observed. For lower alcohol content fuels, the vertical rise of the alcohol plume was reduced, and a fraction of the alcohol was retained and released slowly from the NAPL remaining near the source by groundwater flow. Lower ethanol content fuel mixtures required longer times to displace all of the alcohol from the source. This suggests that for low ethanol content fuel spills, a longer-term release of the alcohol should be expected. For spills of high alcohol content fuels, buoyancy of the alcohol plume is great enough that most of the

alcohol would accumulate near the water table above and downstream of the point of release.

7.1.2 Dissolution of Hydrocarbons from a Residual NAPL Source

The residual NAPL distributions formed from the various ethanol fuel spills determined the elevation and the extent of the hydrocarbon plume. The NAPL distributions also determined the dissolution rate and source strength for the individual hydrocarbon components in the fuel mixture. Based on the results of the post-spill tracer experiments, groundwater flow near the NAPL source varied for fuels of different ethanol content. For spills of low ethanol content fuels, most of the groundwater flow bypassed the NAPL impacted region. As ethanol content increased, the average NAPL saturation decreased, and less bypassing of NAPL by groundwater occurred. For higher ethanol content spills, equilibrium dissolution was approached, resulting in faster depletion of hydrocarbons. For low to intermediate ethanol content fuels, the tracer experiment also indicated that a small fraction of the groundwater flow was able to pass through a region of high NAPL saturation within the NAPL impacted area, but at a significantly reduced velocity. So for the low to intermediate ethanol content fuels, dissolution of hydrocarbons occurred by mass transfer-limited dissolution to groundwater from by-passed NAPL as well as by advection of groundwater through the NAPL source.

The results from the pore water hydrocarbon measurements were in agreement with the post-tracer studies. A thin, pseudo steady-state plume was formed emanating from the residual NAPL source to the aquifer outlet, and the elevation of this plume was aligned with the elevation of the residual NAPL source. The persistence of the individual hydrocarbons during the 4-week dissolution experiment decreased in the following order:

TMB > m-xylene > toluene > benzene. For all of the spill cases investigated, TMB did not deplete over the entire period, while benzene depleted rapidly for all cases except E25. The poor contact between the NAPL and groundwater for the E25 case resulted in mass transfer-limited dissolution of benzene. The tracer experiment for E50 indicated that there were two regions in the source: one region of lower saturation where groundwater flow readily passed through the NAPL, and a second region of higher NAPL saturation where groundwater flow was hindered. This could lead to two phases of dissolution: equilibrium dissolution observed initially, followed by mass transfer limited-dissolution. For E85, due to good contact between the NAPL phase and groundwater passing through the NAPL source, rapid depletion occurred for more soluble hydrocarbons most likely due to equilibrium dissolution. These conclusions were also inferred by analysis of the experiment results with an equilibrium dissolution model.

These results suggest that hydrocarbon contaminants could persist in groundwater for spills of low ethanol content fuels due to the high saturation of NAPL sources generated from these fuels. For spills of fuels with high ethanol content, higher hydrocarbon concentrations in pore water would be expected in the short term following a spill due to hydrocarbons dissolved in the ethanol plume. However, in the longer-term the pore water concentrations would decrease more rapidly than for the low ethanol content spills.

7.2 Numerical Simulations

Numerical simulations using UTCHEM were conducted to complement the physical model experiments to evaluate the source generation and transport behavior of spills of ethanol blended fuels released to the subsurface. The agreement between the

results of simulations and experiments demonstrated the possibility of predicting source generation and transport of NAPL and ethanol from fluid and media properties. It also provided a better understanding of the effect of alcohol, a cosolvent for hydrocarbons, on the overall transport and distribution of hydrocarbons released to the subsurface in the form of ethanol blended fuels.

The numerical simulation studies indicated that the ethanol-hydrocarbon-water phase equilibria and the alcohol content in the fuel mixture were the main factors controlling NAPL source behavior. The simulations predicted that, for the same volume of fuel released, the NAPL impacted areas resulting from spills of fuels of varying alcohol content were similar in size. Consequently, as the ethanol content in the fuel mixture increased, the average residual NAPL saturation within the source area decreased. NAPL saturation was lower in the center of the NAPL source and higher at the edge of the source area. This effect became apparent for E50, but was more pronounced for E85, for which the residual NAPL saturation approached zero in the center.

UTCHEM was not be able to capture the high NAPL saturation formed from spills of some fuels with low to medium alcohol content (e.g., E15 and E25) that was observed in the physical model experiments. For those cases, the simulated values approached residual NAPL saturation. As a result, for those cases relative permeability parameters were modified to account for the observed lower groundwater velocity passing through the NAPL source.

The numerical model was also used to investigate the impact of additional fluid and media properties on alcohol plume transport and NAPL distribution. The permeability of the media has a significant impact on the release behavior of the alcohol

plume which affects the distribution of the immiscible hydrocarbon phase, particularly for spills of the high alcohol content fuels. Fluid viscosity directly affects the fluid transport, however, due to the rapid dilution of the alcohol plume, the overall transport behavior of the ethanol plumes and the residual NAPL distribution profiles were not significantly affected by changes in viscosity. Therefore, a simple linear mixture viscosity model may be sufficient to estimate plume transport behavior. Changes in IFT between the aqueous and NAPL phases were found to have a significant impact on source behavior for the low ethanol content spill cases. For high ethanol content spills, the phase equilibria controlled alcohol partitioning as well as the phase separation and final distribution of NAPL formed from the fuel spill.

This study indicates that UTCHEM could be a useful tool for modeling the multi-phase fluid transport associated with spills of ethanol blended fuels in porous media. Such a tool may be used to extend the results of this study to a wider range of aquifer and spill conditions. In addition, the results could be extended to other types of alternative fuels containing alcohols provided critical data (phase equilibria, capillary pressure, and relative permeability vs. saturation) are available.

REFERENCES

Akin, S., Castanier, L. M., & Brigham, W. E. (1998). *Effect of temperature on heavy-oil/water relative permeabilities*. Paper presented at the SPE annual technical conference, New Orleans, LA.

Aziz, K., & Settari, A. (1979). *Petroleum reservoir simulation*: Applied Science Publishers.

Backes, H. M., Jing Jun, M., E, B., & G, M. (1990). Interfacial tensions in binary and ternary liquid—liquid systems. *Chemical Engineering Science, 45*(1), 275-286.

Bear, J. (1979). *Hydraulics of groundwater*: McGraw-Hill International Book Co.

Brandani, V., Chianese, A., & Rossi, M. (1985). Ternary liquid-liquid equilibrium data for the water-ethanol-benzene system. *Journal of Chemical & Engineering Data, 30*(1), 27-29.

Brown, C. L., Pope, G. A., Abriola, L. M., & Sepehrnoori, K. (1994). Simulation of surfactant-enhanced aquifer remediation. *Water Resources Research, 30*(11), 2959-2977.

Cápiro, N. L., Stafford, B. P., Rixey, W. G., Bedient, P. B., & Alvarez, P. J. J. (2007). Fuel-grade ethanol transport and impacts to groundwater in a pilot-scale aquifer tank. *Water Research, 41*(3), 656-664.

Charbeneau, R. J. (2000). *Groundwater hydraulics and pollutant transport*: Prentice Hall.

Corey, A. T. (1954). The interrelation between gas and oil relative permeabilities. *Producers monthly, 19*(1), 38-41.

Fredenslund, Å., Gmehling, J., & Rasmussen, P. (1977). *Fredenslund,Aa., J.Gmehling and P.Rasmussen, Vapor-liquid Equilibria Using UNIFAC, a Group-contribution Method*: Elsevier.

Freitas, J. G., & Barker, J. F. (2011a). Oxygenated gasoline release in the unsaturated zone — Part 1: Source zone behavior. *Journal of Contaminant Hydrology, 126*(3–4), 153-166.

Freitas, J. G., Doulatyari, B., Molson, J. W., & Barker, J. F. (2011b). Oxygenated gasoline release in the unsaturated zone, Part 2: Downgradient transport of ethanol and hydrocarbons. *Journal of Contaminant Hydrology, 125*(1–4), 70-85.

Garg, S., & Rixey, W. G. (1999). The dissolution of benzene, toluene, m-xylene and naphthalene from a residually trapped non-aqueous phase liquid under mass transfer limited conditions. *Journal of Contaminant Hydrology, 36*(3–4), 313-331.

González, B., Calvar, N., Gómez, E., & Domínguez, Á. (2007). Density, dynamic viscosity, and derived properties of binary mixtures of methanol or ethanol with water, ethyl acetate, and methyl acetate at T = (293.15, 298.15, and 303.15) K. *The Journal of Chemical Thermodynamics, 39*(12), 1578-1588.

Groves, F. R. (1988). Effect of cosolvents on the solubility of hydrocarbons in water. *Environmental Science & Technology, 22*(3), 282-286.

Hand, D. B. (1929). Dineric Distribution. *The Journal of Physical Chemistry, 34*(9), 1961-2000.

Hassan, M. E., Nielsen, R. F., & Calhoun, J. C. (1953). Effect of pressure and temperature on oil-water interfacial tensions for a series of hydrocarbons. *Journal of Petroleum Technology, 5*(12), 299-306.

Haynes, W. M. (2013). *CRC Handbook of Chemistry and Physics, 94th Edition*: Taylor & Francis Limited.

He, X. (2002). *Ethanol-Enhanced Dissolution of Aromatic Hydrocarbons from Non-Aqueous Phase Liquids in Porous Media.* (Doctoral Dissertation), University of Houston, Houston, TX, U.S.A.

He, X., Stafford, B. P., & Rixey, W. G. (2011). Ethanol-enhanced dissolution of a residually trapped synthetic gasoline source. *Ground Water Monitoring & Remediation, 31*(3), 61-68.

Heermann, S. E., & Powers, S. E. (1998). Modeling the partitioning of BTEX in water-reformulated gasoline systems containing ethanol. *Journal of Contaminant Hydrology, 34*(4), 315-341.

Jawitz, J. W., Sillan, R. K., Annable, M. D., Rao, P. S. C., & Warner, K. (2000). In-situ alcohol flushing of a DNAPL source zone at a dry cleaner site. *Environmental Science & Technology, 34*(17), 3722-3729.

Ji, W., & Brusseau, M. L. (1998). A general mathematical model for chemical-enhanced flushing of soil contaminated by organic compounds. *Water Resources Research, 34*(7), 1635-1648.

Kueper, B. H. (1989). *The behavior of dense, non-aqueous phase liquid contaminants in heterogeneous porous media.* (Doctoral dissertation), University of Waterloo, Waterloo, Ontario, Canada.

Lapidus, L., & Amundson, N. R. (1952). Mathematics of adsorption in beds. VI. The effect of longitudinal diffusion in ion exchange and chromatographic columns. *Journal of Physical Chemistry, 56*(8), 984-988.

Lee, K. (2010). Numerical simulation of surfactant-enhanced remediation of heterogeneous aquifer contaminated with nonaqueous phase liquids. *Journal of Material Cycles and Waste Management, 12*(3), 193-203.

Lee, K. Y. (2008a). Phase partitioning modeling of ethanol, isopropanol, and methanol with BTEX compounds in water. *Environmental Pollution, 154*(2), 320-329.

Lee, K. Y. (2008b). Viscosity of high-alcohol content fuel blends with water: subsurface contaminant transport implications. *Journal of Hazardous Materials, 160*(1), 94-99.

Lee, K. Y., & Ha, D. T. (2012). viscosity variations of three-component mixtures comprising an alcohol, various common groundwater contaminants, and water. *Environmental Engineering Science, 29*(1), 26-34.

Lee, K. Y., & Peters, C. A. (2004). UNIFAC modeling of cosolvent phase partitioning in nonaqueous phase liquid-water systems. *Journal of Environmental Engineering, 130*(4), 478-483.

Letcher, T. M., Wootton, S., Shuttleworth, B., & Heyward, C. (1986). Phase equilibria for (n-heptane + water + an alcohol) at 298.2 K. *The Journal of Chemical Thermodynamics, 18*(11), 1037-1042.

Leverett, M. C. (1941). Capillary behavior in porous solids. *Transactions of the AIME, 142*(1), 152-169.

Liang, H., & Falta, R. W. (2008). Modeling field-scale cosolvent flooding for DNAPL source zone remediation. *Journal of Contaminant Hydrology, 96*(1–4), 1-16.

Lovanh, N., Hunt, C. S., & Alvarez, P. J. J. (2002). Effect of ethanol on BTEX biodegradation kinetics: aerobic continuous culture experiments. *Water Research, 36*(15), 3739-3746.

Ma, J., Xiu, Z., Monier, A. L., Mamonkina, I., Zhang, Y., He, Y., Alvarez, P. J. J. (2011). Aesthetic Groundwater Quality Impacts from a Continuous Pilot-Scale Release of an Ethanol Blend. *Ground Water Monitoring & Remediation, 31*(3), 47-54.

Mamonkina, I. (2011). *Physical-Model Simulations of Spills of Ethanol-Blended Fuels.* (Master thesis), University of Houston, Houston, TX, U.S.A.

McDowell, C. J., & Powers, S. E. (2003). Mechanisms Affecting the Infiltration and Distribution of Ethanol-Blended Gasoline in the Vadose Zone. *Environmental Science & Technology, 37*(9), 1803-1810.

Molson, J., Mocanu, M., & Barker, J. (2008). Numerical analysis of buoyancy effects during the dissolution and transport of oxygenated gasoline in groundwater. *Water Resources Research, 44*(7), W07418.

Oliviera, E. d. (1997). *Ethanol Flushing of Gasoline Residuals: Microscale and Field-Scale Experiments.* (Doctoral dissertation), University of Waterloo, Waterloo, Ontario, Canada.

Oliviera, I. B., Demond, A. H., & Salehzadeh, A. (1996). Packing of sands for the production of homogeneous porous media. *Soil Sci. Soc. Am. J., 60*(1), 49-53.

Poling, B., Prausnitz, J., & Connell, J. O. (2000). *The Properties of Gases and Liquids*: Mcgraw-hill.

Pope, G. A., & Nelson, R. C. (1978). A chemical flooding compositional simulator. *Society of Petroleum Engineers, 18*, 339-354.

Powers, S. E., Abriola, L. M., & Weber, W. J. (1992). An experimental investigation of nonaqueous phase liquid dissolution in saturated subsurface systems: Steady state mass transfer rates. *Water Resources Research, 28*(10), 2691-2705.

Powers, S. E., Hunt, C. S., Heermann, S. E., Corseuil, H. X., Rice, D., & Alvarez, P. J. J. (2001a). The transport and fate of ethanol and BTEX in groundwater contaminated by gasohol. *Critical Reviews in Environmental Science and Technology, 31*(1), 79-123.

Powers, S. E., Rice, D., Dooher, B., & Alvarez, P. J. J. (2001b). Peer reviewed: will ethanol-blended gasoline affect groundwater quality? *Environmental Science & Technology, 35*(1), 24A-30A.

Rixey, W. G., Garg, S., & Nie, Y. (1999). Comparison of the fixed-bed and batch leaching characteristics of aromatic compounds in residually trapped crude oils and oily wastes. *Journal of Hazardous Materials, 64*(2), 137-156.

Rixey, W. G., & Joshi, S. (2000). Dissolution of MTBE from a residually trapped gasoline source. *A summary of research results from API's soil & groundwater technical task force,* (13).

Stafford, B. P. (2007). *Impacts to Groundwater from Releases of Fuel Grade Ethanol: Source Behavior*. (Doctoral dissertation), University of Houston, Houston, TX, U.S.A.

Stafford, B. P., Cápiro, N. L., Alvarez, P. J. J., & Rixey, W. G. (2009). Pore water characteristics following a release of neat ethanol onto pre-existing NAPL. *Ground Water Monitoring & Remediation, 29*(3), 93-104.

Stalkup, F. I. (1983). *Miscible displacement*: Henry L. Doherty Memorial Fund of AIME, Society of Petroleum Engineers of AIME.

Yu, S., Freitas, J. G., Unger, A. J. A., Barker, J. F., & Chatzis, J. (2009). Simulating the evolution of an ethanol and gasoline source zone within the capillary fringe. *Journal of Contaminant Hydrology*, *105*(1–2), 1-17.

APPENDIX A CAPILLARY PRESSURE-WATER SATURATION MEASUREMENTS

The measured capillary pressure-water saturation curve is shown in Figure A.1. The measurements were conducted in a smaller scale apparatus. Due to the height was limited by the boundary of the apparatus, the measurements were stopped at 30 cm above the water table. As can be seen from the plot, the water saturation at 30 cm was still more than 35%, the pressure head-water saturation curve was partial.

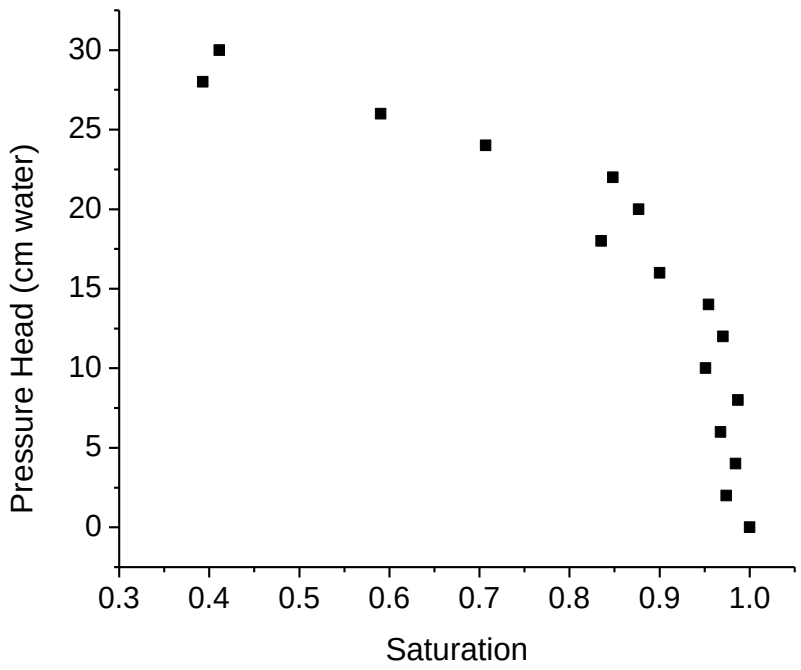

Figure A.1 Pressure head - saturation profile for Ottawa sand using wet packing method.

APPENDIX B IMAGE PROCESSING RESULTS FOR RESIUDAL NAPL SATURATION CALCULATIONS

APPENDIX B Figures and Tables

Figure B.1 Image analysis for E15 spill average residual NAPL saturation calculation. 139

Figure B.2 Image analysis for E25 spill average residual NAPL saturation calculation. 140

Figure B.3 Image analysis for E50 spill average residual NAPL saturation calculation. 141

Figure B.4 Image analysis for E85 spill average residual NAPL saturation calculation. 142

Table B.1 E15 average residual NAPL saturation calculations. 143

Table B.2 E25 average residual NAPL saturation calculations. 143

Table B.3 E50 average residual NAPL saturation calculations. 144

Table B.4 E85 average residual NAPL saturation calculations. 144

1st measurement:

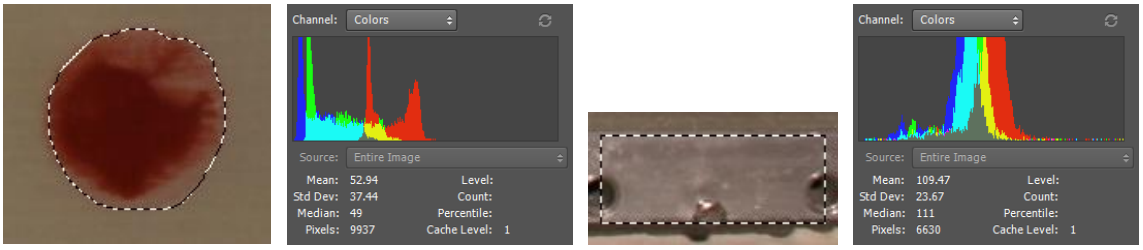

2nd measurement:

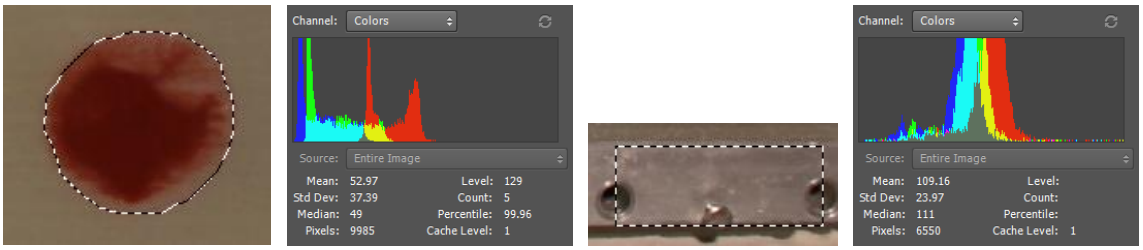

3rd measurement:

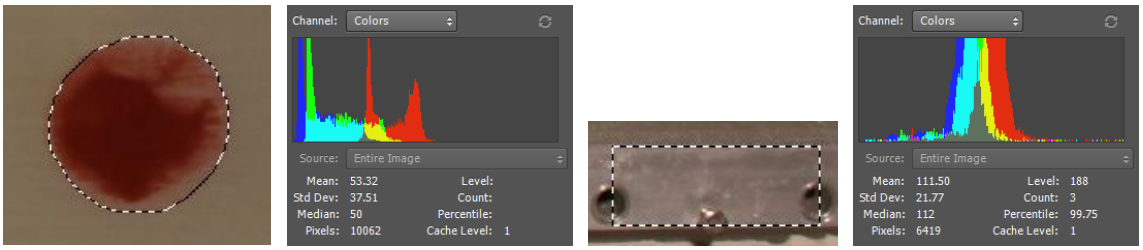

Figure B.1 Image analysis for E15 spill average residual NAPL saturation calculation.

1st measurement:

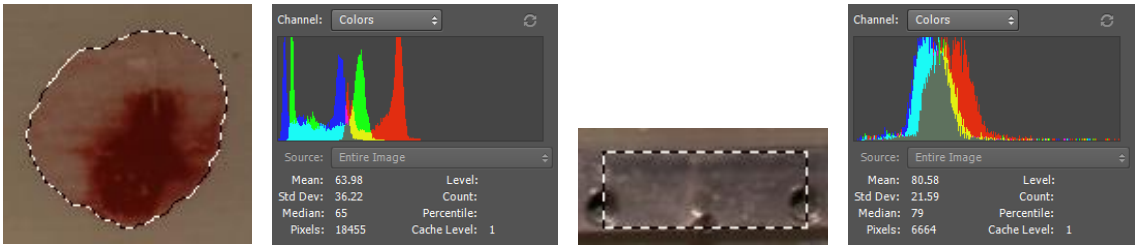

2nd measurement:

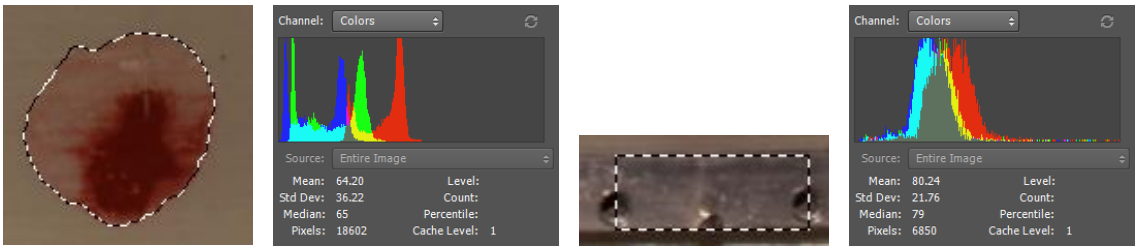

3rd measurement:

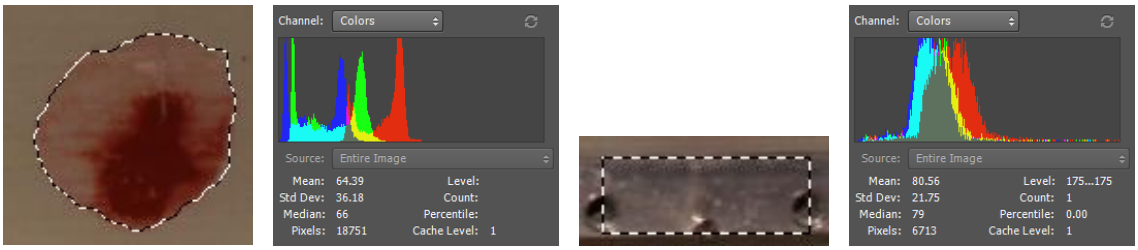

Figure B.2 Image analysis for E25 spill average residual NAPL saturation calculation.

1st measurement:

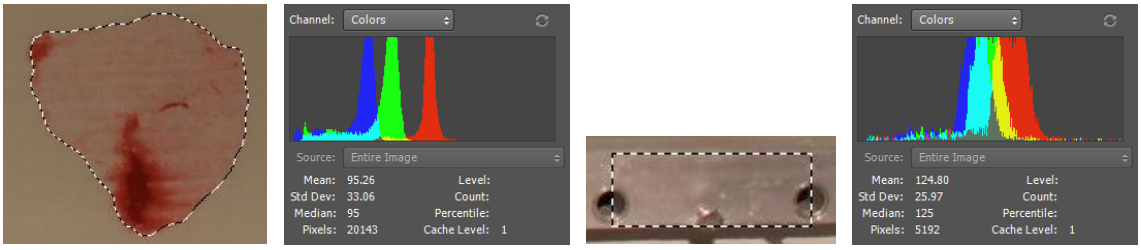

2nd measurement:

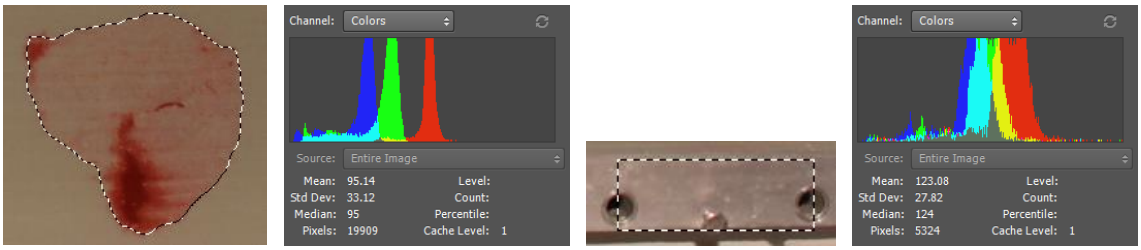

3rd measurement:

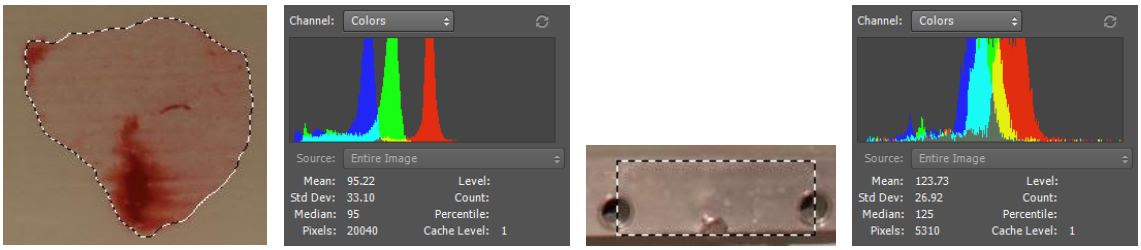

Figure B.3 Image analysis for E50 spill average residual NAPL saturation calculation.

1st measurement:

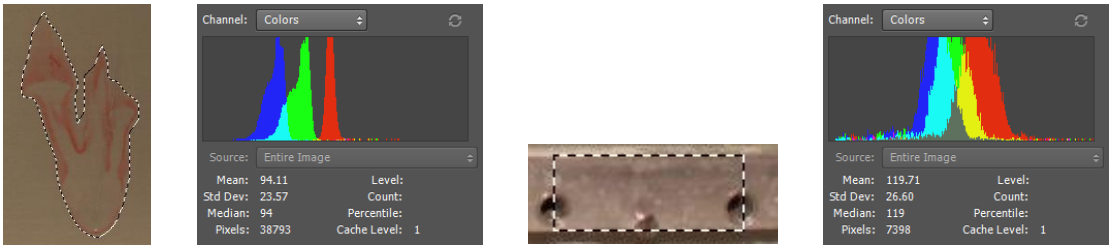

2nd measurement:

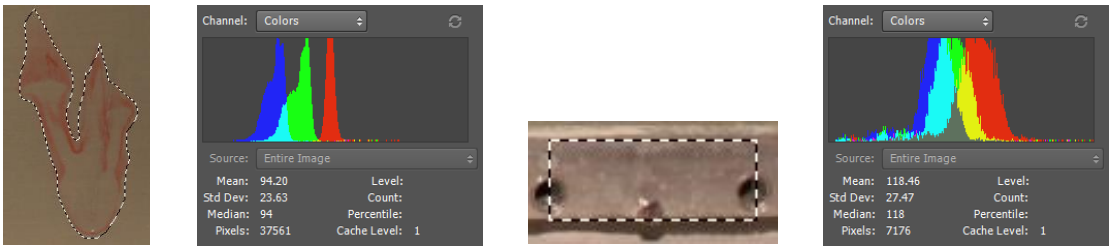

3rd measurement:

Figure B.4 Image analysis for E85 spill average residual NAPL saturation calculation.

Table B.1 E15 average residual NAPL saturation calculations.

E15	**1st**	**2nd**	**3rd**
Ref. Pixel	6630	6550	6419
NAPL. Pixel	9937	9985	10062
NAPL/Ref. Ratio	1.50	1.52	1.57
NAPL Impacted Area, cm^2	52.68	53.58	55.10
NAPL Vol., cm^3	42.15	42.87	44.08
NAPL Vol.% in Gasohol	0.85	0.85	0.85
NAPL Vol. Injected (mL)	34	34	34
NAPL S_{or}	0.81	0.79	0.77
NAPL S_{or} Avg.			0.79
STD			0.02

Table B.2 E25 average residual NAPL saturation calculations.

E25	**1st**	**2nd**	**3rd**
Ref. Pixel	6664	6850	6713
NAPL. Pixel	18455	18602	18751
NAPL/Ref. Ratio	2.77	2.72	2.79
NAPL Impacted Area, cm^2	97.34	95.45	98.18
NAPL Vol., cm^3	77.87	76.36	78.55
NAPL Vol.% in Gasohol	0.75	0.75	0.75
NAPL Vol. Injected (mL)	30	30	30
NAPL S_{or}	0.39	0.39	0.38
NAPL S_{or} Avg.			0.39
STD			0.01

Table B.3 E50 average residual NAPL saturation calculations.

E50	**1st**	**2nd**	**3rd**
Ref. Pixel	5192	5324	5310
NAPL. Pixel	20143	19909	20040
NAPL/Ref. Ratio	3.88	3.74	3.77
NAPL Impacted Area, cm^2	136.37	131.44	132.66
NAPL Vol., cm^3	109.09	105.15	106.13
NAPL Vol.% in Gasohol	0.50	0.50	0.50
NAPL Vol. Injected (mL)	20	20	20
NAPL S_{or}	0.18	0.19	0.19
NAPL S_{or} Avg.			0.19
STD			0.00

Table B.4 E85 average residual NAPL saturation calculations.

E85	**1st**	**2nd**	**3rd**
Ref. Pixel	7398	7176	7124
NAPL. Pixel	38793	37561	35615
NAPL/Ref. Ratio	5.24	5.23	5.00
NAPL Impacted Area, cm^2	184.32	183.98	175.73
NAPL Vol., cm^3	147.45	147.19	140.58
NAPL Vol.% in Gasohol	0.15	0.15	0.15
NAPL Vol. Injected (mL)	6	6	6
NAPL S_{or}	0.04	0.04	0.04
NAPL S_{or} Avg.			0.04
STD			0.00

APPENDIX C PORE WATER SHORT-TERM CONCENTRATION MEASUREMENT FOR INDIVIDUAL HYDROCARBON COMPOUND

APPENDIX C Figures and Tables

Figure C.1 E25 Pore water concentration analyses for individual hydrocarbon compounds. 146

Figure C.2 E50 Pore water concentration analyses for individual hydrocarbon compounds. 147

Figure C.3 E85 Pore water concentration analyses for individual hydrocarbon compounds. 148

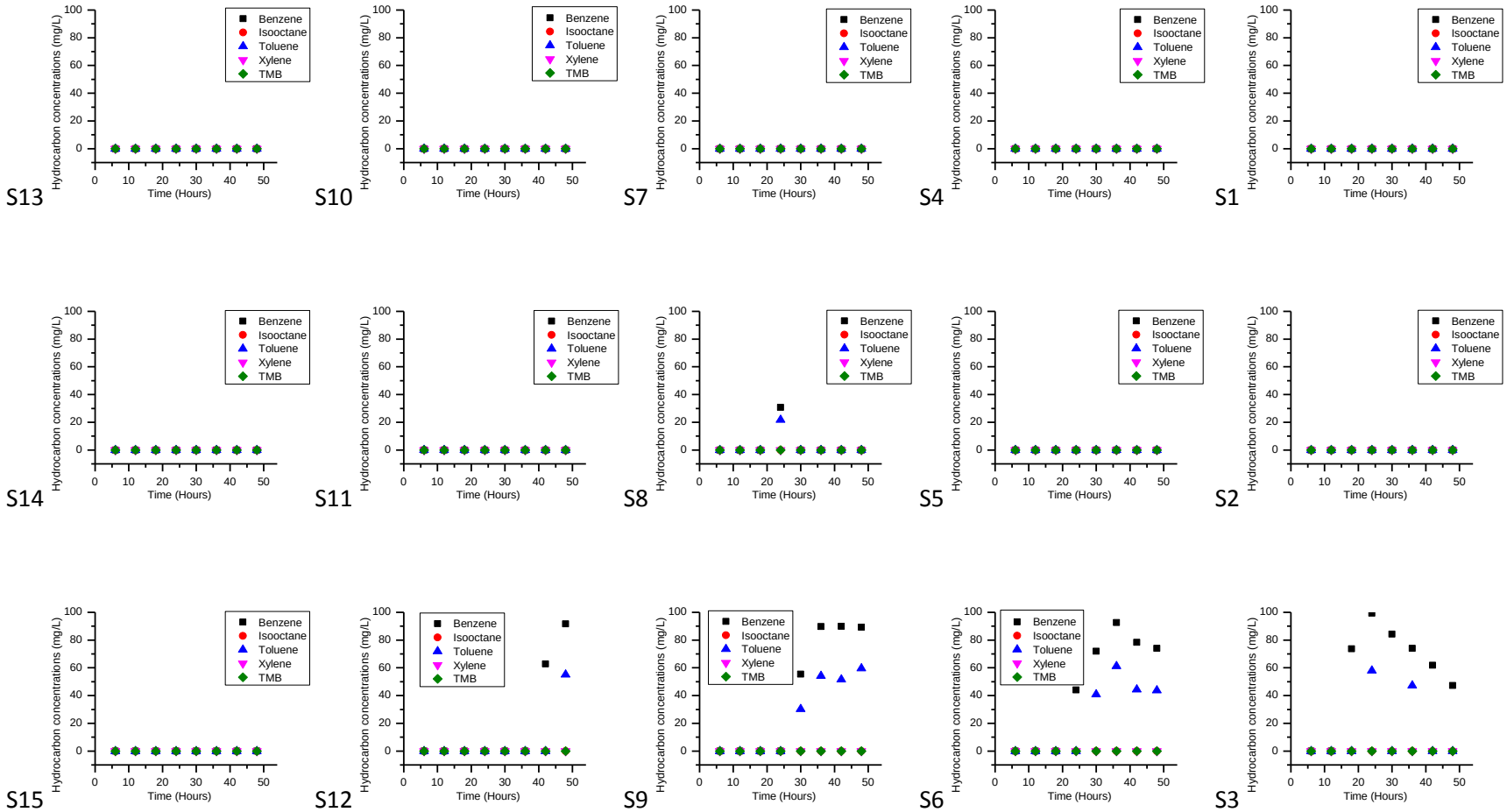

Figure C.1 E25 Pore water concentration analyses for individual hydrocarbon compounds.

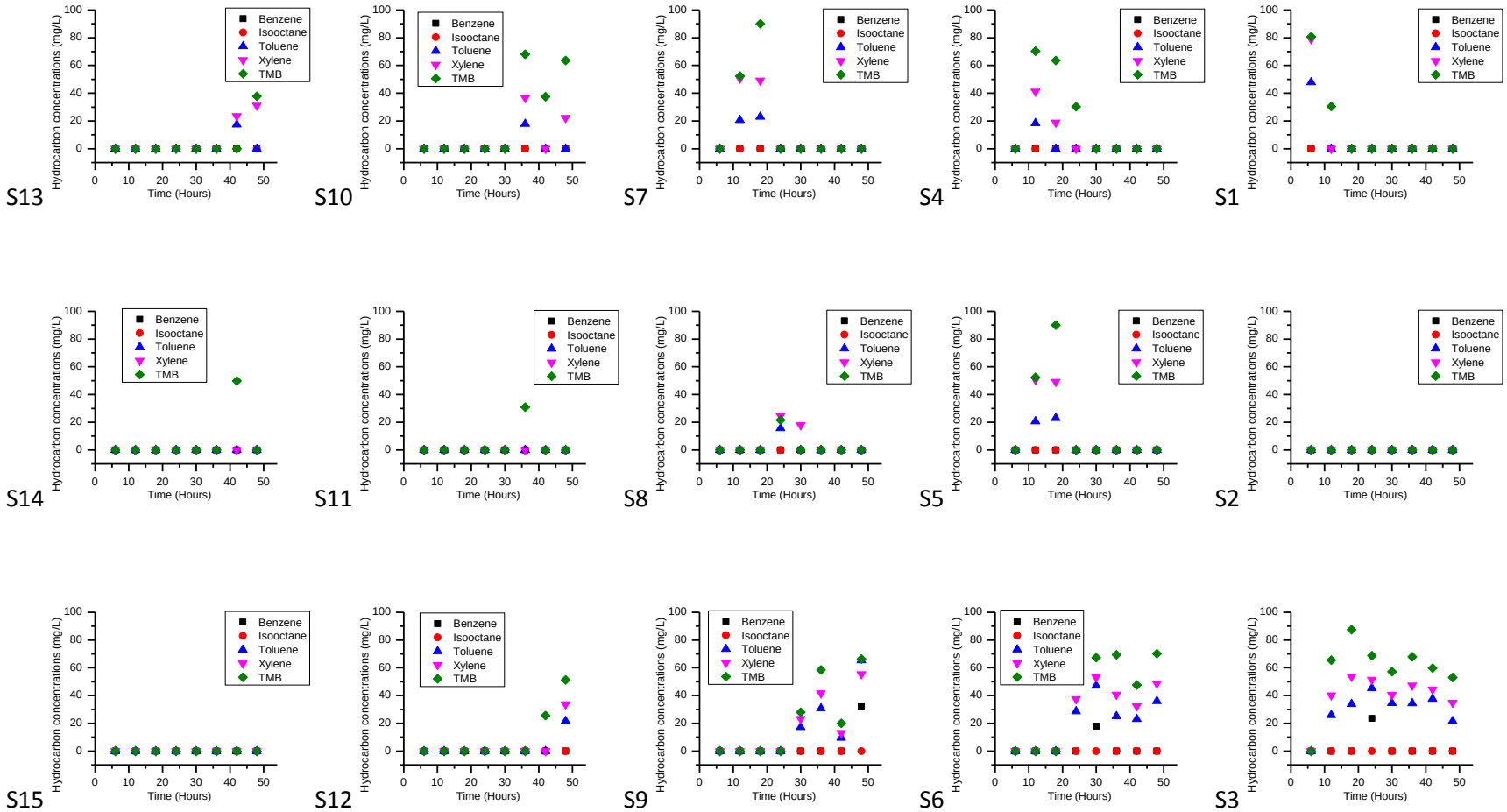

Figure C.2 E50 Pore water concentration analyses for individual hydrocarbon compounds.

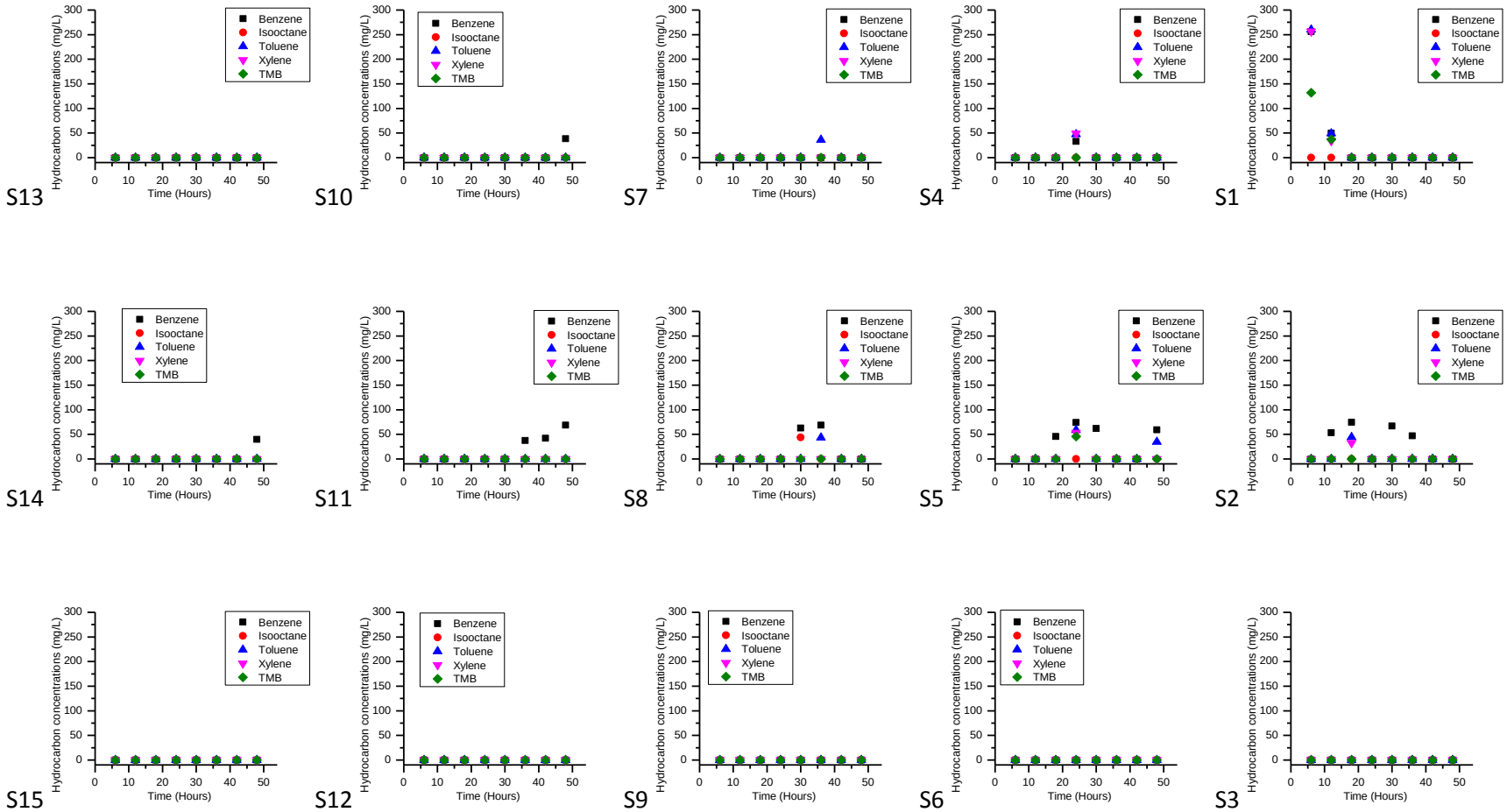

Figure C.3 E85 Pore water concentration analyses for individual hydrocarbon compounds.

APPENDIX D SIMULATION RESULTS WITH VARIOUS PERMEABILITY AND POROSITY CASES

APPENDIX D Figures and Tables

Figure D.1 E50 ethanol source behavior with Case 1 permeability and porosity..... 150

Figure D.2 E50 ethanol source behavior with Case 2 permeability and porosity..... 150

Figure D.3 E50 ethanol source behavior with Case 3 permeability and porosity..... 151

Figure D.4 E50 ethanol source behavior with Case 4 permeability and porosity..... 151

Figure D.5 E50 ethanol source behavior with Case 5 permeability and porosity..... 152

Figure D.6 E50 NAPL source behavior with different permeability and porosity combinations. 153

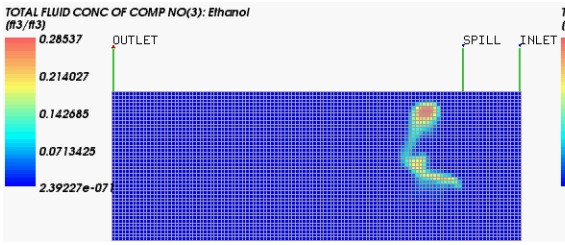

(a) 6 hours

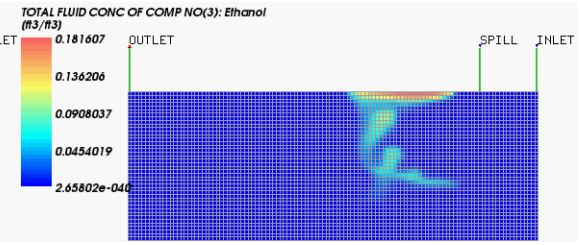

(b) 12 hours

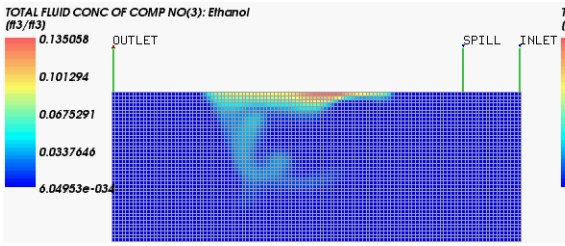

(c) 24 hours

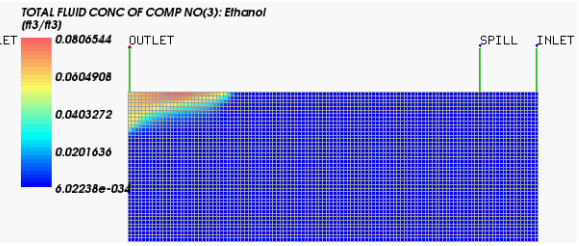

(d) 48 hours

Figure D.1 E50 ethanol source behavior with Case 1 permeability and porosity.

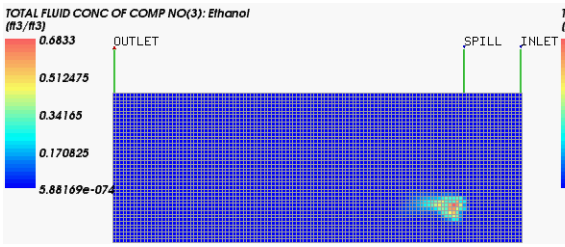

(a) 6 hours

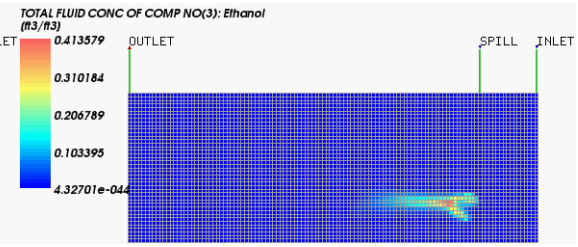

(b) 12 hours

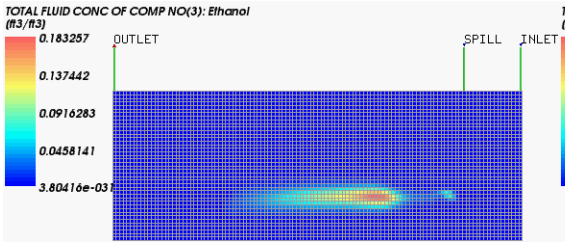

(c) 24 hours

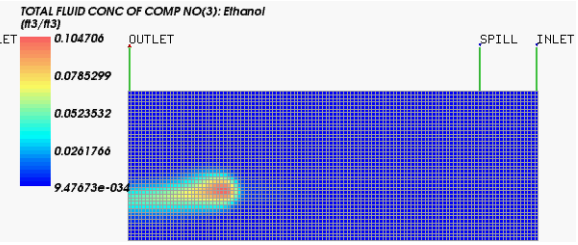

(d) 48 hours

Figure D.2 E50 ethanol source behavior with Case 2 permeability and porosity.

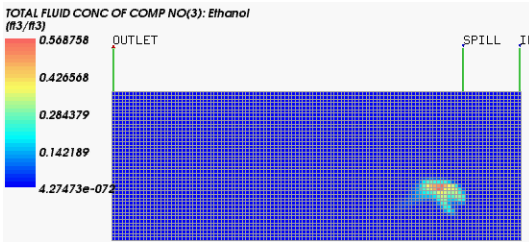

(a) 6 hours

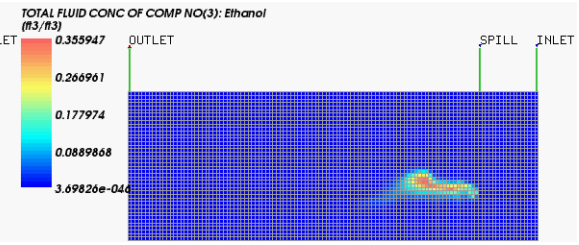

(b) 12 hours

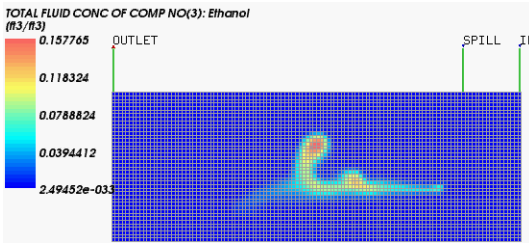

(c) 24 hours

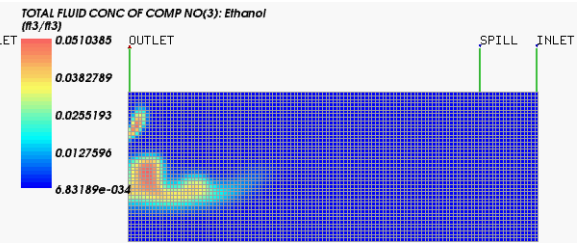

(d) 48 hours

Figure D.3 E50 ethanol source behavior with Case 3 permeability and porosity.

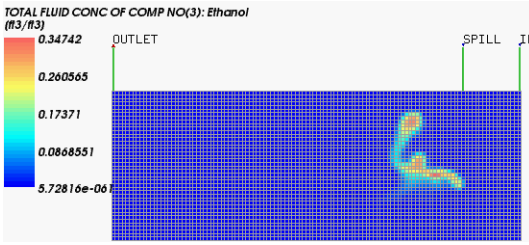

(a) 6 hours

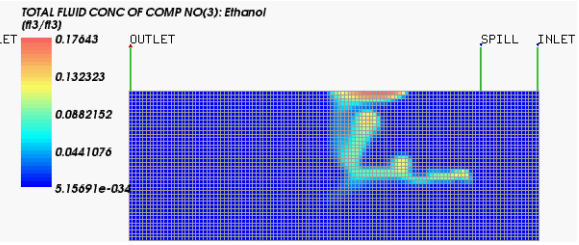

(b) 12 hours

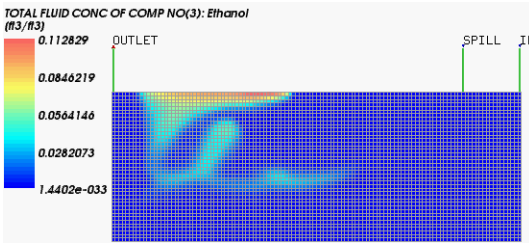

(c) 24 hours

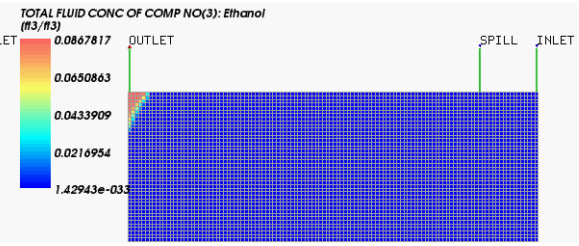

(d) 48 hours

Figure D.4 E50 ethanol source behavior with Case 4 permeability and porosity.

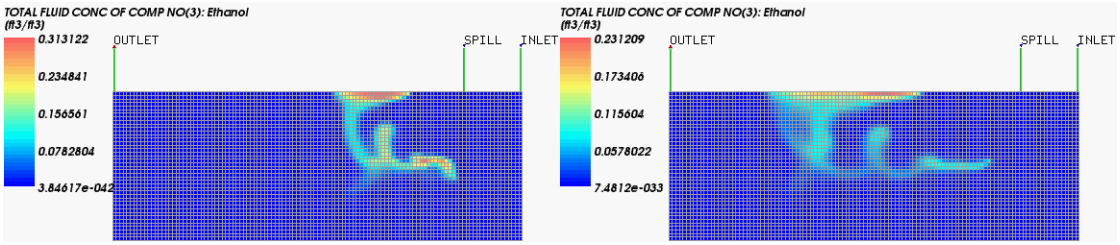

(a) 6 hours (b) 12 hours

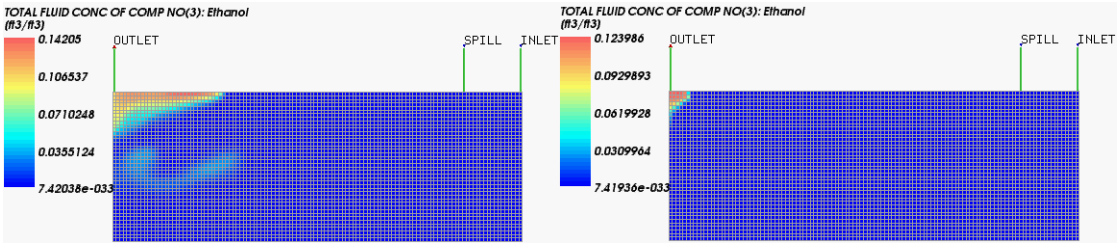

(c) 24 hours (d) 48 hours

Figure D.5 E50 ethanol source behavior with Case 5 permeability and porosity.

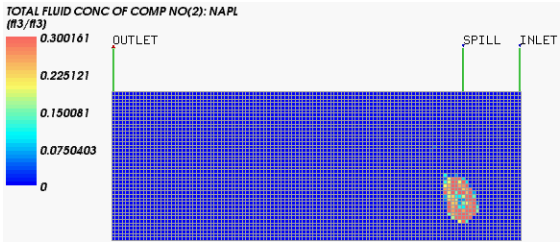

(a) Case 1

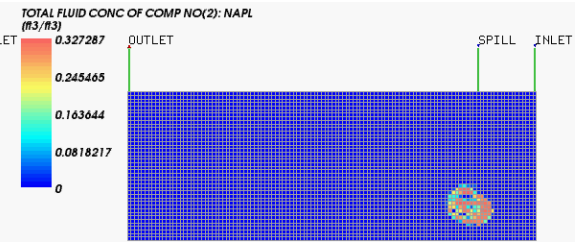

(b) Case 2

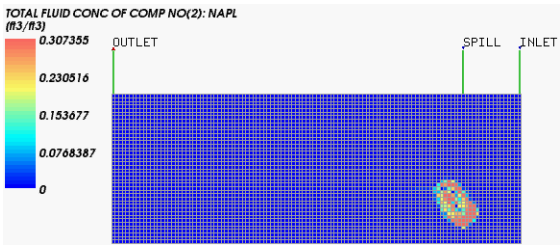

(c) Case 3

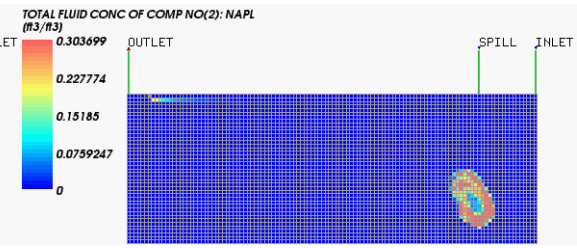

(d) Case 4

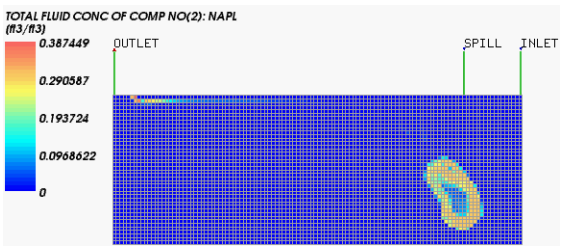

(e) Case 5

Figure D.6 E50 NAPL source behavior with different permeability and porosity combinations.